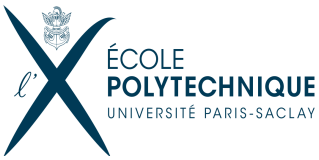

Thèse présentée pour obtenir le grade de

DOCTEUR DE L'ÉCOLE POLYTECHNIQUE

spécialité : mécanique

par

V K Chakravarthy RAVILLA

Local and global instabilities in buoyant jets and plumes

à soutenir le 10 décembre 2015 devant le jury composé de :

Colm-cille Caulfield	rapporteur
Carlo Cossu	rapporteur
Patrick Huerre	directeur de thèse
Lutz Lesshafft	directeur de thèse
Patrice Meunier	examinateur
Jean-Christophe Robinet	examinateur

Abstract

Local and global eigendynamics of free plumes are analyzed in this dissertation, with a particular focus on the possibility of self-sustained global oscillations. Such behavior in plumes is examined from the perspective of hydrodynamic stability. In this investigation, local absolute instability as well as linear global instability are found in the plumes, suggesting that plumes may indeed display self-sustained oscillator behavior. The frequency of the most unstable global mode matches closely with the self-excited axisymmetric puffing reported from experiments and direct numerical simulations of plumes and buoyant jets. A low Mach number approximation is employed for the global instability analysis, which captures the non-Boussinesq effects in flows with arbitrarily large density variations. The Boussinesq setting represents a special case of the low Mach number formulation, reached in the limit of small density variations. In this limit, a local analysis indicates the presence of an absolute instability of very low frequency for helical perturbations. However, this absolute instability does not appear to provoke a global instability, possibly due to its small absolute growth rate. The dynamics of plumes are contrasted with that of buoyant jets; these two regimes of the vertical flow of hot fluid are characterized by the Richardson number Ri. An endogeneity analysis demonstrates that global instability in jets (low Ri) is mostly driven by base flow shear, whereas the global destabilization of plumes (high Ri) is dominantly caused by buoyancy. The local instability modes in Boussinesq plumes are interpreted by means of the perturbation kinetic energy equation.

Résumé

Cette thèse vise à décrire la dynamique propre des panaches libres à partir d'approches locales et globales. Il s'agit en particulier de déterminer si, dans le cadre de la thorie de l'instabilité linéaire, des oscillations auto-entretenues sont susceptibles de se produire dans le cas des panaches. Les configurations considérées dans cette étude prsentent effectivement une instabilité absolue locale ainsi qu'une instabilité globale linéaire. Les panaches peuvent donc être le siège d'oscillations synchronisées. La fréquence prédite par la présente analyse globale est en bon accord avec les observations expérimentales et les simulations numériques directes de jets légers. Une formulation valable aux faibles nombres de Mach est utilisée pour l'analyse d'instabilité globale, retenant ainsi les effets non-Boussinesq présents dans les écoulements à forte variation de masse volumique. Dans la limite des faibles variations de masse volumique, cette formulation se rduit aux équations de Boussinesq. Une analyse d'instabilité locale dans cette limite révèle alors la présence d'une instabilité absolue pour des modes hélicoïdaux de très basse frquence. Toutefois, cette instabilité absolue ne semble pas donner lieu à une instabilité globale, vraisemblablement en raison de son faible taux de croissance absolu. La dynamique des panaches est comparée avec celle des jets légers; ces deux rgimes distincts, associés à un écoulement ascendant sous l'effet de la flottabilité, sont caractérisés par leur nombre de Richardson Ri. Une analyse basée sur le concept rcent dl'endogénéité démontre que l'instabilité globale d'un jet (Ri faible) est principalement due au cisaillement de l'coulement de base, tandis que la dstabilisation globale des panaches (Ri grand) est dominée par la flottabilité. Les modes d'instabilité locale dans la limite Boussinesq sont interprétés par le biais de l'équation de l'énergie des perturbations.

Acknowledgments

As with everyone entering École polytechnique (yes, "p" is in lowercase!), mine too began at the Lozère station and the famed staircase that follows, with the additional features of a cold rainy day in December and a reliable friend who totally forgot that he had to pick me up from the station. With this, I realized why people say getting into Polytechnique is difficult! After this martial-styled welcome, things were a lot smoother, thanks to my advisers Dr. Lutz Lesshafft and Prof. Patrick Huerre. Though there was a period of turbulence with regard to funding, they had me well insulated.

I would firstly like to thank my advisers for the freedom to pursue things in my own priority order and at the same time making me staying focused on the bigger picture. If Lutz, my primary adviser, had not pulled me back from being obsessed with tiny $\mathcal{O}(\varepsilon^2)$ details, ex. stationary modes and soft global modes, I would have never understood the more important features of the flow, like global instability, or maybe never completed the work within the stipulated time. His focus and guidance to always pursue the broader picture but not get stuck on one minute detail is very helpful skill. I wish to continue that philosophy further into my career. Apart from technical details, he maintains a high standards professional ethics by placing students ahead of himself (ex. Stockholm conference) and this is another important thing I will practice in my professional life in the future.

Another equally important person I would like to thank for the successful completion of the thesis is Patrick Huerre, co-adviser of my thesis. When I just began the dissertation, I had too many trivial questions on the stability theory and he always gave the answer even before I completed the question. This "awe" factor about him remained throughout my PhD and will continue in future as well. Whenever I and Lutz get stuck on nuances of stability analysis, recent one being perturbation energy budgets, or on things related to asymptotic analysis and complex planes, he has the information and full array of techniques to help us out. With his vast experience, he always places the results in a broader perspective and helped me have a generic picture of hydrodynamic stability analysis and fluid mechanics. In addition to Science, he has also taught me English grammar, especially the importance of the article "the"!!

As I understood later, both of my advisers had to endure severe trouble during the discussions as well as while reading through my manuscripts due to the cryptic style of my presentation and the miniature sketches, which I

referred to as figures/plots. Patrick took my brunt of my first manuscript and he added the word “the” at least at 50 places in the manuscript. Later, Lutz re-plotted the results in the article and made them human-readable to demonstrate to me how a figure should look and why it is important for scientific discussion in the first place. This situation, I hope, improved over time.

Also, both Lutz and Patrick practiced and demonstrated the broad philosophy and critical assessment of the results one has to have in research to make meaningful contributions. I hope to take forward this research attitude I learnt working with them in my future endeavours. Overall, I think it is indeed an enjoyable transition to referring them as Lutz and Patrick instead of Dr. Lutz Lesshafft and Prof. Patrick Huerre. I thank them for this great learning experience.

I would also like to thank the lab, Laboratoire d’Hydrodynamique (LadHyX) for the friendly work environment and Prof. Christophe Clanet, head of the lab, for taking care of the funding troubles. In this context, I particularly thank the Directeur général de l’École polytechnique, IGA Yves Demay, for kindly agreeing to fund my scholarship through École Doctorale and bail me out of the funding complication. I would also like to acknowledge the contribution of my fellow PhDs and Postdocs at LadHyX for the nice discussions and time. Special thanks to Onofrio (bearing through my complaint sessions, helping me with my final presentations, postdoc hunt etc.) and Yifan (assistance with the highly non-trivial bureaucratic procedures of France).

I also take this opportunity to thank my teachers all through my career (school, college etc) who were responsible for me to land at l’X in the first place, particularly the faculty at IIT M (Prof. S R Chakravarthy, Dr. T M Muruganandam), JNC (Prof. Rama Govindarajan) and my school teachers (Mrs. Vydehi, Mr. Johnson and Mr. L N Raju). I conclude by thanking my parents and friends for keeping me in good spirit (Aditya, Srikanth, Kanna, Ashish, Leopoldine, Prabal, Onofrio, Yifan, Shreyas, Supriyo and many others I met at Citè, hikes, Polytechnique and other events in Paris).

These have been three really eventful years !

V K Chakravarthy RAVILLA

Contents

Chapter 1

Introduction

> "Any solid lighter than a fluid will, if placed in the fluid, be so far immersed that the weight of the solid will be equal to the weight of the fluid displaced."
>
> "If a solid lighter than a fluid be forcibly immersed in it, the solid will be driven upwards by a force equal to the difference between its weight and the weight of the fluid displaced."
>
> "A solid heavier than a fluid will, if placed in it, descend to the bottom of the fluid, and the solid will, when weighed in the fluid, be lighter than its true weight by the weight of the fluid displaced."
>
> -Archimedes of Syracuse, c. 250 BC.

With these postulates by Archimedes [32], the quantitative study of buoyancy began, possibly inside a bathtub, in ancient Greece.

A buoyancy force can be generated in a flow field under a multitude of situations such as hot fluid injected into a cold ambient, low density fluid injected into a high density fluid, change of phase or chemical reactions. This force, in turn, results in a plethora of flow fields. Common examples are atmospheric and oceanic circulations, ventilation in confined spaces, volcanic plumes, under-ice convection, chimney exhausts, saline jets, lifted flames etc.

Most buoyancy-driven flows are unstable, resulting in large-scale unsteady dynamics and the subsequent transition to a turbulent state within a few diameters downstream of the inlet. Prediction of the laminar to turbulent

transition and controlling the dynamics could be of great practical interest. For instance, in the case of lifted flames, an instability upstream of the flame front could result in large fluctuations in the flame front location and drastically alter the combustion efficiency. The emphasis of this dissertation is to understand the role of buoyancy in destabilizing the flow fields of buoyant jets and plumes in a laminar setting before they transition into a turbulent state.

1.1 Long-time response

In stability analysis, the question one seeks to answer is, "if the base flow is perturbed infinitesimally at time $t = 0$, will it return to the initial state provided one waits long enough?" In this investigation, the response of the flow in the limit $t \to \infty$, referred to as the *long-time response*, is considered. The perturbation is assumed to be a white noise which mimics the random fluctuations of the ambient.

In order to predict the long-time response of the steady base flow to a perturbation, a standard method is to superpose an infinitesimally small perturbation on the base state and linearize the governing equations about the base state. The complex frequency ω, which is obtained as an eigenvalue of the linearized governing equations and boundary conditions, determines the evolution of the perturbation field in the asymptotic limit $t \to \infty$. Rayleigh [76] first applied these techniques to understand the dynamics of inviscid flows. This was later extended to include viscous effects by Orr [65] and Sommerfeld [82] independently. Depending on the assumptions made on the base flow as well as the perturbations, the stability problem may be posed in a *local* or *global* sense

In a local analysis, the streamwise evolution of the base flow is assumed to be much slower in comparison to the perturbation evolution. Therefore, in a cylindrical coordinate system, the base flow is taken to be of the form

$$\overline{q} = \overline{q}(r), \tag{1.1}$$

and perturbations of the form

$$q' = \hat{q}(r)e^{i(kz+m\theta-\omega t)} + c.c. \tag{1.2}$$

Here, $\overline{q}$ and q' denote the state vectors which include all the variables of the base flow and the perturbation respectively. In physical terms, the local approximation amounts to considering a slice of the flow at some streamwise

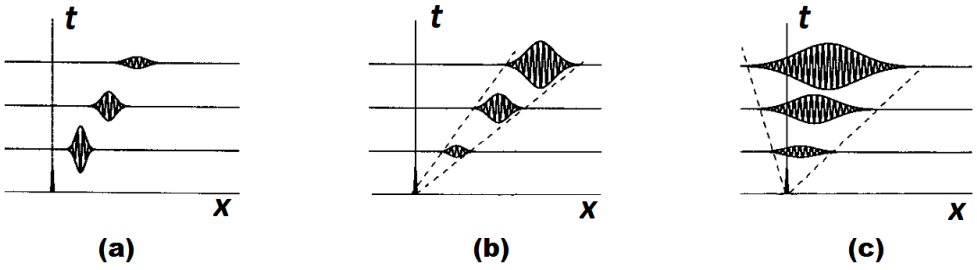

Figure 1.1: Schematic of various linear impulse responses in the $x-t$ plane: a. stable; b. convectively unstable; c. absolutely unstable. The figure is adopted from figure 8 in *Open shear flow instabilities* by Huerre [34]

.

location and extending it to $-\infty$ and $+\infty$ along the streamwise direction. This implies that, in order to satisfy the conservation of mass, given by the continuity equation, only the streamwise component of the velocity survives and other components of velocity vanish. Under these assumptions on the base flow, and in the absence of any pressure feedback from the boundary, if a steady flow is perturbed by an infinitesimally small impulse at time $t = 0$ and the response is recorded as $t \to \infty$, the response can be classified into three categories shown in the schematic 1.1: a. stable - the perturbation decays in time as it is convected downstream; b. convectively unstable - the perturbation grows in time as it convected downstream but in the long-time limit, the perturbation is convected out of the domain and the flow returns to the initial state; and c. absolutely unstable - the perturbation grows exponentially in time throughout the flow field and the initial flow state is never reached in the long-time limit. Such a classification of the flows can be made based on the growth rate of the most unstable eigenmode, and for the ansatz (1.2), the imaginary part of the complex frequency ω gives the growth rate. If the maximum *temporal growth rate* is negative, then the flow is stable, while in a convectively unstable flow the temporal growth rate is positive but the *absolute growth rate* is negative, and in an absolutely unstable scenario, both the absolute and temporal growth rates are positive. The notions of convective/absolute instability and their computation through the method of steepest descent were established in the plasma physics community by Briggs [7] and Bers [3]. These concepts were later adopted to analyze open shear flows by Huerre & Monkewitz [35].

In a global analysis, the streamwise evolution of the base flow is accounted for and no assumption is made on the spatial variation of the eigenfunction.

For a weakly nonparallel base flow, this may be accomplished through an integration of the local stability properties of the base flow at each streamwise location in the z-direction under the WKBJ assumption [12]. However, the applicability of such an analysis might be limited if the flow is strongly nonparallel. A robust way to account for the streamwise variation in the base flow is to assume a perturbation of the form

$$q' = \hat{q}(r, z)e^{i(m\theta - \omega t)} + c.c., \tag{1.3}$$

over a base flow of the form

$$\overline{q} = \overline{q}(r, \theta, z) \tag{1.4}$$

and then, as in the local analysis, linearize the governing equations to obtain ω as an eigenvalue of the linearized system. The long-time response of the flow is classified similar to the local framework: a. stable - all the global eigenmodes decay exponentially in time and the resulting perturbation field decays in time as it is convected downstream; b. amplifier - similar to the stable scenario, all the global modes decay exponentially in time but through non-normal interaction between the eigenmodes, the perturbation field grows spatially as it propagates downstream [15] and it is eventually convected out of the domain, thereby returning the flow to its initial state; and c. globally unstable or oscillator - at least one global eigenmode grows exponentially in time throughout the flow field. The amplifier and oscillator states are the global analogues to the local convective and absolute instability states, respectively. However, unlike the local stability analysis, it is not possible to distinguish between globally stable and amplifier type flows purely on the basis of global eigenvalue spectrum. Note that all the oscillator type flows are necessarily absolutely unstable for some region while, only those flows with strong absolute growth rates over a large enough streamwise extent can become globally unstable. This was shown rigorously for the case of the 1-D Ginzburg-Landau equation [12] but this has been observed to hold true for many real flows such as wakes, jets, shear layers, etc. A typical example of an oscillator type flow is the wake of a bluff body, which above a critical Reynolds number presents intrinsic periodic oscillations [74]. A similar behaviour holds for counter-flowing jets and shear layers. On the other hand, co-flowing shear layers and homogeneous jets act as amplifiers [38, 84].

The oscillator type behaviour is intrinsic to the base flow, i.e. continuous external forcing is not required to sustain the oscillation of such global modes and therefore, these modes are called *self-sustained oscillations*. They

are triggered by the white noise of the system and sustained by the energy transferred from the base flow through various mechanisms such as shear, baroclinic torque, buoyancy, etc. Note that until now, only infinitesimal perturbations are discussed and such an analysis is called linear analysis. The global modes obtained under this framework should be qualified further as *linear global modes*. Once these infinitesimally small amplitude linear global modes grow in time, they saturate and result in a limit cycle called *nonlinear global mode*. An example of such nonlinear global mode is shown in figure 1.2 which presents a snapshot of the smoke rising from a cigarette, an archetype of buoyancy-driven flow.

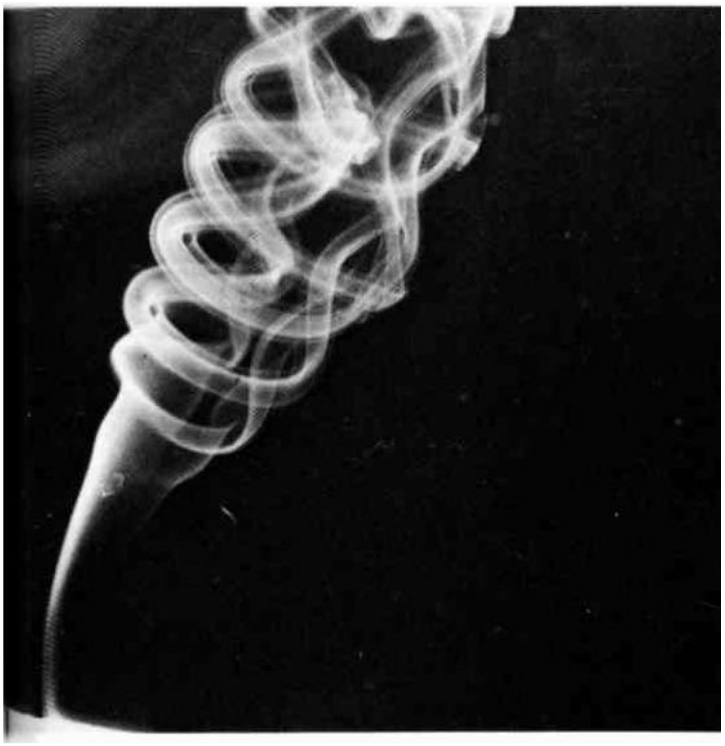

Figure 1.2: Photograph of the smoke rising from a cigarette taken from van Dyke's *An album of fluid motion* (figure 107) [92]. The flow rises from the heat source steadily and evolves into an unsteady self-sustained oscillatory pattern downstream of the source.

Unlike the linear global mode, where the entire flow field is contaminated by the perturbation in the long-time limit, a nonlinear global mode exists only downstream of a *stable front*. The location of such a front can be predicted from the local absolute/convective behaviour and the departure from the

local prediction is likely to increase with the nonparallel nature of the flow [17, 18, 70, 71]. In experiments and DNS, one observes these nonlinear global modes and they cannot be obtained through a linear stability analysis.

1.2 Buoyant jets and plumes

Consider a helium jet injected vertically upwards into quiescent air. The fluid continues to rise up due to two forces: inertia imparted at the inlet and the buoyancy force as helium density is lower than ambient air density. Depending on the strength of these two forces, the evolution of the flow downstream of the inlet varies. This is quantified by the Richardson number Ri, which is a measure of the relative strength of the buoyancy and inertia forces. In the limit of $Ri \ll 1$, referred to as *buoyant jets*, the inertia of the fluid at the inlet has a stronger effect than the buoyancy and the flow evolves in the same way as jets [64]. In the limit of $Ri \gg 1$, referred to as *plumes*, the converse holds; the downstream evolution of the flow is determined by buoyancy imparted to the fluid at the inlet.

The dynamics of pure jets, where the effect of buoyancy is completely omitted, have been studied in great detail. Various types of stability analyses, direct numerical simulations (DNS) and experiments were performed to understand the dynamics of jets. It was established that the classical isothermal homogeneous density jets are convectively unstable locally and amplifier type globally [25]. However, on addition of counter-flow [38, 84], or density variation (either due to heating the fluid [64] or variation of species composition and thereby density [83]), global modes are observed. In all these scenarios, it was demonstrated that the instability is either due to baroclinic torque (*jet column mode*) [44] or stronger velocity gradient (*shear mode*) [84].

For the case of laminar plumes, however, such detailed investigations are missing. Most of the plumes observed in nature become turbulent within a few diameters downstream of the inlet. The evolution of the time-averaged mean flow quantities along the streamwise direction were described by Morton, Taylor & Turner [61] in 1956 (further referred to as the MTT model) by assuming that the mean entrainment velocity is proportional to the local spatial average of the mean axial velocity. This is equivalent to assuming a self-similar variation for the mean flow quantities. The MTT model is very successful in predicting the mean flow quantities, height of the plume, radial spreading of the plume etc. Corrections were proposed to predict the mean flow close to the source where the flow has not yet reached the self-similar

state [37]. List [48] and Woods [96] present a review of this MTT model applied to various flow scenarios. Woods [96] particularly examines the flow fields observed in natural convection such as atmospheric plumes, submarine pumice plumes, ventilation in confined spaces etc. In all these analyses on turbulent plumes, only spatially averaged mean flows were considered. Hence, a discussion on the stability of these flows profiles is not possible. Some recent studies have concentrated on the spatial structure of the turbulent plume [73] and interaction of plumes in complex configurations relevant to ventilation [5]. Stability analyses of such spatially resolved turbulent mean states could be interesting but the current thesis is limited to the dynamical characteristics of laminar plumes.

One of the first investigations of the stability of buoyancy-driven flows was undertaken by Gill & Davey [28] for planar plumes along a heated wall. Gebhart and his co-investigators have followed it up with numerous works on flows along a heated wall, free planar plumes and axisymmetric plumes [68, 67, 58]. Mollendorf & Gebhart [58] have studied the *spatial* stability of axisymmetric plumes. However, buoyancy was included only as a small correction parameter to the momentum equation. Given the difficulty in computing the base flow as well as the coupled stability problem for round plumes, many studies concentrated on planar plumes. A review article summarizing the various works on the stability of laminar plumes was presented by Gebhart [26]. Most of the early analyses were limited to the self-similar region [93, 58, 67] but recent studies have examined the region close to the buoyancy source as well [86, 30, 31, 10].

With regard to round plumes, for a long time, the analysis was limited to Prandtl numbers of unity and 2. This is due to the availability of an analytical solution for the base flow [98]. A robust method for computing the base flow for other Prandtl numbers was proposed by Riley & Drake [77] and Worster [97] independently. Later on, many works on the computation of the base flow under various boundary conditions at the source followed [88, 94, 95]. The first *temporal* stability analysis of an axisymmetric free plume was performed by Riley & Tveitereid [78] and it was shown that the helical mode $m = 1$ is the most unstable mode in the streamwise wavenumber - Grashof number ($k-Gr$) plane. Through a perturbation energy analysis, it was shown that the instability in the low wavenumber and low Grashof number limit is due to buoyancy while at high Grashof numbers, the dynamics are shear dominated. Most investigations, however, considered the *spatial* stability of the plume [58, 93]. It is to be noted that none of the spatial stability investigations have established the validity of spatial analysis by showing the flow to be only convectively unstable but not absolutely unstable [34]. Also,

all these investigations have focused only on the self-similar region under the Boussinesq approximation while most of the plumes observed in nature are found to transition to a turbulent state within a few diameters downstream of the inlet. Hence, the pertinence of the predictions made in the self-similar region for real flows remains questionable.

Through a careful experiment, Subbarao & Cantwell [85] demonstrated the existence of self-sustained oscillations in helium jets, injected into air at Richardson numbers of the order unity, beyond a critical Reynolds number $Re_c(Ri)$. These observations were confirmed experimentally by Cetegen & Kasper [9] who also studied the dynamics of helium jets but for a much larger range of Richardson numbers. Satti & Agrawal [80] varied the Richardson number of the flow by altering the gravity in the DNS, and it was observed that as Ri is decreased, the self-sustained oscillations ceased to exist. However, DNS of the heated fluid injected into air in the buoyant jet limit by Nichols et al. [64], indicate the presence of a nonlinear global mode similar to hot jets. This discrepancy is due to the choice of inlet velocity profile: it is parabolic in the DNS of Satti & Agrawal [80] while it is a steep profile in Nichols et al. [64]. Note that in the case of helium jets, the variation in density along the cross-stream direction is large and the Boussinesq approximation no longer holds. Hence, Nichols et al. [64] the low Mach number approximation is used to model the flow in DNS studies. The present study follows that choice.

1.3 Objectives

In this investigation, a base flow as shown in the schematic 1.3 is considered. Here, heated fluid exits through a round orifice in an infinitely large, adiabatic, rigid wall and as the flow evolves downstream, it reaches self-similar velocity and temperature profiles which are independent of the inlet conditions. The dynamical behaviour of such a flow field is analyzed with an emphasis on understanding the role of buoyancy in the dynamics as well as in the base state.

From the brief review of the literature on plumes presented in the previous section, it can be seen that the vast majority of the studies on plumes are dedicated to turbulent plumes [61, 96, 73] and confined plumes [49, 63, 50]. Only a fraction of the studies are directed towards understanding the dynamical characteristics of laminar round plumes from a hydrodynamic stability point of view, and these were mostly limited to the classical local temporal

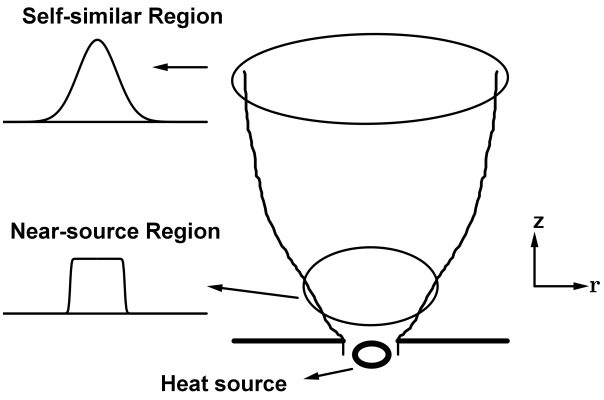

Figure 1.3: Schematic of the flow considered in this thesis. A heated fluid is continuously injected into a quiescent ambient from a round orifice in an infinitely large wall. As the flow is convected upwards, it evolves to a self-similar profile which is independent of the inlet profile.

and spatial stability analysis of the self-similar region under the Boussinesq approximation. Thus, much remains to be explored about the local stability characteristics, the role of buoyancy and how it varies in a plume in contrast to a buoyant jet. In the non-Boussinesq regime, only DNS and experiments have been undertaken until now. Furthermore, the dynamics in the plume limit, $Ri \gg 1$, have not yet been investigated from the stability point of view.

This dissertation envisages to uncover these missing pieces in our understanding of plumes and their dynamical behaviour. As a first step, both local and global linear instabilities of the plume are examined for a wide range of values of Richardson number and density variation, ranging from the Boussinesq limit up to large density variations, such as in helium jets injected into air. Rather than performing a mere parametric study, the objective here is to understand the role of buoyancy and shear forces in destabilizing the flow field. This is accomplished by studying the perturbation energy of the temporal mode in the local framework [78, 62]. Also, a mechanism through which buoyancy can destabilize the flow field has been proposed. In the global setting, the interplay between buoyancy and shear is studied through a new sensitivity metric: the *endogeneity* [51]. Comparisons will be drawn between the stability characteristics of non-buoyant jets/pure jets, buoyant jets and plumes to achieve a better understanding of the role of buoyancy.

1.4 Outline of the thesis

This thesis is organized into two main chapters followed by Concluding remarks.

Chapter 2, **Local linear stability of laminar axisymmetric plumes**, focuses on the local temporal and spatio-temporal behaviour of the self-similar region of the plume. The spatio-temporal stability of the self-similar Boussinesq plume is attempted for the first time and it is shown that only the helical $m = 1$ mode transitions to absolute instability. Further, this absolute instability is shown to be solely due to buoyancy. Most of the previous temporal investigations were limited to $Pr = 1, 2$ and helical perturbations $m = 1$ [78, 58, 93]. Here, in addition to the helical mode $m = 1$, the axisymmetric mode $m = 0$ and the double-helical mode $m = 2$ are also analyzed for a wide range of Prandtl numbers. The role of shear and buoyancy in the temporal instability of the flow is examined by computing the perturbation kinetic energy. For all the values of m investigated, buoyancy is shown to be dominant at the low Grashof numbers and wavenumbers while shear dominates in the high Grashof number regime. A mechanism through which buoyancy could destabilize the flow is proposed. The predictions of the self-similar region are demonstrated to hold good in the near-source region for a specific case as an example.

Chapter 3, **Global stability of buoyant jets and plumes**, deals with the linear global stability problem for a wide range of Richardson numbers Ri and ambient to jet density ratios S. The main aim of this part of the investigation is to examine the axisymmetric puffing observed in the helium jet experiments by Subbarao & Cantwell [85] and Cetegen & Kasper [9] from a hydrodynamic stability point of view. Under the Boussinesq limit, discussed in Chapter 2, the dynamics were predicted to be dominated by the helical mode $m = 1$ but the experimental investigations report axisymmetric puffing. Therefore, the local and global stability of the base flow is computed for both $m = 0$ and $m = 1$. It is observed that the local absolute instability of the helical mode present in the Boussinesq limit does not translate into an unstable global mode for all S and Ri investigated. However, beyond a certain density ratio $S_{crit}(Ri)$, an unstable global mode is observed in the global spectrum of $m = 0$. Moreover, the oscillation frequencies reported in the experiments are seen to match closely with the predicted axisymmetric linear global mode. Through examination of the integral measure of endogeneity for various terms in the governing equations, the relative contributions of buoyancy and shear towards global instability are calculated. Furthermore,

based on the spatial distributions of the endogeneity and the eigenfunctions, plausible differences in the mechanism through which these forces destabilize the flow are proposed.

The dissertation concludes with a summary of the main results, thereby giving an overall perspective of the work. This is followed by a broad road map for future extensions of the investigation.

Chapter 2

Local linear stability of laminar axisymmetric plumes

This chapter discusses the local stability of the laminar Boussinesq plume, primarily for self-similar profiles. The main results of this chapter are the following: the helical mode $m = 1$ is the dominant mode for most of the parameters investigated and beyond a critical Grashof number, it becomes absolutely unstable. The dominance of helical mode and its transition to an absolute instability is also demonstrated in a region close to the buoyancy source for a plume originating from a finite-sized inlet where the base flow is not self-similar. However, this was limited to a particular example.

The bulk of the material in this chapter, till section 2.4, is presented in the form of an article [10] which was published in *Journal of Fluid Mechanics*. Additional details which were not conclusively understood or computational details not presented in the article are discussed in sections 2.5 and 2.6.

Local linear stability of laminar axisymmetric plumes

R. V. K. Chakravarthy, Lutz Lesshafft and Patrick Huerre
Laboratoire d'Hydrodynamique (LadHyX), CNRS – École Polytechnique,
91128 Palaiseau, France

published in *Journal of Fluid Mechanics*, **780**, pp. 344–369

Abstract

The temporal and spatio-temporal stability of thermal plumes is investigated for laminar velocity and temperature profiles, under the Boussinesq approximation, in the far self-similar region as well as in the region close to a finite-size inlet. In the self-similar case, Prandtl and Grashof numbers are systematically varied, and azimuthal wavenumbers $m = 0$, 1 and 2 are considered. In the temporal analysis, helical modes of $m = 1$ are found to be dominant throughout the unstable parameter space, with few exceptions. Axisymmetric modes typically present smaller growth rates, but they may dominate at very low Prandtl and Grashof numbers. Double-helical modes of $m = 2$ are unstable over a very restricted range of parameters. Only the helical $m = 1$ mode is found to ever become absolutely unstable, whereas $m = 0$ and $m = 2$ modes are at most convectively unstable. In a temporal setting, an analysis of the perturbation energy growth identifies buoyancy- and shear-related mechanisms as the two potentially destabilizing flow ingredients. Buoyancy is demonstrated to be important at low Grashof numbers and long wavelengths, whereas classical shear mechanisms are dominant at high Grashof numbers and shorter wavelengths. The physical mechanism of destabilization through the effect of buoyancy is investigated, and an interpretation is proposed. In the near-source region, both axisymmetric and helical modes may be unstable in a temporal sense over a significant range of wavenumbers. However, absolute instability is again only found for helical $m = 1$ modes.

2.1 Introduction

The present paper investigates the local stability properties of round laminar plumes under the Boussinesq approximation. With these premises, the analysis pertains to physical situations where viscous forces are significant, and where density variations are sufficiently small. Examples for such situations are magma flows, saline jets, convective CO_2 transport in water, under-ice convection and algae suspensions (see Thorpe [89]; Lombardi et al. [49]; Nadal et al. [63] and references therein).

The velocity field of a steady plume resembles that of a jet, with the fundamental difference that a jet emerges from a nozzle with a given amount of streamwise momentum which merely diffuses radially as the fluid convects downstream, whereas the buoyancy in a plume flow continues to generate vertical momentum at any streamwise station. With regard to unsteady dynamics, buoyancy may provide new mechanisms of perturbation growth in addition to the well-known shear instabilities that are present in jets.

Mollendorf & Gebhart [58] investigated the spatial stability of a self-similar plume, although in a simplified framework where buoyancy effects were accounted for by adding a small forcing parameter to a non-buoyant jet analysis, thereby avoiding the solution of the coupled system of temperature and momentum equations. A spatial analysis was performed for Prandtl numbers $Pr = 2$ and 6.7. Weak buoyancy was observed to destabilize helical perturbations, with azimuthal wavenumber $m = 1$, but no instability was found for axisymmetric perturbations ($m = 0$). These conclusions were confirmed by the spatial analysis of Wakitani [93], who solved the fully coupled Boussinesq equations for settings with Prandtl numbers $Pr = 0.7$ and 2, and over a range of Grashof numbers. The observation of stable axisymmetric and unstable helical perturbations is consistent with the instability properties of fully developed non-buoyant jets [2].

The first *temporal* analysis of axisymmetric plumes was performed by Riley & Tveitereid [78]. Their investigation was limited to $Pr = 1$, and the results were congruous with the earlier spatial studies. By resorting to the perturbation kinetic energy equation, it was demonstrated that the instability at low Grashof numbers is mainly driven by buoyancy effects. The absence of a lower branch of the neutral instability curve, i.e. a lower limit on unstable wavenumbers, was attributed to the locally parallel flow assumption. A subsequent *nonparallel* spatial stability analysis [91] did indeed yield such a lower limit. However, the absolute or convective nature of the instability in all these laminar base flows has never been established, and the pertinence

of a spatial analysis therefore remains to be proven.

There is ample experimental and numerical evidence for oscillator behaviour in plumes and in related flows, suggesting the presence of absolute instability. The large majority of those settings, however, involves strong density differences outside the realm of validity of the Boussinesq approximation. Subbarao & Cantwell [85] as well as Cetegen & Kasper [9] observed self-sustained axisymmetric oscillations in their experiments with helium jets in air. Similar self-excited behaviour has been documented for planar plumes [8] and diffusion flames [53]. Jiang & Luo [40, 39] numerically studied the instability dynamics of thermal plumes and of diffusion flames, and they examined the role of buoyancy and baroclinic torque in the vorticity equation in order to explain the occurrence of self-sustained oscillations. Hattori et al. [31] identified an instability of the boundary layer over a heated plate as the cause for sinuous oscillations in the rising planar plume. Satti & Agrawal [79, 80, 81] performed a series of experimental and numerical studies on helium-air mixture injected into pure air. Their results indicate that such jets transition from oscillator- to amplifier-type behaviour as gravity is reduced. However, Lesshafft et al. [46] found oscillator behaviour in light jets in the absence of gravity. For the case of a confined plume inside a cylindrical container, driven by an extended heat source in the bottom wall, Lopez & Marques [50] documented a succession of bifurcations, through direct numerical simulation, leading from steady laminar flow to turbulence. The first of these bifurcations gives rise to a regular formation of axisymmetric vortices.

Despite all these experimental and numerical studies of intrinsic plume dynamics, the linear global stability of plumes appears to never have been investigated so far. The absolute/convective character of local instability has only been examined by Lombardi et al. [49] for the case of a planar plume in a stratified environment. The present study extends that analysis to round plumes, without the effect of background stratification, over a large range of Grashof and Prandtl numbers and for azimuthal wave numbers between 0 and 2. The Boussinesq approximation is employed in order to exclude the effect of the density ratio as an additional parameter.

The paper presents instability results for two different types of base flows: a general self-similar set of velocity and temperature profiles, typical for the flow field far away from a buoyancy source in section 2.2, and one specific case of a "forced" plume close to an inlet in section 2.3, which may also be characterized as a buoyant jet. Inside each of these sections, the base flow is described first, the linear stability problem is posed, and then the results of temporal and absolute/convective analysis are documented. The

physical discussion focuses principally on the temporal instability modes of the self-similar base flow sections 2.2.3 – 2.2.5. Conclusions are summarized in section 2.4.

2.2 Self-similar plume

2.2.1 Base flow

A quiescent incompressible fluid is considered, characterized by its temperature T_∞, density ρ_∞, kinematic viscosity ν, volumetric expansion coefficient α, thermal diffusivity κ and conductivity K. All fluid properties are assumed to be independent of temperature. A point source of heat flux Q is introduced into this quiescent medium. Buoyancy then induces a flow in the positive z-direction, opposite to the gravity $-g\mathbf{e}_z$.

The governing equations for primitive flow variables are written in the Boussinesq approximation [90]:

$$\nabla \cdot \mathbf{u} = 0, \tag{2.1a}$$

$$\frac{D\mathbf{u}}{Dt} = -\frac{\nabla p}{\rho_\infty} + \nu\nabla^2\mathbf{u} - \frac{(\rho-\rho_\infty)g}{\rho_\infty}\mathbf{e_z}, \tag{2.1b}$$

$$\frac{DT}{Dt} = \kappa\nabla^2 T, \tag{2.1c}$$

$$\frac{\rho-\rho_\infty}{\rho_\infty} = -\alpha(T-T_\infty). \tag{2.1d}$$

The pressure p includes the hydrostatic correction for $\rho_\infty gz$. Under a boundary-layer type approximation of slow streamwise variations, the steady self-similar base flow is governed by

$$\frac{\partial(ru_z)}{\partial z} + \frac{\partial(ru_r)}{\partial r} = 0, \tag{2.2a}$$

$$u_z\frac{\partial u_z}{\partial z} + u_r\frac{\partial u_r}{\partial r} = g\alpha(T-T_\infty) + \frac{\nu}{r}\frac{\partial}{\partial r}\left(r\frac{\partial u_z}{\partial r}\right), \tag{2.2b}$$

$$u_z\frac{\partial}{\partial z}(T-T_\infty) + u_r\frac{\partial}{\partial r}(T-T_\infty) = \frac{\kappa}{r}\frac{\partial}{\partial r}\left[r\frac{\partial}{\partial r}(T-T_\infty)\right], \tag{2.2c}$$

with boundary conditions

$$u_r = \frac{\partial u_z}{\partial r} = \frac{\partial}{\partial r}(T - T_\infty) = 0 \qquad \text{for } r = 0, \tag{2.3a}$$

$$u_r, u_z, (T - T_\infty) \to 0 \qquad \text{for } r \to \infty. \tag{2.3b}$$

Following [98], the similarity variables are chosen to be

$$\begin{aligned} \psi &= \nu z f(\eta), \\ T - T_\infty &= \frac{Q}{Kz} h(\eta), \\ \eta &= \frac{r}{z^{1/2}} \left[\frac{\alpha g Q}{K\nu^2}\right]^{1/4}, \end{aligned} \tag{2.4}$$

where ψ is a streamfunction defined by

$$u_z = \frac{1}{r}\frac{\partial \psi}{\partial r}, \quad u_r = -\frac{1}{r}\frac{\partial \psi}{\partial z}. \tag{2.5}$$

Substituting these variables into equations (2.2a)–(2.2c), one obtains

$$\left[\eta \left(\frac{f'}{\eta}\right)'\right]' = -\eta h - f\left[\frac{f'}{\eta}\right]', \tag{2.6}$$

$$\eta h' + Pr\, f h = 0, \tag{2.7}$$

where the prime denotes differentiation with respect to η, and the Prandtl number is defined as $Pr = \nu/\kappa$. The boundary conditions (2.3) become

$$h',\ f,\ (f'/\eta)' = 0 \quad \text{for } \eta = 0, \tag{2.8a}$$

$$h,\ f'/\eta \to 0 \quad \text{for } \eta \to \infty. \tag{2.8b}$$

With the above choice of variables for the similarity transformation, the following scales for length, velocity and temperature have been adopted:

$$R(z) = z^{1/2}\left(\frac{K\nu^2}{\alpha g Q}\right)^{1/4}, \tag{2.9a}$$

$$U = \left(\frac{\alpha g Q}{K}\right)^{1/2}, \tag{2.9b}$$

$$\Theta(z) = Q/Kz, \tag{2.9c}$$

where $R(z)$ defines a measure of the local plume radius. With these scales, the Grashof number is defined as

$$Gr = \frac{g\alpha\Theta(z)R^3(z)}{\nu^2} = \left(\frac{\alpha g Q z^2}{K\nu^2}\right)^{\frac{1}{4}}. \tag{2.10}$$

From equations (2.4, 2.5, 2.9), one obtains

$$u_z = U\overline{U}_z = U\frac{f'(\eta)}{\eta}, \tag{2.11}$$

$$u_r = U\overline{U}_r = U\frac{1}{Gr}\left(\frac{f'(\eta)}{2} - \frac{f(\eta)}{\eta}\right), \tag{2.12}$$

$$T - T_\infty = \Theta\overline{T} = \Theta(z)h(\eta). \tag{2.13}$$

Symbols with an overbar denote non-dimensional base flow quantities.

In order to have a unique solution, conservation of the heat flux at any axial location z is imposed. Furthermore, due to the self-similarity assumption, some boundary conditions in (2.8) are seen to become redundant. The following conditions are retained:

$$f'/\eta \to 0, \qquad as\ \eta \to \infty, \tag{2.14a}$$

$$f,\ (f'/\eta)' = 0, \qquad at\ \eta = 0, \tag{2.14b}$$

$$\int_0^\infty f'h\ d\eta = 1/(2\pi Pr). \tag{2.14c}$$

The base flow for any given Prandtl number can be derived by solving equations (2.6, 2.7, 2.14). A closed-form solution to these equations is known only for $Pr = 1$ and 2 [98, 6]. For all other values, the solution must be constructed numerically as follows [97]. Guess values for $f'(\eta)/\eta$ and for h are prescribed at $\eta = 0$, and the equations are integrated outward using a Runge–Kutta algorithm. The guess values for $f'(\eta)/\eta$ and h at $\eta = 0$ are improved based on the errors incurred in satisfying the boundary conditions (2.14a) and (2.14c). The resulting base flow profiles at Prandtl numbers between 0.1 and 10 are shown in figure 2.1. As Pr increases, both the temperature and the velocity mixing layers become thinner, measured by their vorticity thickness (see solid symbols in figure 2.1d). Yet, remarkably, the maximum value of the shear decreases at the same time (see open symbols in figure 2.1d).

2.2.2 Formulation of the linear stability problem

In the context of local stability analysis, the base flow is assumed to be locally parallel, i.e. the radial velocity u_r given by (2.12) is neglected, and perturbations are assumed to be of the form

$$(\tilde{u}_r, \tilde{u}_\theta, \tilde{u}_z, \tilde{P}, \tilde{T}) = \left[\hat{A}(\eta), \hat{B}(\eta), \hat{C}(\eta), \hat{P}(\eta), \hat{T}(\eta)\right] e^{i(kz+m\theta-\omega t)} + c.c. \tag{2.15}$$

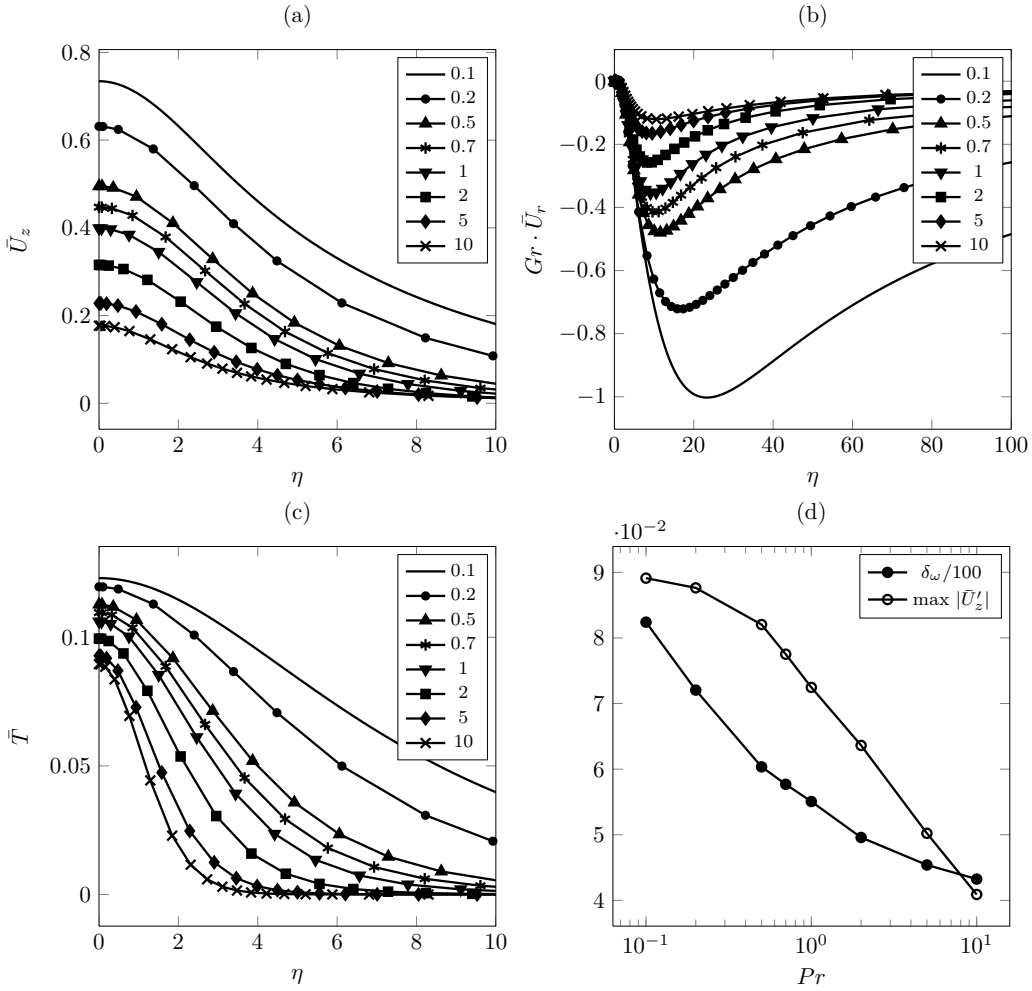

Figure 2.1: Self-similar base flow profiles, computed from equations (2.11)–(2.13) for various Prandtl numbers as specified in the legend. a) Axial velocity; b) radial velocity; c) temperature; d) vorticity thickness δ_ω of the velocity shear layer (scaled by a factor 1/100), and maximum value of the velocity gradient.

As in any local stability analysis, the locally parallel assumption can be taken as valid as long as the Grashof number is sufficiently large. The limitations of this assumption are critically discussed by Crighton & Gaster [19] in the context of jets. The axial wavenumber k, which in the following will simply be referred to as the wavenumber, as well as the frequency ω may take on complex values ($\omega = \omega_r + i\omega_i$), whereas the azimuthal wavenumber m is an integer. The nondimensional, linearized equations that govern the perturbations are obtained as

$$\eta\hat{A}' + \hat{A} + im\hat{B} + i\eta k\hat{C} = 0, \tag{2.16a}$$

$$i\left(k\overline{U}_z - \omega\right)\hat{A} = -\hat{P}' + \frac{1}{Gr}\left(\hat{A}'' + \frac{\hat{A}'}{\eta} - (k^2 + \frac{m^2+1}{\eta^2})\hat{A} - \frac{2im\hat{B}}{\eta^2}\right), \tag{2.16b}$$

$$i\left(k\overline{U}_z - \omega\right)\hat{B} = -\frac{im\hat{P}'}{\eta} + \frac{1}{Gr}\left(\hat{B}'' + \frac{\hat{B}'}{\eta} - (k^2 + \frac{m^2+1}{\eta^2})\hat{B} + \frac{2im\hat{A}}{\eta^2}\right), \tag{2.16c}$$

$$i\left(k\overline{U}_z - \omega\right)\hat{C} + \overline{U}'_z\hat{A} = -ik\hat{P} + \frac{\hat{T}}{Gr} + \frac{1}{Gr}\left(\hat{C}'' + \frac{\hat{C}'}{\eta} - (k^2 + \frac{m^2}{\eta^2})\hat{C}\right), \tag{2.16d}$$

$$i\left(k\overline{U}_z - \omega\right)\hat{T} + \overline{T}'\hat{A} = \frac{1}{PrGr}\left(\hat{T}'' + \frac{\hat{T}'}{\eta} - (k^2 + \frac{m^2}{\eta^2})\hat{T}\right) \tag{2.16e}$$

where $\overline{U}_z$ and $\overline{T}$ are defined in equations (2.11, 2.13).

In the limit $\eta \to \infty$, all perturbations vanish. The boundary conditions on the axis depend on m [41]:

$$\text{For } m = 0: \quad \hat{A}(0) = \hat{B}(0) = 0, \hat{C}'(0) = \hat{P}'(0) = \hat{T}'(0) = 0, \tag{2.17}$$

$$\text{for } m = \pm 1: \ \hat{A}(0) \pm i\hat{B}(0) = 0, \hat{A}'(0) = \hat{C}(0) = \hat{P}(0) = \hat{T}(0) = 0, \tag{2.18}$$

$$\text{for } |m| > 1: \quad \hat{A}(0) = \hat{B}(0) = \hat{C}(0) = \hat{P}(0) = \hat{T}(0) = 0, \tag{2.19}$$

$$\text{for all } m: \quad \hat{A}(\infty) = \hat{B}(\infty) = \hat{C}(\infty) = \hat{P}(\infty) = \hat{T}(\infty) = 0. \tag{2.20}$$

Equations (2.16) are solved numerically as an eigenvalue problem in ω for given values of k, and for a set of parameters (Pr, Gr, m). The problem is discretized using Chebyshev collocation on a finite interval $0 \leq \eta \leq \eta_\infty$. The value of η_∞ is prescribed to be at least 5000, and up to 50 000 for very low values of k and Gr. The domain is discretized with 300 - 350 points for all the cases considered here and the points are distributed using a mapping

function (equation 52 in Khorrami et al. [41]) which clusters the points close to the axis. Convergence with respect to resolution and domain size has been verified. In all cases, at most one unstable discrete eigenmode could be identified, i.e. all other eigenmodes appear to belong to the continuous spectrum. The convergence of the method is demonstrated in the figure 2.2 for two different parameters as an example.

2.2.3 Temporal analysis

Temporal analysis is performed on the self-similar base flow for Prandtl number values between 0.1 and 10, and for a range of Grashof numbers between 0.1 and 50 000. Azimuthal wavenumbers $m = 0, 1, 2$ are considered for each (Gr, Pr) combination, and the axial wavenumber k is varied such as to cover the entire unstable range. The principal result from these computations is a set of neutral stability curves, traced in figure 2.3, representing contour lines of zero growth rate. At nearly all Prandtl and Grashof numbers, the domain of instability of the helical $m = 1$ mode contains the other two modes. An exception to this rule is observed at $Pr \leq 0.2$, where instability sets in for axisymmetric $m = 0$ modes at slightly lower Grashof numbers than for $m = 1$ modes. Double-helical $m = 2$ modes are found to be unstable only over quite restricted parameter ranges; higher azimuthal wavenumbers are therefore not considered in this study. For $Pr \geq 5$, the double-helical mode is stable at all locations in the $k - Gr$ plane and therefore, there is no neutral curve to be shown for these Prandtl numbers in figure 2.3.

Another important observation from figure 2.3 is that the unstable range of wavenumbers in general has no finite lower limit, at least within the considered range of k. As the present numerical method requires k to be finite, a minimum value of 10^{-3} is used. In other words, the neutral curve for $m = 1$ in most cases has no lower branch, and it appears as if instability prevails even in the limit $k \to 0$, for Grashof numbers above a critical value Gr_c that is a function of the Prandtl number. Values of Gr_c, as a function of Pr, are reported in figure 2.4 for all m. In the absence of a lower branch, Gr_c is taken to be the critical value for $k = 10^{-3}$. The slight precedence of $m = 0$ over $m = 1$ at very low Prandtl numbers is visible in figure 2.4. Above $Pr = 0.2$, the self-similar plume will always first become unstable to helical perturbations as the Grashof number increases.

The neutral curve for $m = 0$ modes in figure 2.3 shows a peculiar behavior near a Prandtl number of unity. No unstable axisymmetric mode is found at $Pr = 1$, and the unstable ranges of Gr and k are very different for Prandtl

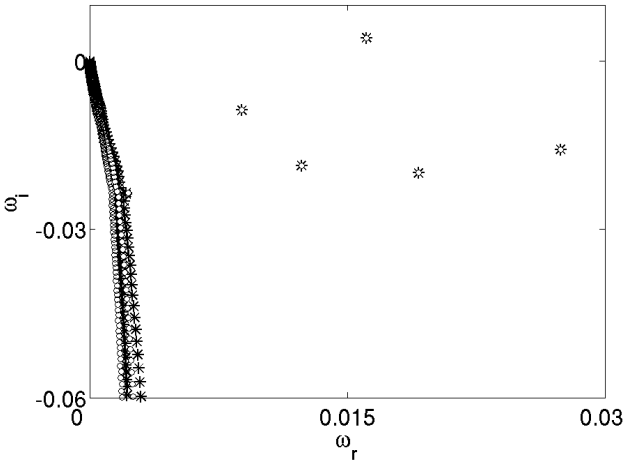

(a) $m = 1, Gr = 70, k = 0.12$

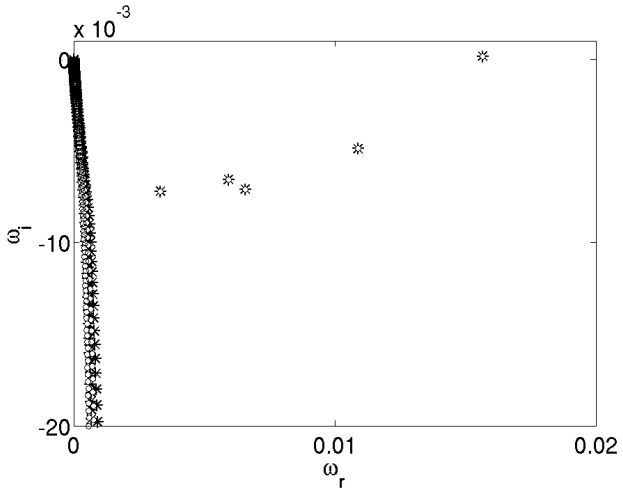

(b) $m = 0, Gr = 100, k = 0.05$

Figure 2.2: Eigenvalue spectrum for the base flow at Prandtl number of 2 for two different resolutions where asterisk markers correspond to 300 discretization points while open circles correspond to 350 points.

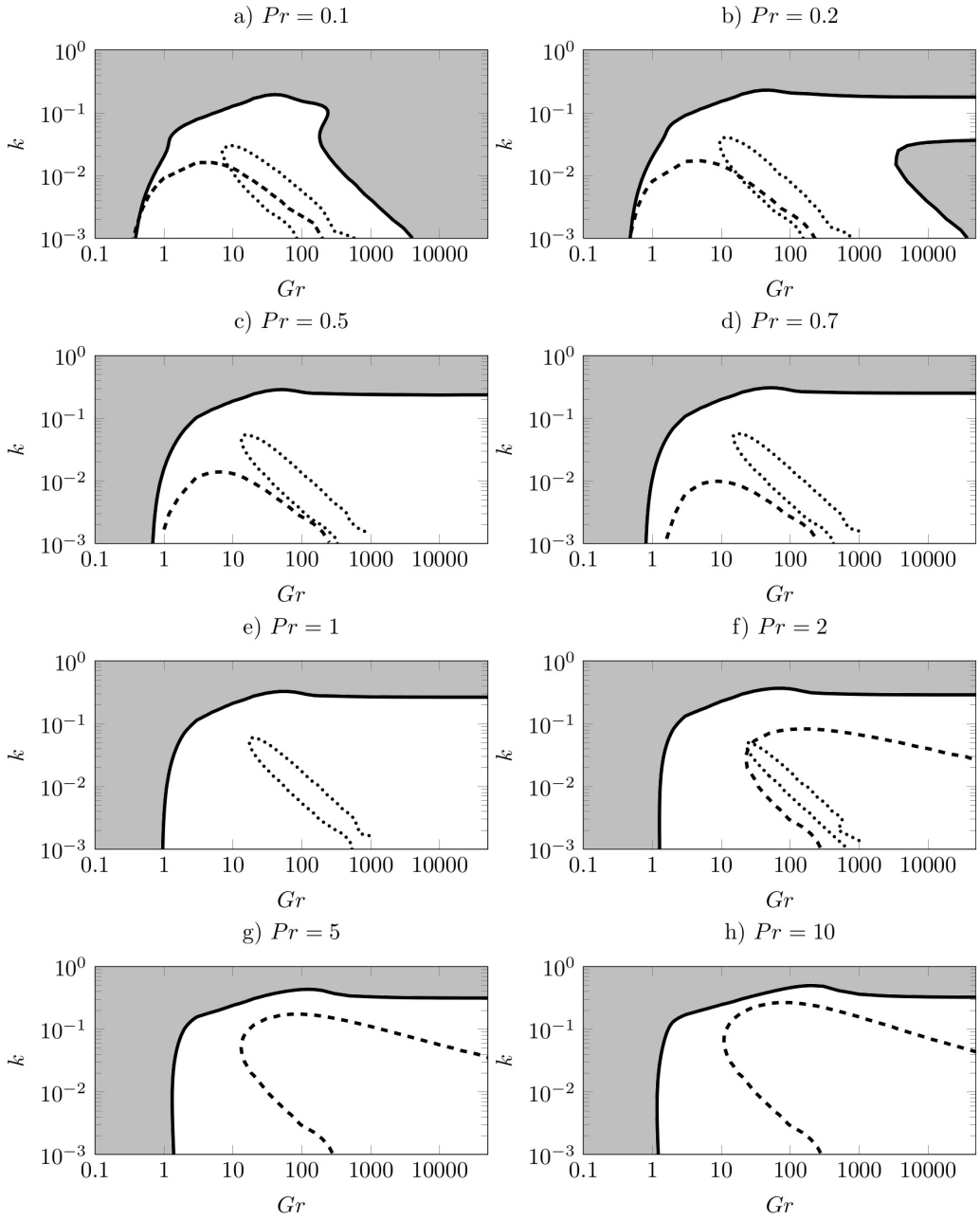

Figure 2.3: Neutral curves for azimuthal wavenumbers $m = 0$ (dashed), $m = 1$ (solid) and $m = 2$ (dotted) at various Prandtl numbers. Shaded regions indicate the parameter space over which the flow is stable to $m = 1$ perturbations.

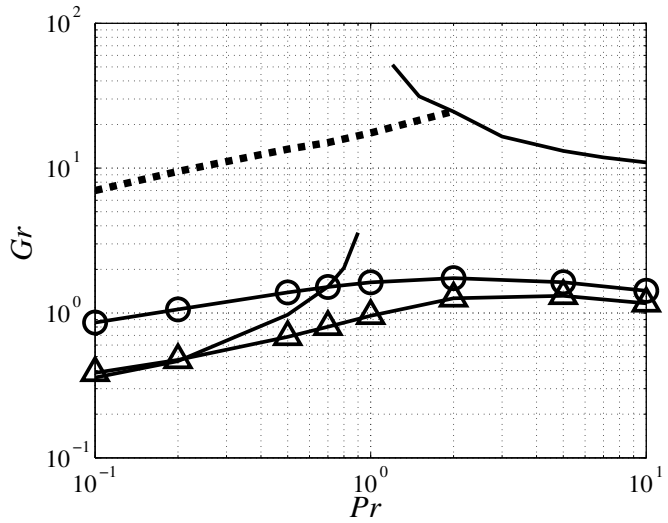

Figure 2.4: Critical Grashof number Gr_c for onset of temporal instability, as a function of Prandtl number Pr, for azimuthal wavenumbers $m = 0$ (solid), $m = 1$ (solid with triangular markers) and $m = 2$ (dashed). The solid line with circular markers denotes the transition from convective to absolute instability for $m = 1$ which will be discussed in section 2.2.6.

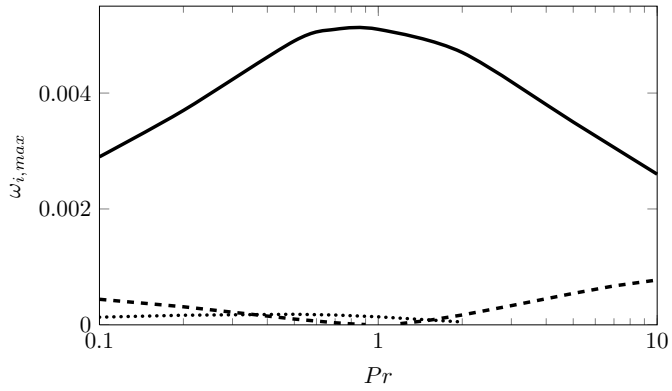

Figure 2.5: Maximum growth rate $\omega_{i,max}$, as a function of Prandtl number Pr, for azimuthal wavenumbers $m = 0$ (dashed), $m = 1$ (solid) and $m = 2$ (dotted).

numbers above and below $Pr = 1$. We associate this change with an observation in the context of an asymptotic expansion for large radial distances η. Such a study was attempted, but as it remained inconclusive, it is not presented here in detail. However, it can be reported that the analytically obtained solution for the potentially unstable $m = 0$ mode contains a factor $(Pr - 1)^{-1}$. The present numerical results suggest that this factor indeed causes a singularity at $Pr = 1$, separating two regimes of distinct character. The $m = 0$ mode is found to be always stable in the limit $Gr \to \infty$, which implies that the mode is stable to shear mechanisms. This is consistent with the Rayleigh criterion [2], which states that, for shear instability to exist in an axisymmetric inviscid non-buoyant flow, the relation

$$\eta_0 \left[\frac{\eta_0 \overline{U}'}{m^2 + k^2 \eta_0^2} \right]' = 0 \tag{2.21}$$

must be satisfied for some point $\eta_0 \in (0, \eta_\infty)$. For the base flow under consideration, expression (2.21) is not satisfied anywhere for the $m = 0$ mode. Therefore, instability is excluded in the inviscid (large Gr) limit by the Rayleigh criterion.

If the $m = 1$ mode is unstable over the largest range of parameters, nothing has been said so far about the strength of the instability. Figure 2.5 compares the maximum values $\omega_{i,max}$ reached by the growth rate over all wavenumbers and Grashof numbers, at $m = 0$, 1 and 2, for different Prandtl numbers Pr. Clearly, the $m = 1$ mode also dominates by this measure. The overall maximum is reached at $Pr = 1$, where the axisymmetric mode vanishes. A more detailed comparison is given for $Pr = 2$ in figure 2.6. Plots to the left show the variations of the growth rate ω_i with k for various values of Gr and for all m; diagrams to the right show the corresponding phase velocities $c_r = \omega_r / k$. The growth rates are consistently largest for $m = 1$ and smallest for $m = 2$.

The phase velocities display several characteristic trends. All axisymmetric modes (figure 2.6b) have phase velocities approximately equal to the base flow centerline velocity $\overline{U}(\eta = 0) = 0.315$ (see figure 2.1a). Unstable helical modes at high Grashof number ($m = 1$, figure 2.6d) display lower phase velocities, corresponding to base flow velocities in the shear layer. The values of c_r at $Gr = 50\,000$ are in fact within one percent of the base flow velocity $\overline{U}(\eta_0)$ at the radial station η_0 where the Rayleigh criterion (2.21) is fulfilled indicating that, in this limit, the instability is predominantly shear driven. Remarkably, at low values of k and Gr, the phase velocity for $m = 1$ drops sharply and even becomes negative. We do not have a clear explanation for

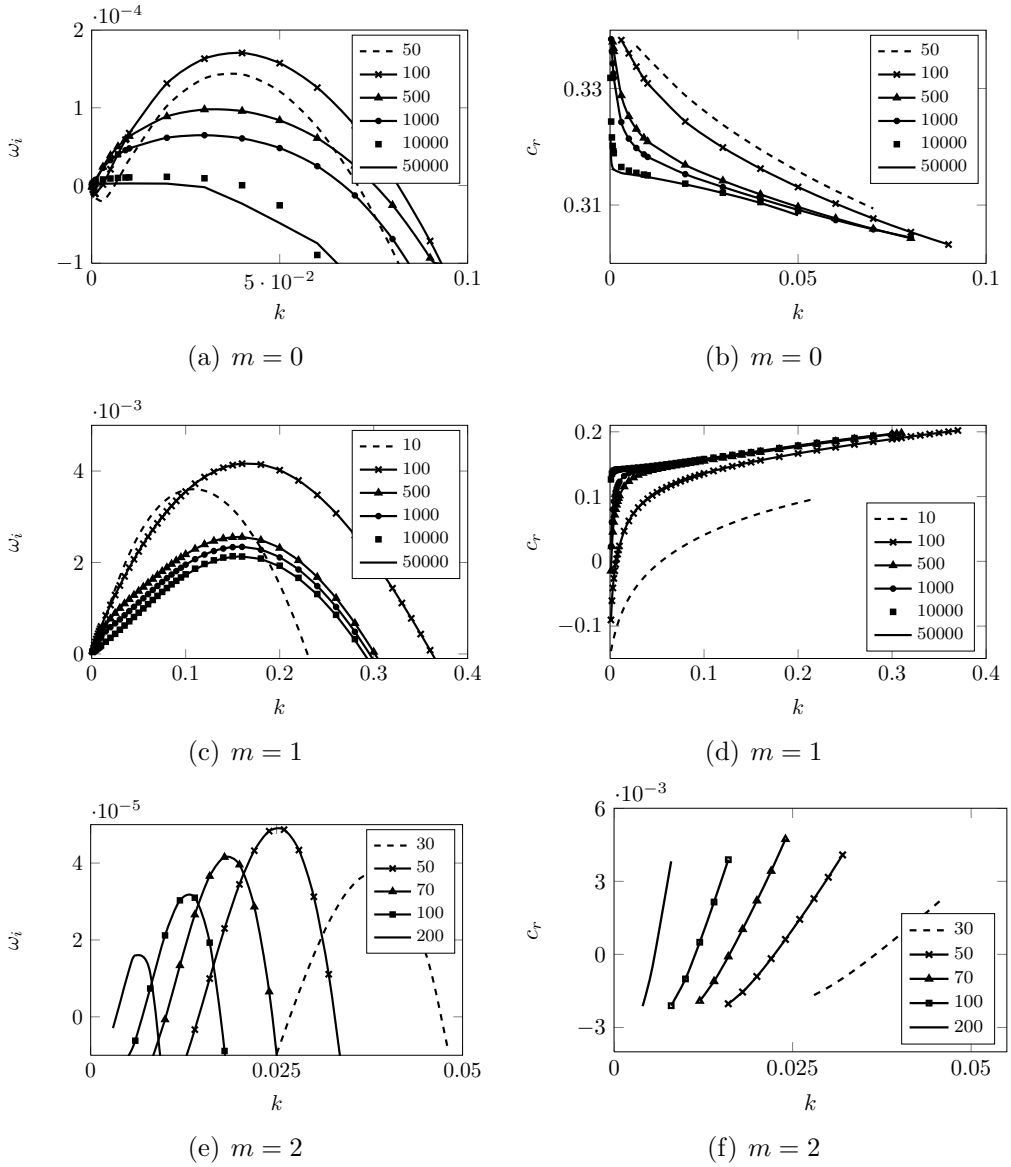

(a) $m = 0$ (b) $m = 0$

(c) $m = 1$ (d) $m = 1$

(e) $m = 2$ (f) $m = 2$

Figure 2.6: Variations of growth rate ω_i and phase velocity c_r with wavenumber k at a Prandtl number of 2 for various azimuthal wavenumbers m indicated below each plot and Grashof numbers indicated in the legend.

this behaviour at present. Unstable $m = 2$ modes (figure 2.6f) have phase velocities near zero.

2.2.4 Perturbation energy analysis

A useful characterization of the various physical mechanisms that affect the stability of the base flow can be inferred from the perturbation energy equation. Following the procedure outlined by Nacthsheim [62] and adopting the notation of Riley & Tveitereid [78], the following equations are obtained:

$$2\omega_i \int_0^\lambda \langle KE \rangle \, dz = \int_0^\lambda \langle M_u \rangle \, dz + \int_0^\lambda \langle B \rangle \, dz - \int_0^\lambda \langle D_u \rangle \, dz, \tag{2.22}$$

$$2\omega_i \int_0^\lambda \langle TE \rangle \, dz = \int_0^\lambda \langle M_t \rangle \, dz - \int_0^\lambda \langle D_t \rangle \, dz, \tag{2.23}$$

where

$$KE = \frac{\tilde{u}_r^2 + \tilde{u}_\theta^2 + \tilde{u}_z^2}{2}, \qquad TE = \frac{\tilde{T}^2}{2}, \tag{2.24a}$$

$$M_u = -(\overline{U}_z)' \tilde{u}_r \tilde{u}_z, \quad B = \frac{\tilde{u}_z \tilde{T}}{Gr}, \quad M_t = -\overline{T}' \tilde{u}_r \tilde{T}, \tag{2.24b}$$

$$D_u = \frac{\tilde{\chi} \cdot \tilde{\chi}}{Gr}, \qquad D_t = \frac{\nabla \tilde{T} \cdot \nabla \tilde{T}}{PrGr}, \tag{2.24c}$$

$$\langle (\,) \rangle = \int_0^\infty (\,) \eta d\eta, \quad \tilde{\chi} = \nabla \times \tilde{\mathbf{u}}, \quad \tilde{\mathbf{u}} = (\tilde{u}_r, \tilde{u}_\theta, \tilde{u}_z),$$

and $\lambda = 2\pi/k$ is the perturbation wavelength. While KE is the perturbation kinetic energy, note that TE only represents an *ad hoc* temperature norm; it is not rigorously defined as the thermal perturbation energy. The quantities D_u and D_t, which represent the dissipation terms associated with viscous and thermal diffusion respectively, are positive definite. The only terms that may give rise to a positive growth rate are therefore M_u, M_t and B. The symbol M_u stands for the work of Reynolds stresses, i.e. shear-related instability mechanisms, B denotes the work of buoyancy, and M_t represents the convective transfer of thermal energy between base flow and perturbations. All these production terms may take on positive or negative values.

In order to compute the various terms in (2.22, 2.23), the equations are cast in terms of complex eigenfunctions, leading to

$$2\omega_i \langle \mathscr{K} \rangle = \langle \mathscr{M}_u \rangle + \langle \mathscr{B} \rangle - \langle \mathscr{D}_u \rangle, \tag{2.25}$$

$$2\omega_i\langle\mathscr{T}\rangle = \langle\mathscr{M}_t\rangle - \langle\mathscr{D}_t\rangle, \tag{2.26}$$

with

$$\mathscr{K} = \frac{1}{2}(\hat{A}^*\hat{A} + \hat{B}^*\hat{B} + \hat{C}^*\hat{C}),\ \ \mathscr{M}_u = -\frac{\overline{U}'_z}{2}(\hat{A}^*\hat{C} + \hat{A}\hat{C}^*),\ \ \mathscr{B} = \frac{1}{2Gr}(\hat{C}^*\hat{T} + \hat{C}\hat{T}^*), \tag{2.27a}$$

$$\mathscr{D}_u = \frac{1}{Gr}\left[\frac{m^2|\hat{C}|^2}{\eta^2} + k^2|\hat{B}|^2 - \frac{km}{\eta}(\hat{B}^*\hat{C} + \hat{B}\hat{C}^*) + k^2|\hat{A}|^2 + |\hat{C}'|^2 - ik(-\hat{A}^*\hat{C}' + \hat{A}\hat{C}'^*)\right.$$
$$\left. + \frac{|\hat{B}|^2}{\eta^2} + |\hat{B}'|^2 + \frac{|\hat{A}|^2}{\eta^2} + \frac{\hat{B}^*\hat{B}' + \hat{B}\hat{B}'^*}{\eta} - im\frac{\hat{A}\hat{B}'^* - \hat{A}^*\hat{B}'}{\eta} - i\frac{\hat{A}\hat{B}^* - \hat{A}^*\hat{B}}{\eta^2}\right], \tag{2.27b}$$

$$\mathscr{T} = \frac{|\hat{T}|^2}{2},\quad \mathscr{M}_t = -\overline{T}'\frac{\hat{A}^*\hat{C} + \hat{A}\hat{C}^*}{2},\quad \mathscr{D}_t = \frac{1}{PrGr}\left[|\hat{T}'|^2 + (k^2 + \frac{m^2}{\eta^2})|\hat{T}|^2\right]. \tag{2.27c}$$

An asterisk denotes the complex conjugate. Riley & Tveitereid [78] gave identical expressions for the special case $m = 1$. A typographical error in their expression for $\mathscr{B}$ is corrected above.

Based on the kinetic energy equation (2.25), the separate contributions of buoyancy, shear and viscosity to the flow instability can be quantified. Viscosity is always stabilizing in the present context and will not be further considered. The relative importance of buoyancy and shear for the helical mode instability in the (Gr, k) plane is indicated in figure 2.7 by the contour lines $\langle\mathscr{B}\rangle/\langle\mathscr{M}_u\rangle = \{0.2, 5\}$. Clearly, buoyancy-related effects dominate at low Grashof numbers, and shear effects dominate at high Grashof numbers. This is expressed in equation (2.27a) by the scaling $\mathscr{B} \sim Gr^{-1}$. The shear-dominated character of the instability at high Grashof numbers is consistent with the accurate prediction of a critical point in η_0, from the Rayleigh criterion (2.21), as observed in section 2.2.3. Figure 2.7 shows that buoyancy effects gain importance as the wavenumber is lowered. Markers in figure 2.7 indicate the (Gr, k) combination at which the highest growth rate is reached, as reported in figure 2.5. Invariably, this combination is found in a region where buoyancy and shear contributions are of similar importance.

Figure 2.8 compares eigenfunction shapes of two representative modes in the buoyancy-dominated and shear-dominated regimes, respectively, for a Prandtl number $Pr = 2$. The shear mode (thin lines) has significant amplitudes only inside the plume, with peaks in several quantities at the critical point $\eta_0 = 3.2$, whereas the buoyancy mode (thick lines) spreads over a much larger radial distance.

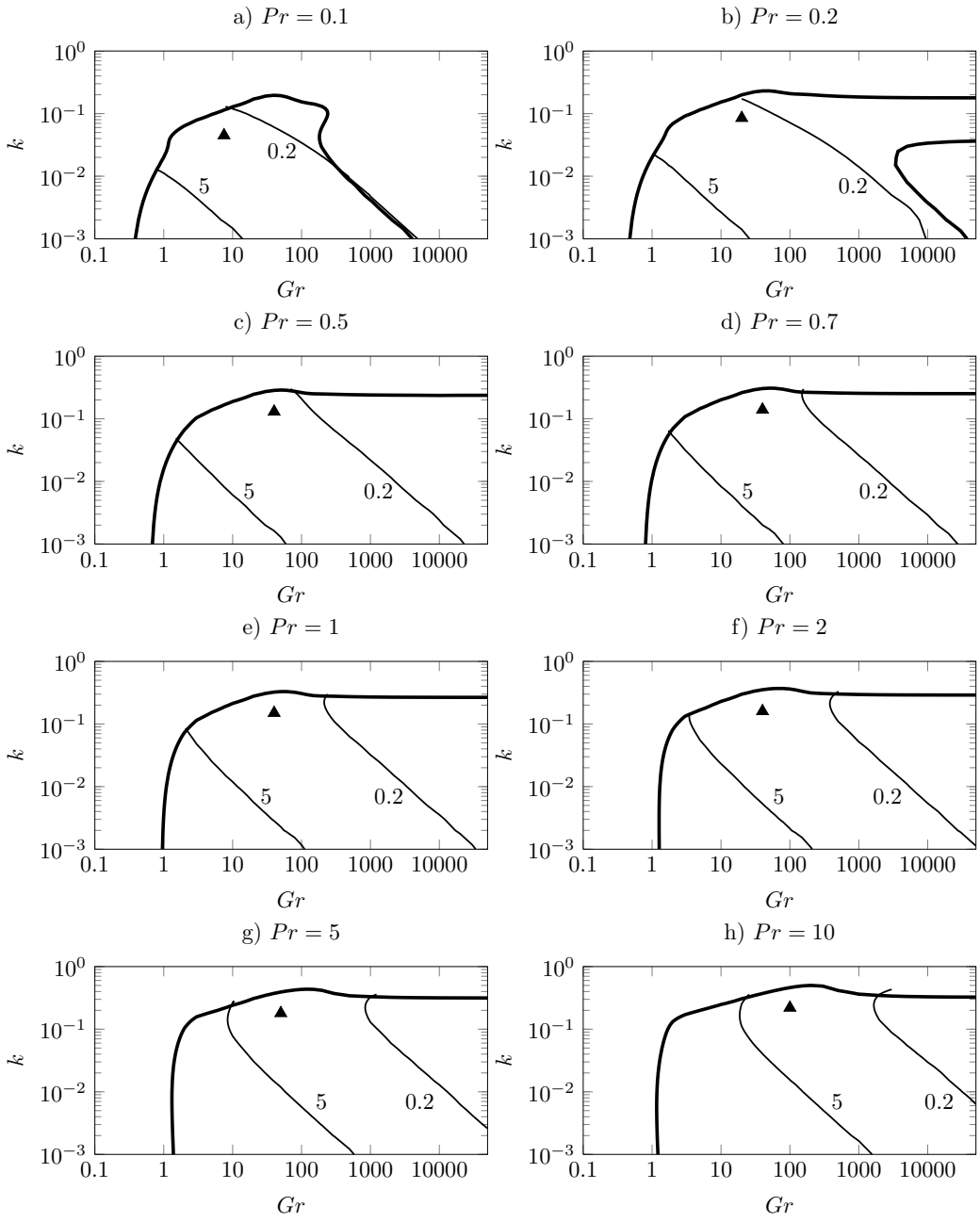

Figure 2.7: Neutral curves for $m = 1$ mode instability (thick lines), alongside contour lines $\langle \mathscr{B} \rangle / \langle \mathscr{M}_u \rangle = \{0.2, 5\}$ (thin lines), at various Prandtl numbers. Triangles mark the point of maximum growth rate $\omega_{i,max}$.

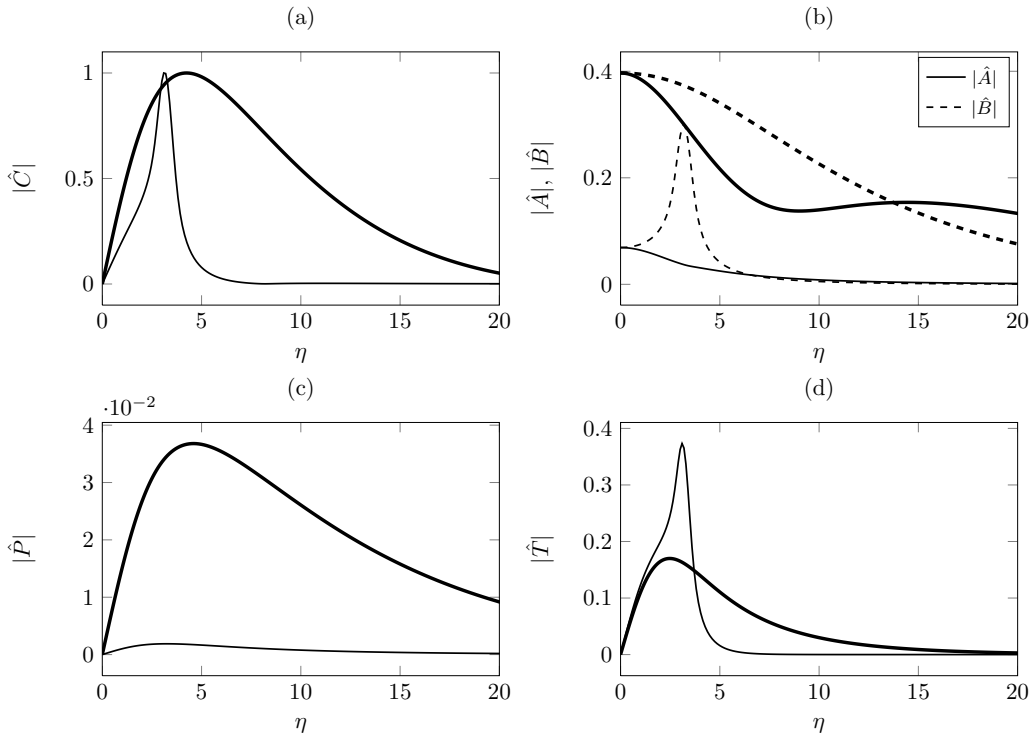

Figure 2.8: Unstable eigenfunctions (absolute values) for $m = 1$, $k = 0.1$ and $Pr = 2$. Thick lines: buoyancy-dominated regime $Gr = 5$; thin lines: shear-dominated regime $Gr = 50\,000$. The eigenfunctions are normalized with respect to their maximum in the axial velocity.

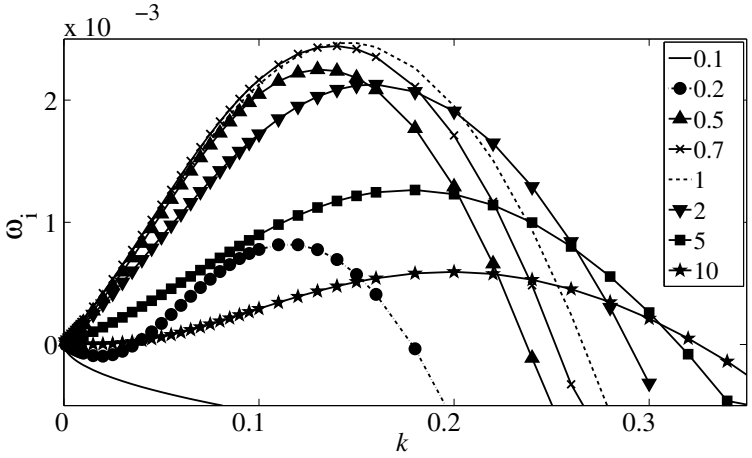

Figure 2.9: Growth rate as a function of wavenumber, for $m = 1$, various Prandtl numbers as indicated in the legend, and $Gr = 50\,000$.

Figure 2.7 indicates that a higher Prandtl number favors a stronger dominance of buoyancy contributions to the instability at low and moderate Grashof numbers. This trend may be partially ascribed to a base flow effect, as the base flow shear reduces with increasing Pr (see figure 2.1d). In addition, the thermal dissipation of temperature perturbations is decreased (equation 2.27c), which should lead to an increase in $\langle \mathscr{B} \rangle$ (equation 2.27a).

In the high Grashof number regime, the unstable range of wavenumbers increases steadily with Pr, as seen in figures 2.3 and 2.7. This is easily understood from the fact that the vorticity thickness of the base flow decreases monotonically with the Prandtl number, as thinner shear layers are unstable to a larger band of wavenumbers. However, the complete stabilization at $Pr = 0.1$ cannot be explained from obvious shear instability arguments. The growth rate variations with wavenumber, at $m = 1$ and for various Prandtl number values, are shown in figure 2.9. The trends for $Pr \geq 1$ are fully consistent with classical results for non-buoyant inviscid shear layers: the unstable range of k grows with increasing Pr, because the vorticity thickness shrinks; the maximum growth rate diminishes with increasing Pr, because the maximum base flow velocity gradient decreases. Yet the latter trend is reversed for $Pr < 1$, and lower Prandtl numbers stabilize the flow. It is observed, but not shown here, that the Reynolds stress $\tilde{u}_z \tilde{u}_r$ decreases in amplitude at low Prandtl numbers.

Both the $m = 0$ and the $m = 2$ modes are stable in the inviscid limit of high Grashof numbers (figure 2.3). According to equation (2.27a), the buoyant energy production term vanishes as Gr grows large, and the only

potential source of instability is the shear term $\mathscr{M}_u$. However, the Rayleigh criterion (2.21) for a cylindrical geometry predicts that all self-similar base flows in the present study are stable with respect to $m = 0$ perturbations in the inviscid limit. It is confirmed numerically that the term $\langle \mathscr{M}_u \rangle$ takes on negative values for $m = 0$ under all conditions. Any growth of axisymmetric perturbations must be attributed to buoyancy effects.

Shear-related instability of $m = 2$ perturbations cannot be categorically ruled out on the basis of the Rayleigh criterion; however, earlier studies [2, 58] on non-buoyant and weakly buoyant jets have found $m = 2$ modes to be stable in such flows in the presence of viscosity. Comparison of $\langle \mathscr{M}_u \rangle$ and $\langle \mathscr{B} \rangle$ in the present calculations consistently identify the buoyant term as the dominant contributor to $m = 2$ instability.

2.2.5 Buoyancy-driven instability mechanism

While the shear-driven instability at high Grashof numbers is among the most classical phenomena described in the literature (see Drazin & Reid [23]), the buoyancy-driven instability that prevails in the low Grashof regime deserves some further attention. Insights into the physical mechanisms are sought from an examination of the instability eigenfunctions.

Figure 2.10 presents contour plots of some relevant perturbation quantities for the case $m = 1$, $Pr = 1$, $Gr = 5$ and $k = 0.01$. A Cartesian (y, z) plane is shown for convenience, where y is identical with the radial coordinate η at positive values, and $y = 0$ is the centerline of the plume. Perturbation streamlines are superposed on temperature perturbation contours in figure 2.10(a). Note that the true streamlines in $m = 1$ geometry are three-dimensional; for the purpose of our argument, the azimuthal velocity component may be safely ignored, as it does not contribute to the convection of base flow quantities. It is clear from figure 2.10(a) that the perturbation velocity convects hotter fluid from the centerline, where the base flow temperature is maximum, into the regions of positive perturbation temperature. We may therefore interpret this temperature perturbation as an effect of the velocity perturbation. In turn, this temperature perturbation induces a vertical motion (figure 2.10b) that reinforces the circulating flow in the sense of the streamlines. This action of buoyancy therefore constitutes a positive feedback on the fluid motion, providing a plausible scenario for an instability mechanism. Figure 2.10(c) demonstrates that the resulting buoyancy work B is indeed positive everywhere for the chosen parameter combination, i.e. the phase relation between $\tilde{T}$ and $\tilde{u}_z$ is such that the feedback mechanism is

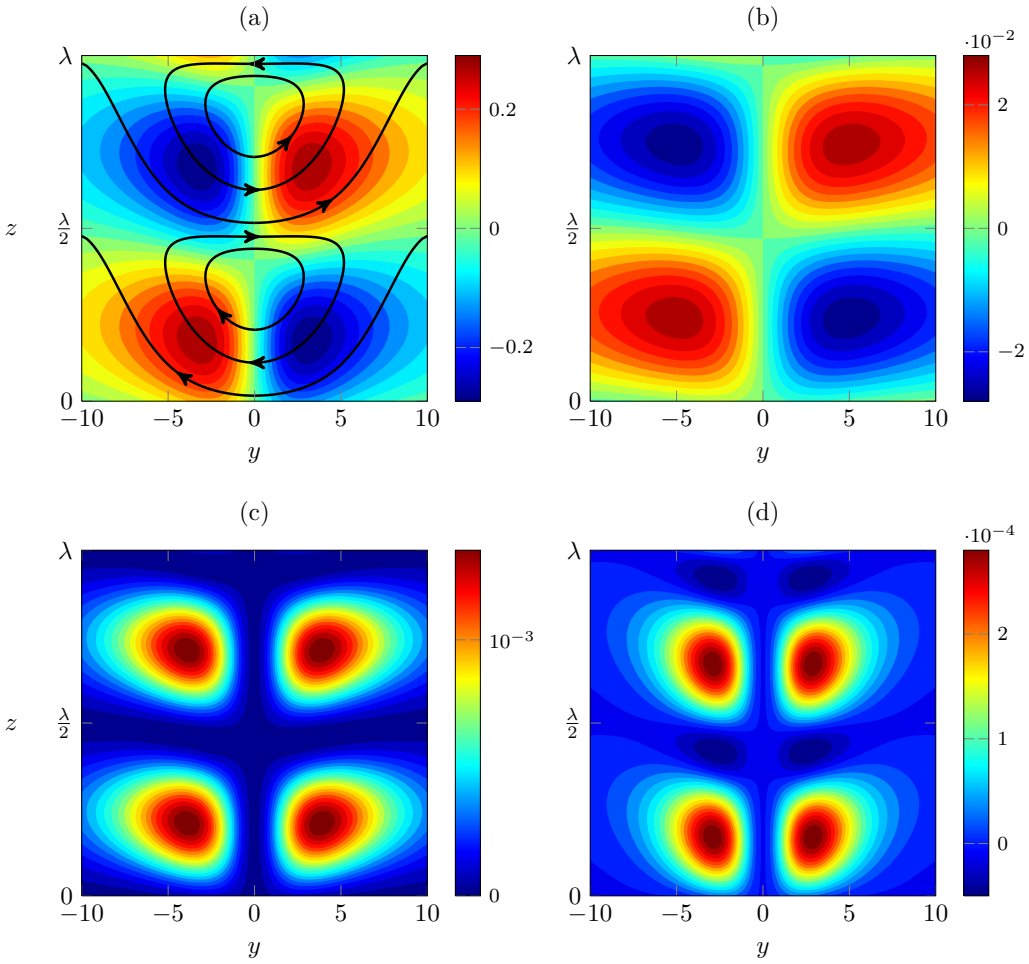

Figure 2.10: Helical $m = 1$ eigenmode for parameters $Pr = 1$, $Gr = 5$ and $k = 0.01$. All quantities are shown in a Cartesian plane, with the centerline of the plume at $y = 0$. a) Perturbation isotherms and perturbation streamlines; b) perturbation axial velocity; c) buoyancy work B; d) shear-related work M_u.

destabilizing at every point in space. The shear-related work M_u is visualized in figure 2.10(d). Its net contribution is clearly positive, and therefore destabilizing, but the amplitudes are lower than those of the buoyancy work by a factor of around 5.

A similar situation for an unstable $m = 0$ mode is shown in figure 2.11. Parameters $Pr = 10$, $Gr = 50$ and $k = 0.1$ are chosen, corresponding to a comparatively strong axisymmetric instability. The perturbation streamlines show the presence of counter-rotating toroidal vortices. These vortices deform the column of hot fluid, thus leading to positive and negative values of the temperature perturbation along the axis, which in turn drive the vertical convection. Stationary vortices would lead to maximum temperature perturbation in the hyperbolic points, whereas buoyant acceleration would be most efficient with the temperature maxima just between two hyperbolic points. In the case shown in figure 2.11, the position of temperature maxima is between these two extremes; by virtue of this compromise, temperature perturbations grow due to convection of base flow temperature, and at the same time they drive the convection rolls.

2.2.6 Absolute/convective analysis

Everyday observations for example in cigarette smoke (figure 107 in *An album of fluid motion* by van Dyke [92]), suggest that laminar plumes may spontaneously bifurcate to a sate of periodic oscillations. Such behaviour is usually linked to an absolute instability of the steady flow state. The possibility of absolute instability, in parameter regimes defined by m, Gr and Pr, is investigated in this section.

The absolute instability mode for a given base flow profile in section 2.2.1 is identified by tracking a saddle point of the complex-valued function $k(\omega)$, according to the Briggs–Bers criterion (see Huerre & Monkewitz [35]). This analysis turns out to be very delicate in the present flow case, and the following procedure is found to yield the most accurate results: values of ω are computed on a grid of complex k values in an area of interest in the k-plane. The group velocity v_g associated with these modes is obtained as detailed in Lesshafft & Marquet [47]. The saddle point, characterized by zero group velocity, is then identified through successive mesh refinements. A convergence criterion $|v_g| < 10^{-4}$ is used for all results presented here. The absolute instability mode is characterized by its complex frequency ω_0 and its complex wavenumber k_0. If the growth rate $\omega_{0,i}$ is positive, the flow is absolutely unstable.

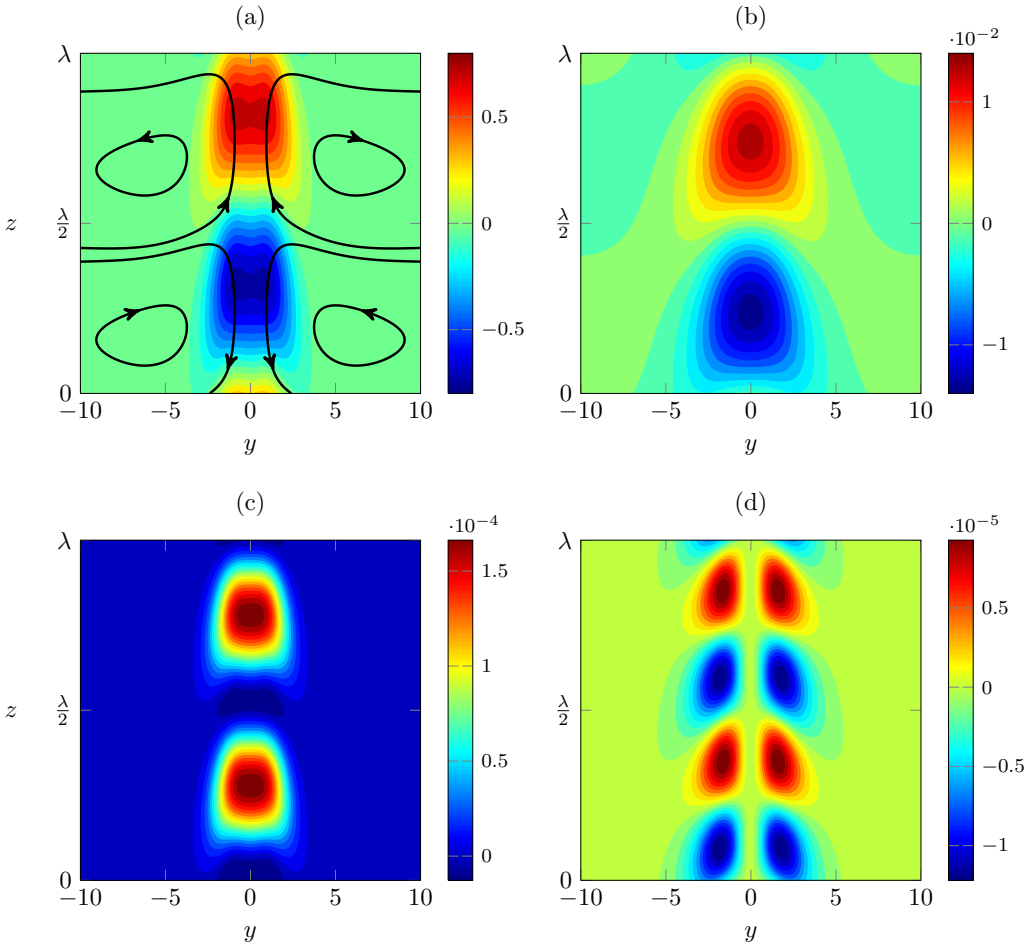

Figure 2.11: Axisymmetric $m = 0$ eigenmode for parameters $Pr = 10$, $Gr = 50$ and $k = 0.1$. All quantities are shown in a Cartesian plane, with the centerline of the plume at $y = 0$. a) Perturbation isotherms and perturbation streamlines; b) perturbation axial velocity; c) buoyancy work B; d) shear-related work M_u.

Absolute instability is found to occur at Grashof numbers above a critical value, $Gr > Gr_{ca}$, which depends on the Prandtl number. The absolute mode is *always* found to be of the helical type ($m = 1$). Indeed, no convective-absolute transition is observed for any other azimuthal modes over the investigated parameter range. The variation of the critical Grashof number $Gr_{ca}(Pr)$ is presented in figure 2.4 (circles). Its value is close to unity at all Prandtl numbers.

The variations of ω_0 and k_0 with Grashof number at $Pr = 1$ are shown in figure 2.12. Transition from convective to absolute instability (sign change in $\omega_{0,i}$) takes place at $Gr_{ca} = 1.627$, and the flow remains absolutely unstable at all $Gr > Gr_{ca}$. As the Grashof number is proportional to the square root of vertical distance (2.10), this transition station will typically be located close to the source. However, both ω_0 and k_0 asymptote to zero as the Grashof number tends to infinity. Very small values of ω and k correspond to perturbations that are quasi-steady in time and quasi-constant in z, and such perturbation modes are difficult to track numerically. The analysis is therefore limited to Grashof number values below 1000.

The near-zero asymptotic variations of both ω_0 and k_0 are rather peculiar, and require a validation. In particular, it must be ascertained that no other undetected saddle point might dominate the long-time dynamics. Three-dimensional time-resolved direct numerical simulations are therefore performed, using the *linear* evolution equations for perturbations of a parallel base flow. The code of Deloncle [22] has been adapted to the present problem; typical simulations run over 2000 time steps on 10^8 grid points. Starting from an initial impulse, the long-time perturbation wavepacket is computed, and the absolute mode is recovered from a spatio-temporal Fourier transform [21]. The (ω_0, k_0) values obtained with this procedure, represented as triangles in figure 2.12, clearly validate the results found from direct solution of eigenvalue problems. The eigenvalue procedure is significantly cheaper, and more accurate.

Variations of the absolute growth rate $\omega_{0,i}$ with Grashof number at various Prandtl numbers are displayed in figure 2.13. The qualitative features do not vary significantly with Pr; in all cases, absolute instability sets in at a Grashof number around 1, and the maximum growth rate is reached shortly after. The overall maximum of $\omega_{0,i}$ is found at $Pr = 1$. The spatial distribution of the eigenfunction for the absolutely unstable $m = 1$ helical mode at absolute wavenumber k_0 is shown in figure 2.14 for two different Grashof numbers at $Pr = 1$. It is seen that the phase relation between the temperature and velocity perturbations strongly resemble the temporal results shown in figure

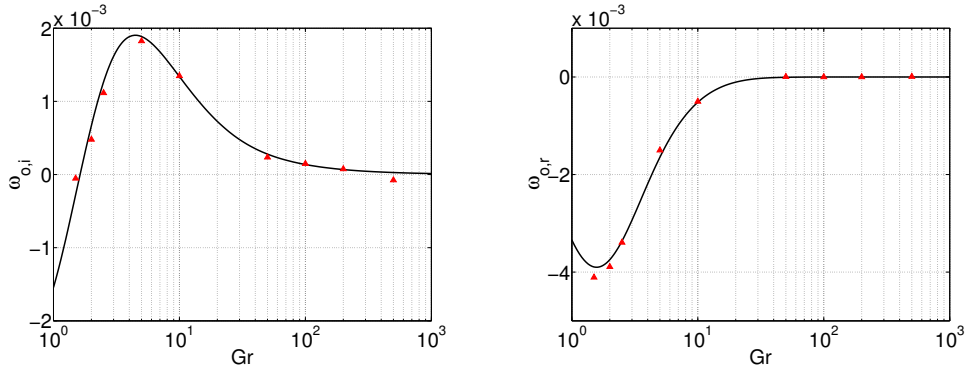

(a) $\omega_{0,i}$

(b) $\omega_{0,r}$

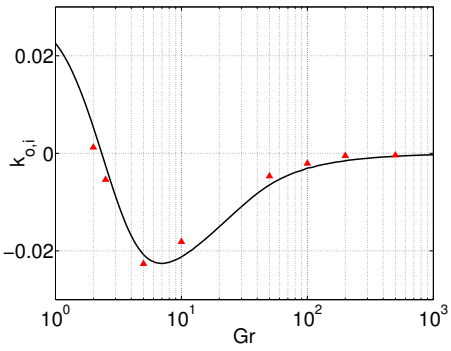

(c) $k_{0,i}$

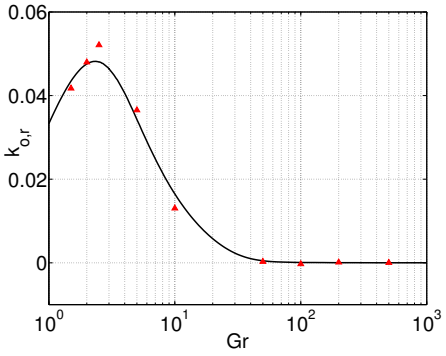

(d) $k_{0,r}$

Figure 2.12: Variations of ω_0 and k_0 as a function of Grashof number at Prandtl number of unity. Results obtained from eigenvalue problems (—) and from direct numerical simulation of the linear impulse response (▲).

2.10 indicating a similar mechanism for destabilization of the absolute mode. Note that in order to show this correlation between velocity and temperature perturbation clearly, the imaginary part $k_{0,i}$ is set to zero. However, as the imaginary part of k_0 only contributes to the amplitude, the arguments about the phase continue to hold for the actual case of $k_{0,i} \neq 0$.

We surmise that this quasi-steady absolute mode is the local trace of a non-oscillatory *global* instability mode. If this is the case, then the spatially developing plume is expected to first bifurcate to a new steady flow state that breaks the axial symmetry; in analogy to axisymmetric wakes [69, 56], the result would be a deflected steady flow, which may exhibit secondary oscillatory instabilities. This scenario remains to be confirmed in future studies.

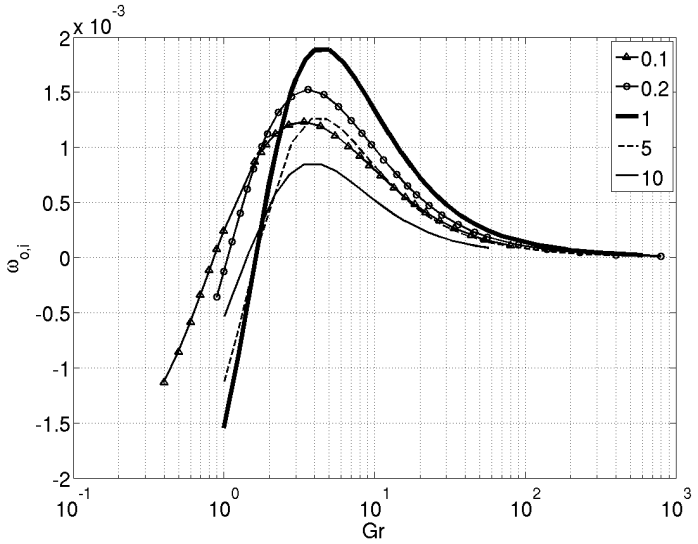

Figure 2.13: Absolute growth rate variations $\omega_{0,i}(Gr)$ at various Prandtl numbers Pr given in the legend.

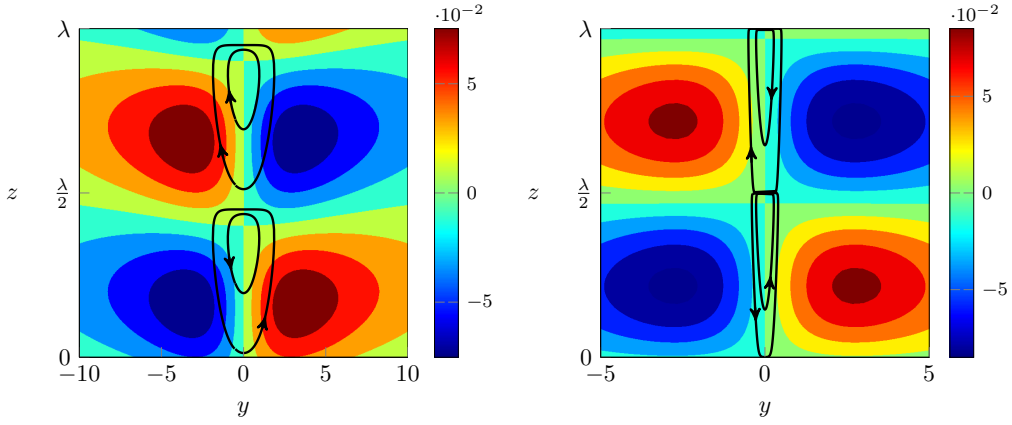

(a) $Gr = 4$ (b) $Gr = 100$

Figure 2.14: Perturbation isotherms and perturbation streamlines for helical $m = 1$ eigenmode for $Pr = 1$ at the absolute wavenumber k_0 at two different Grashof numbers: a) $Pr = 1$, $Gr = 4$ and b) $Pr = 1$, $Gr = 100$. All quantities are shown in a Cartesian plane, with the centerline of the plume at $y = 0$.

2.3 Plume near a finite-sized inlet

2.3.1 Base flow

The self-similar base flows investigated in the preceding section represent laminar plumes far away from the buoyancy source. However, as it has been found that the convective-absolute transition takes place at low Grashof number, i.e. close to the source, the global dynamics are likely to be determined in the *near-source* region. The defining characteristic of the self-similar flow regime is its generality; upstream of this region, the base flow profiles depend on the specific form of the buoyancy source. Such a source may be a heated body, a jet of light fluid, a flame, or other; and any such configuration would require an individual analysis. In this section, the particular case of hot fluid issuing from a circular orifice is examined. The fluid is injected at $z = 0$ with finite momentum; the initial flow near the orifice is therefore a buoyant jet, characterized by a thin shear layer at $z = 0$. With increasing distance from the orifice, the velocity profiles are more and more dominated by the momentum that is induced by buoyancy, and the influence of the inlet condition is lost. The self-similar profile shapes of section 2.2.1 are asymptotically recovered.

Specifically, the following flow configuration is considered: a fluid is injected with a prescribed velocity $u(r)$ and temperature $T(r)$ from an inlet of radius R into a quiescent ambient at temperature T_∞ and density ρ_∞. Non-dimensionalizing the governing equations (2.1) with the centerline axial velocity at the inlet U_c and centerline temperature difference $(T_c - T_\infty)$ at the inlet, one obtains

$$\nabla \cdot \mathbf{u} = 0, \tag{2.28a}$$

$$\frac{D\mathbf{u}}{Dt} = -\nabla p + \frac{1}{Re}\nabla^2 \mathbf{u} + Ri(T - T^*_\infty)\mathbf{e_z}, \tag{2.28b}$$

$$\frac{DT}{Dt} = \frac{1}{PrRe}\nabla^2 T, \tag{2.28c}$$

where $T^*_\infty = T_\infty/(T_c - T_\infty)$, Richardson number $Ri = g\alpha R(T_c - T_\infty)/U_c^2$ and $Re = U_c R/\nu$. These are related to the Grashof number from section 2.2 as $Gr = RiRe^2$. All quantities are made non-dimensional with U_c as the velocity scale, R as the length scale and $(T_c - T_\infty)$ as the temperature scale. The base flow is computed by a Newton–Raphson method, using finite elements as implemented in FreeFEM++ [25], on a domain of size 20×200

in the radial and streamwise directions. Analytic inflow profiles of the form

$$u(r, z = 0) = T(r, z = 0) - T^*_\infty = sech^{20}\left[20\ r^{20}\right], r \leq 2, \tag{2.29a}$$
$$u(r, z = 0) = T(r, z = 0) - T^*_\infty = 0, r > 2. \tag{2.29b}$$

are prescribed at $z = 0$, which give a momentum thickness of the shear layer and the thermal mixing layer that is 1/46 of the orifice radius. At the lateral boundary, vertical velocity is set to zero and temperature is set to T_∞, while a Neumann condition for the radial velocity allows an entrainment influx. Stress-free boundary conditions are imposed at the outlet, and axial symmetry is enforced at $r = 0$. Domain convergence is verified on a grid of dimension 50×300.

A single configuration is presented here, with parameters $Pr = 1$, $Re = 100$ and $Ri = 1$. The base flow is documented in figure 2.15(a) – 2.15(d), which shows axial velocity and temperature as a function of r at several streamwise positions, as well as the streamwise development of the centerline values. The asymptotic behaviour of the latter characterizes the approach towards the self-similar solution. It is stressed again that all following results pertain to the very specific case that is considered here as an example.

2.3.2 Temporal analysis

The linearized instability equations for a local analysis are identical to equations (2.16), with the substitutions $\eta \to r$, $Gr \to Re$ in the viscous and thermal diffusion terms, and $Gr^{-1} \to Ri$ in the buoyancy term.

The temporal growth rates as functions of real-valued k are plotted in figure 2.16 for several vertical positions. Unlike in the self-similar flow, where the helical $m = 1$ mode is clearly dominant, axisymmetric and helical modes present similar growth rates in the near-inlet region. The axisymmetric mode then stabilizes rapidly with increasing distance from the inlet. At large distance z, the results are fully consistent with those obtained earlier for the self-similar region: the $m = 1$ growth rates at $z = 190$ from figure 2.16 match the corresponding values from the self-similar analysis, at $Gr = 630$ and appropriately rescaled, within 1%.

2.3.3 Absolute/convective analysis

Absolute frequency and wavenumber, as functions of the vertical distance z, are displayed in figure 2.17 for the helical $m = 1$ mode. Also in the

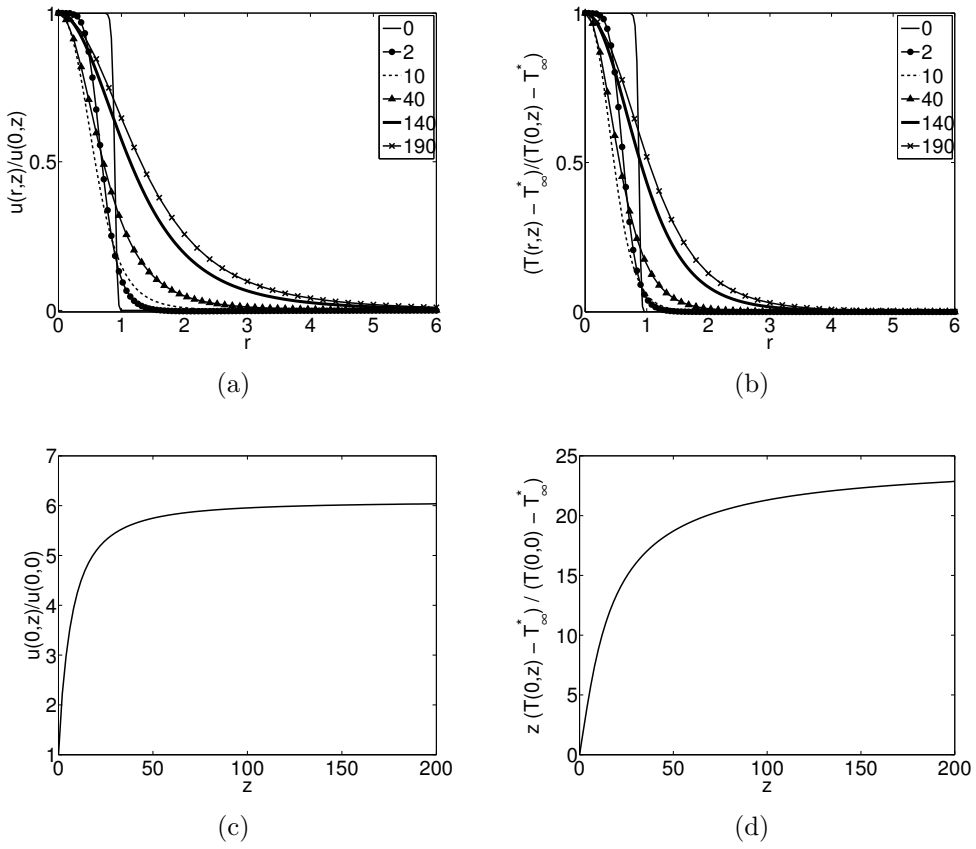

Figure 2.15: Velocity and temperature evolution of the base flow. (a) Radial profiles of axial velocity at various streamwise positions indicated in the legend; (b) corresponding radial profiles of temperature; (c) streamwise development of centreline velocity; (d) streamwise development of centreline temperature.

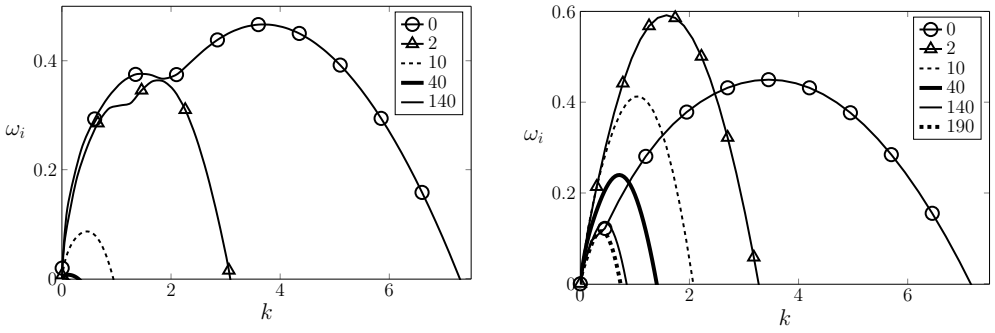

(a) $m = 0$ (b) $m = 1$

Figure 2.16: Temporal growth rate $\omega_i(k)$ for (a) $m = 0$, (b) $m = 1$ at various streamwise locations z given in the legend, for the spatially evolving base flow shown in figure 2.15(a).

present case of a spatially developing base flow with thin initial shear layer, axisymmetric perturbations are found to never become absolutely unstable, just like in the self-similar analysis of section 2.2.6. However, the helical mode is seen to be absolutely unstable everywhere along z, starting from the inlet. The values of ω_0 and k_0 are again very small, especially at larger distances from the inlet. Saddle points could be reliably identified only down to $z = 40$, due to numerical difficulties that arise when ω_0 and k_0 tend to zero.

All absolute/convective instability results presented herein are markedly different from what is typically found in jet flows [44]. If the present analysis is consistent with classical jet results, the described helical absolute instability must arise from the Boussinesq-type buoyancy term. The saddle point represented in figure 2.17 is the most unstable one, which therefore dominates the long-time behaviour of the linear impulse response, but other saddle points arise as well. Several such saddle points in the complex ω- and k-planes are displayed in figure 2.18. Open symbols represent saddle points of the inlet profile if buoyancy is completely removed. The addition of buoyancy (filled symbols) shifts the positions of these points moderately, but most importantly it creates a new saddle point, with higher absolute growth rate than all others, that has no counterpart in the non-buoyant case. This is the saddle point that has been described above, the one that causes absolute instability in the plume; it follows that the occurrence of this absolute instability is conditioned by the presence of buoyancy.

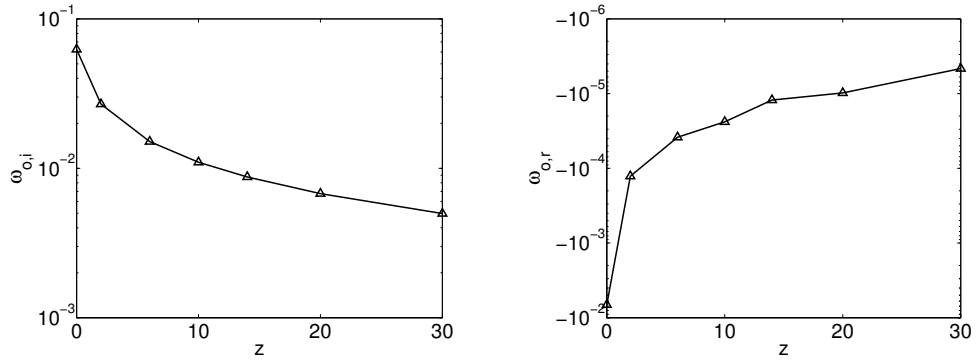

(a) $\omega_{0,i}$

(b) $\omega_{0,r}$

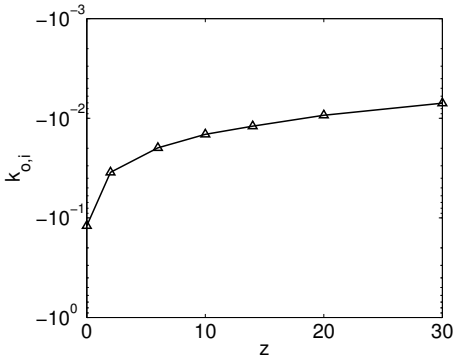

(c) $k_{0,i}$

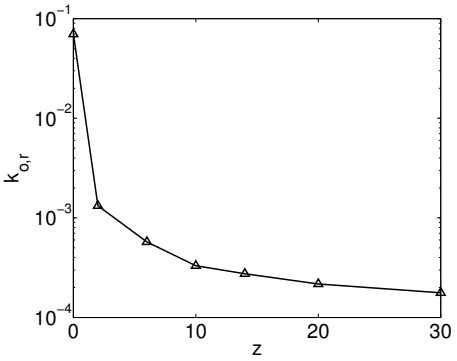

(d) $k_{0,r}$

Figure 2.17: Variation of absolute frequency ω_0 and wavenumber k_0 with streamwise distance.

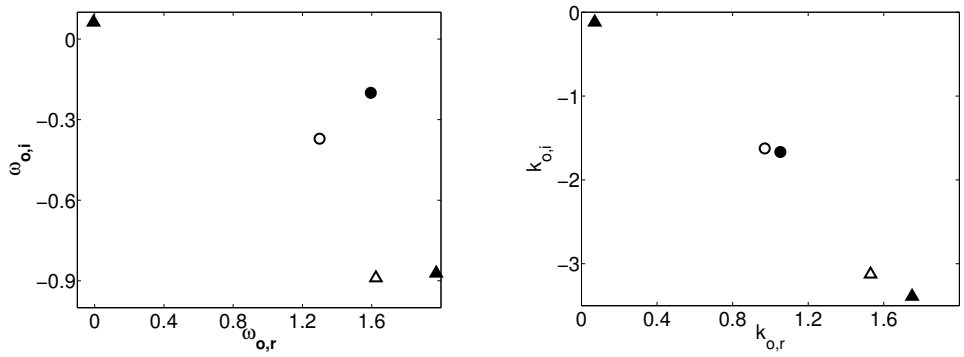

(a) (b)

Figure 2.18: Saddle point locations computed for the evolving base flow at the inlet ($z = 0$), with parameters $Ri = 1$, $Pr = 1$ and $Re = 100$; (a) in the complex ω-plane; (b) in the complex k-plane. Filled symbols: with buoyancy; open symbols: without buoyancy. Circles: $m = 0$ (axisymmetric); triangles: $m = 1$ (helical).

2.4 Conclusions

The local linear stability of laminar plumes has been investigated, first in full detail in the self-similar region far away from the buoyancy source, then for one particular setting in the vicinity of an orifice from which exits a hot fluid with imposed initial momentum. The temporal stability properties as well as the absolute instability modes have been documented over a wide range of Grashof and Prandtl numbers, under the Boussinesq approximation, and the physical origin of the flow instability has been discussed. Shear and buoyancy are the two ingredients that may give rise to instability. With rare exceptions, helical perturbation modes ($m = 1$) have been found to dominate the temporal instability properties of the self-similar flow under all conditions. It has been shown for these modes that buoyancy effects drive the instability at low Grashof numbers and wavenumbers, whereas shear effects are prevalent in the high Grashof number and wavenumber regime. The strongest temporal instability is found at intermediate parameters, where both effects are of comparable strength. For axisymmetric perturbations, the Rayleigh criterion precludes an instability of the self-similar flow profiles by shear mechanisms alone; therefore a destabilization through buoyancy effects is necessarily involved whenever an $m = 0$ mode becomes unstable.

Interpretations for the physical mechanisms behind buoyancy-driven in-

stability in plumes have been proposed, both for $m = 0$ and $m = 1$ perturbations, based on the observed eigenfunction shapes. Temperature perturbations induce vortical structures through buoyancy, which in turn convect the base flow temperature. Instability arises if the temperature perturbations and the convection rolls co-operate constructively.

Instability persists down to Grashof number values near unity. However, as instability appears to set in at inaccessibly low values of k, the critical value of the Grashof number could not be determined unambiguously for most Prandtl numbers. It cannot be excluded that zero-wavenumber perturbations are unstable in the limit of zero Grashof number. Yet this question is quite irrelevant for practical purposes, as the parallel base flow hypothesis is not valid at low Grashof numbers and long wavelengths.

Absolute instability arises in all self-similar profiles above a critical Grashof number close to unity. The absolute mode is always of the $m = 1$ type; absolute instability of axisymmetric perturbations has not been observed at any parameter setting in the present investigation. The dominant absolute instability mode is linked to a saddle point of the dispersion relation that only exists due to the buoyancy term in the governing equations; it vanishes if the buoyancy term is removed. However, both the frequency and the wavenumber of the absolute mode are nearly zero, which characterizes this mode as being quasi-steady and quasi-constant in the vertical flow direction. An ad hoc interpretation of this result, which will have to be confirmed in future studies, is that this absolute mode is associated with a non-oscillatory global instability of the spatially developing plume. Such an instability is expected to provoke a first bifurcation that leads to a non-axisymmetric steady flow state.

Classical theory predicts that the dynamics of globally unstable flows are dominated by the local properties near the transition station from convective to absolute instability. The results obtained for self-similar plumes suggest that this transition station indeed lies far upstream (at small local Grashof number), where the parallel flow hypothesis may not be well justified. This consideration motivated the investigation of the flow region near a finite-sized inlet. The principal conclusions from this extended investigation are consistent with the observations in the self-similar region. Absolute instability is found only for helical $m = 1$ perturbations, and indeed throughout the flow domain, starting from the inlet, with very small values of the absolute frequency and wavenumber. The temporal analysis shows that axisymmetric perturbations, although convective, exhibit similarly strong growth rates as their helical counterparts in the jet-like region very close to the inlet. The

self-similar behaviour is recovered at a far distance from the inlet.

The dominance of helical modes in the jet-like region, where the shear layer is thin compared to the inlet radius, contrasts with the absolute instability of axisymmetric perturbations in non-buoyant light jets [59]. Experiments as well as numerical simulations of plumes with strong density differences, e.g. Subbarao & Cantwell [85], Satti & Agrawal [79] and Jiang & Luo [40], also show evidence of axisymmetric self-excited instability structures. A major difference between those settings and the present investigation lies in the use of the Boussinesq approximation in this paper, which is valid only for small density variations. In particular, the Boussinesq approximation eliminates the baroclinic torque term from the dispersion relation, which has been shown to be responsible for the occurrence of absolute instability in light jets by Lesshafft & Huerre [44]. We hope to be able to report soon on our ongoing investigation about the influence of the density ratio on the instability characteristics of plumes.

Errata

The equations 2.24c, 2.28b and 2.29 are corrected for notations from the original article. Also, the labels for figures 2.15 and 2.17 are correspondingly corrected for notations.

2.5 DNS of the linear impulse response

In section 2.2.6, the absolute/convective analysis was performed through two methods. One is to track the saddle point in the complex k-plane while the second method is to perform a linear DNS of the evolution of the perturbation filed. The methodology of the saddle point computation was detailed in section 2.2.6 and the details of the DNS, which were omitted there, are presented in this section.

In order to perform the time evolution of the perturbation field added to the base flow, the governing equations are cast into a form convenient for computations. Governing equations (2.1a) – (2.1d) are non-dimensionalized with the scales defined in equations (2.9) and the equations are then linearized about the base flow. Furthermore, a spatial Fourier transform is performed on the equations to obtain

$$\frac{\partial \underline{\tilde{\mathbf{u}}} e^{\mathbf{k^2}t/Gr}}{\partial t} = \mathbf{P}(\mathbf{k}) \left[\underline{\left(\tilde{\mathbf{u}} \times \mathbf{\Omega} + \bar{U}_z \mathbf{e_z} \times \tilde{\mathbf{\Sigma}} \right)} + \frac{\tilde{T}}{Gr} \right] e^{\mathbf{k^2}t/Gr}, \tag{2.30a}$$

$$\frac{\partial \underline{\tilde{T}} e^{\mathbf{k^2}t/(PrGr)}}{\partial t} = \left[-i\mathbf{k} \cdot \left(\underline{\bar{U}_z \mathbf{e_z} \tilde{T} + \bar{T} \tilde{\mathbf{u}}} \right) \right] e^{\mathbf{k^2}t/(PrGr)}, \tag{2.30b}$$

where $\underline{()} = \iiint ()e^{-i(k_x x + k_y y + k_z z)} \mathrm{d}x\mathrm{d}y\mathrm{d}z$ is the Fourier transform in Cartesian space, $\mathbf{k} = (k_x, k_y, k_z)$ is the wavenumber, $\mathbf{\Omega} = \nabla \times (\bar{U}_z \mathbf{e_z})$ is the vorticity of the parallel base flow, $\mathbf{\Sigma} = \nabla \times \tilde{\mathbf{u}}$ is the vorticity of the perturbation velocity field and $\mathbf{P}(\mathbf{k})$ is the tensor $P_{ij} = \delta_{ij} - k_i k_j / \mathbf{k^2}$ denoting the projection operator. These equations are then integrated in time using 4^{th} order Runge-Kutta scheme. The method employed for this purpose in this study is similar to the one previously used in the study of jets [66], wakes [21, 20] and stratified flows [4, 22]. A parallel version of the code to perform the above procedure was developed by Deloncle [22] and the same has been used in this study. Note that in this DNS study, a Cartesian frame of reference is chosen as it is easier to perform pseudo-spectral analysis.

For most simulations, the periodic box with dimensions $L_x \times L_y \times L_z = 96 \times 96 \times 1536$ which is discretized with $N_x \times N_y \times N_z = 192 \times 192 \times 3072$ equally spaced points with a time step of $\delta t = 2.0$ is used and 2000 time steps are performed to reach the long-time asymptotic state. The results obtained are verified for grid independence. As an initial perturbation, divergence free, zero mean white noise is added over a small cuboidal domain of size $2.5 \times 2.5 \times 5.5$ centered around the point $(0.5L_x, 0.5L_y, 0.3L_z)$ to simulate the impulse and the flow field is then marched in time. After performing the prescribed number of time steps, the data are then analyzed to obtain the

asymptotic behaviour along each ray as described by Delebende & Chomaz [20].

In brief, the data obtained from the DNS are analyzed as follows: Firstly, the DNS data obtained in Fourier space are inverted into real space. Then, a Hilbert transform of the data followed by decomposition into the azimuthal components are carried out. Further, the streamwise Fourier transform followed by an integration of the amplitude in the radial direction are performed in the case of temporal analysis, while the amplitude of the perturbation along each *ray* is computed by integration along the radial direction and the temporal evolution of the amplitude along these rays are tracked in the case of absolute/convective analysis. However, Hilbert transform is known to have difficulty distinguishing between wavepackets when their boundaries overlap [33]. In the current flow field, temporal analysis of section 2.2.3 shows the existence of at least three wavepackets corresponding to $m = 0$, $m = 1$ and $m = 2$. Therefore, instead of the Hilbert transform, the Hilbert-Huang transform was applied for few cases to verify the results obtained via Hilbert transform. The results from both methods were matching closely for the case of $m = 0$ and $m = 1$. The double-helical mode $m = 2$ however, could not be analyzed through either of these transformations possibly due to its extremely low growth rate in comparison to $m = 0$ and $m = 1$ (refer to the temporal growth shown in figure 2.5). Performing the DNS for longer time is likely to help analyze this double-helical mode as its amplitude would grow larger in comparison to the initial white noise. Such an investigation was not attempted in the present study because such low growth rates are unlikely to be significant for the dynamics of the flow.

2.6 Singularity at Pr = 1

It can be seen from figure 2.4 in section 2.2.3, that for the axisymmetric mode $m = 0$, the critical Grashof number Gr_c steeply increases and approaches ∞ as $Pr \to 1$. At $Pr = 1$, no discrete eigenvalue could be obtained for $m = 0$ for all the range of parameters considered. In order to understand this rather strange behaviour, attempts are made to prove the non-existence of an eigenfunction for $m = 0$ at $Pr = 1$. For this, the large η behaviour of the eigenfunction is studied.

Following are the perturbation equations (2.16a) – (2.16e) cast into radial velocity - radial vorticity formulation, valid for any azimuthal wave number

at any radial location:

$$ik\left[\overline{U}-\frac{\omega}{k}\right]\mathcal{T}\phi-\frac{ik(k^2\eta^2+m^2)}{\eta}\left[\frac{\eta\overline{U}'}{k^2\eta^2+m^2}\right]'\phi=$$
$$\frac{1}{Gr}\left[\mathcal{T}^2\phi-2km\mathcal{T}\Omega-k\left(\frac{2m^2\hat{T}}{k^2\eta^2+m^2}+\eta\hat{T}'\right)\right], \tag{2.31a}$$

$$ik\left[\overline{U}-\frac{\omega}{k}\right]\Omega-\frac{i}{\eta}\left[\frac{m\overline{U}'}{k^2\eta^2+m^2}\right]\phi=$$
$$\frac{1}{Gr}\left[\mathcal{S}\Omega+\frac{2km\mathcal{T}}{(k^2\eta^2+m^2)^2}\phi-\frac{m\hat{T}}{k^2\eta^2+m^2}\right], \tag{2.31b}$$

$$ik\left[\overline{U}-\frac{\omega}{k}\right]\hat{T}+\frac{i\overline{T}\phi}{\eta}=\frac{1}{PrGr}\left[\hat{T}''+\frac{\hat{T}'}{\eta}-\hat{T}\left(k^2+\frac{m^2}{\eta^2}\right)\right], \tag{2.31c}$$

where

$$\mathcal{T}=\frac{k^2\eta^2+m^2}{\eta}\frac{d}{d\eta}\left(\frac{\eta}{k^2\eta^2+m^2}\right)\frac{d}{d\eta}-k^2,$$
$$\mathcal{S}=\frac{1}{\eta(k^2\eta^2+m^2)}\frac{d}{d\eta}\left[\eta(k^2\eta^2+m^2)\frac{d}{d\eta}\right]-k^2,$$
$$\hat{u}_r=\frac{i\phi}{\eta},$$
$$\hat{u}_\theta=\frac{-m\phi'}{k^2\eta^2+m^2}+k\eta\Omega,$$
$$\hat{u}_z=\frac{-k\eta\phi'}{k^2\eta^2+m^2}-m\Omega.$$

For $Pr=1$, the base flow is of the form

$$\overline{U}=\frac{\alpha_1}{\alpha_2+\eta^4},\qquad \overline{T}=\frac{\alpha_3}{\alpha_4+\eta^6}$$

while for $Pr=2$, it is

$$\overline{U}=\frac{\alpha_5}{\alpha_6+\eta^4},\qquad \overline{T}=\frac{\alpha_7}{\alpha_8+\eta^8}$$

where the α_j are real valued coefficients. In the limit $\eta\to\infty$, the base flow quantities and their derivatives are set to zero and the equations (2.31a) -

(2.31c) simplify to the form

$$-i\omega\mathcal{T}\phi = \frac{1}{Gr}\left[\mathcal{T}^2\phi - 2kn\mathcal{T}\Omega - k\eta\hat{T}'\right] \tag{2.32a}$$

$$-i\omega\Omega = \frac{1}{Gr}\left[\mathcal{S}\Omega\right] \tag{2.32b}$$

$$-i\omega\hat{T} = \frac{1}{PrGr}\left[\hat{T}'' - k^2\hat{T}\right] \tag{2.32c}$$

where

$$\mathcal{S} = \frac{d^2}{d\eta^2} - k^2,$$

$$\mathcal{T} = \frac{d^2}{d\eta^2} - k^2.$$

In addition to the base flow quantities, all the coefficients of ϕ, Ω, $\hat{T}$ and their derivatives which are of the form $1/\eta$ and higher powers of $1/\eta$ have been neglected.

These above equations can be solved for any m. An analytical solution for this set of equations is obtained by using Mathematica as

$$\hat{T}(\eta) = p_1 e^{-\lambda_1} + p_2 e^{\lambda_1} \tag{2.33}$$

$$\Omega(\eta) = e^{-\lambda_2}\left[\frac{c_1}{2} - \frac{c_2\eta}{2\lambda_2}\right] + e^{\lambda_2}\left[\frac{c_1}{2} + \frac{c_2\eta}{2\lambda_2}\right] \tag{2.34}$$

$$\begin{aligned}
\phi(\eta) = {} & \frac{e^{-\lambda_1}kp_1}{\omega^3 Pr^2 Gr^3(Pr-1)^2}\left[2ik^2(2Pr-1)+\omega PrGr(-2-\lambda_1+Pr(4+\lambda_1))\right] \\
& + \frac{e^{\lambda_1}kp_2}{\omega^3 Pr^2 Gr^3(Pr-1)^2}\left[2ik^2(2Pr-1)+\omega PrGr(-2+\lambda_1+Pr(4-\lambda_1))\right] \\
& - \frac{ie^{\pm\lambda_3}}{2k\omega Gr}\left[2km(kc_1 \pm c_2)+\zeta(kc_3 \pm c_4)-(kc_5 \pm c_6)\right] \\
& + \frac{ie^{\pm\lambda_2}\eta}{2\omega Gr\lambda_2\zeta}\left[km\omega Gr\left\{\frac{\lambda_2}{\eta}(-2i \pm \lambda_2)c_1 - i(\pm 3-\lambda_2)c_2\right\}\right. \\
& \qquad \left. + 2k^3 m\left(\frac{\lambda_2}{\eta}c_1 \pm c_2\right) + \zeta\left\{k^2\left(\frac{\lambda_2}{\eta}c_3 \pm c_4\right) - \left(\frac{\lambda_2}{\eta}c_5 \pm c_6\right)\right\}\right]
\end{aligned} \tag{2.35}$$

where, $\lambda_1 = (\sqrt{k^2 - i\omega PrGr})\eta$, $\lambda_2 = (\sqrt{k^2 - i\omega Gr})\eta$, $\lambda_3 = k\eta$ and $\zeta = k^2 - i\omega Gr$ and p_1, p_2, c_1, ... , c_6 are constant coefficients and can be complex valued functions of m, Pr, k and Gr.

In equation (2.35), it is seen that there are exponential terms with coefficients of the form $1/(Pr-1)$. The hypothesis is that, this $1/(Pr-1)$ singularity is somehow nullified for the case of $m=1$ and we obtain a non-trivial spectrum and eigenfunctions. Whereas, for the case of $m=0$, it does not seem to happen, i.e, no discrete eigenmode could be observed numerically for $m=0$ at $Pr=1$. Again, it is important to note that the explanation is far from being exact as the dependence of p_1 and p_2 with Pr and m could not be obtained. With the current analysis, only a passing comment could be made.

Chapter 3

Global stability of buoyant jets and plumes

In the previous chapter, the dynamics of a plume under the Boussinesq approximation was discussed and the presence of an absolute instability in the helical mode was established. However, nothing was said about the global dynamics of the flow. In experiments on helium jets, self-excited axisymmetric puffing is observed whereas, the axisymmetric mode in a Boussinesq plume is at most convectively unstable. To address this conundrum, linear global stability analyses of plumes and buoyant jets are performed.

In this chapter, it is demonstrated that the large scale self-sustained oscillations reported in experiments [85, 9] are a result of a global instability and the oscillation frequencies predicted by the linear global stability analysis corroborate quantitatively with the experiments. Further, through a local spatio-temporal analysis, these global dynamics are shown to be intrinsic in nature. The role of various terms such as shear, buoyancy, viscosity, etc towards instability are quantified through a linear sensitivity analysis of the global eigenvalue, endogeneity.

As in the previous chapter, presentation will be in the form of an article which will soon be submitted to *Journal of Fluid Mechanics* for review. A small portion of this work was presented at *The International Conference on Jets, Wakes and Separated Flows* held in Stockholm, 16 – 18 June, 2015. The corresponding contribution to the proceedings is attached as an Appendix to this dissertation.

Global stability of buoyant jets and plumes

R. V. K. Chakravarthy, Lutz Lesshafft and Patrick Huerre
Laboratoire d'Hydrodynamique (LadHyX), CNRS – École Polytechnique,
91128 Palaiseau, France

under preparation, for submission to *Journal of Fluid Mechanics*

Abstract

The linear global stability of laminar buoyant jets and plumes is investigated under the low Mach number approximation. For Richardson numbers in the range $10^{-4} \leq Ri \leq 10^3$ and density ratios $S = \rho_\infty/\rho_{jet}$ between 1.05 and 7, only axisymmetric perturbations are found to exhibit global instability. These linear predictions agree well with previous experimental studies on the dynamics of helium jets. By varying the Richardson number over seven decades, the effect of buoyancy on the dynamics and on the base flow is explored in detail, and the distinct dynamics of buoyant jets and plumes is demonstrated. Through a sensitivity analysis, based on the recently proposed endogeneity formalism, the relative contributions of various terms to the global eigenvalue are computed, thereby leading to the identification of different destabilizing forces. The base flow shear provides the largest destabilization effect at low Richardson numbers while the buoyancy force is dominant at large Richardson numbers. The existence of unstable global eigenmodes is consistent with the presence of local absolute instability in the axisymmetric mode. For the helical mode of azimuthal wavenumber $m = 1$, under local analysis, two absolutely unstable saddle points are observed. However, these modes are shown to have either small growth rates or small streamwise extent of the absolute instability. This plausibly explains the lack of an unstable discrete global mode for $m = 1$.

3.1 Introduction

Many studies have investigated the dynamics of jets under various scenarios and observed the presence of self-exited oscillations in the case of the heated jets [60, 45], helium jets [83, 29] and also in jets with counter-flow [84]. These

oscillations have been documented in experiments as well as direct numerical simulations (DNS) and the cause of this self-excited behaviour has been attributed to the presence of an absolute instability of the base flow solution. In all these investigations, the importance of buoyancy force resulting from the density difference in the base flow was shown to be insignificant in comparison to the inertia of the fluid [13]. In the absence of either density inhomogeneity or counter-flow, the classical homogeneous jet was shown to be globally stable [25]. Some instability analyses have attempted to investigate the effect of buoyancy on jets by including it as a weak forcing [58]. Overall, it would be fair to say that the regime where buoyancy is either comparable to or dominant over the inertia of the fluid, such as in plumes, has received very little attention in comparison to jets.

The earliest investigations fully accounting for buoyancy were by Wakitani [93], and Riley & Tveitereid [78]. In these studies, local spatial and temporal analyses were performed under the Boussinesq approximation. Both these analyses were limited to the self-similar region of the base flow. Investigations aimed at determining the spatial stability characteristics have not looked at the spatio-temporal behaviour to establish the validity of a spatial investigation in the first place. Under the Boussinesq approximation, a recent study by Chakravarthy et al. [10] focused on the spatio-temporal behaviour of plumes both close to the heat source as well as in the self-similar region far downstream of the source. The existence of an absolute instability for $m = 1$ helical perturbations was established. By switching off buoyancy numerically in the stability analysis, it was demonstrated that the absolute instability is unique to plumes and does not have a non-buoyant counterpart. However, as the investigation was only performed in a local framework, it is still not established whether the absolute instability reported by Chakravarthy et al. [10] would result in a global instability. Lopez & Marques [50] performed unsteady simulations of confined plumes under the Boussinesq approximation and reported a sequence of bifurcations as the Rayleigh number is increased. Through a linear stability analysis of the same base flow, Lesshafft [43] showed that the cause of these bifurcations is likely to be the reflections from the downstream wall rather than the absolute instability of the base flow.

Many experiments have been performed on flows with large density differences, where the Boussinesq approximation is not justified. Subbarao & Cantwell [85] studied the dynamics of helium jets injected into air and observed that beyond a certain Reynolds number and Richardson number, periodic axisymmetric puffing occurs. Similar observations were made by Cetgen & Kasper [9] for a larger range of Richardson numbers. A power

law relating the variation of the puffing frequency, non-dimensionalized as a Strouhal number, was obtained. These experimental findings were corroborated by numerical studies [40, 80]. By gradually changing gravity numerically, Satti & Agrawal [80] have demonstrated that the self-sustained oscillations do not exist in the absence of gravity. However, the mechanism for this stabilization remains to be understood. Nichols et al. [64] performed local spatio-temporal analysis of strongly heated jets injected into cold ambient and showed the existence of an absolute instability which matches with the global frequency obtained from a DNS. Their study, however, was limited only to small Richardson numbers where the effect of buoyancy is not dominant. Also, note that under the Boussinesq approximation, the helical modes were found to be absolutely unstable while in the case of helium jets injected into air, axisymmetric puffing is experimentally observed. This indicates that density difference is an important parameter in the dynamics of the flow and a competition between the modes might be possible. A careful investigation of the parameter space is required to ascertain this possibility.

The current study is aimed towards understanding the reason for the self-sustained oscillations from a hydrodynamic stability point of view both in the *local* and *global* frameworks. As the Richardson number is increased, the base flow transitions from a jet to a plume type flow field. A more interesting issue we seek to understand through this study is the fundamental difference between the dynamics as well as the base state of a plume and those of a jet. In order to account for the large density variation in the base flow, the analysis is performed in the low Mach number limit. The previously investigated Boussinesq limit [10] will be shown to arise as a special case of the more generic low Mach number limit. By varying the Richardson number and density ratio of the fluid injected into the ambient, the dynamics of the flows and the relative effect of various destabilizing mechanisms will be investigated. The base flow under consideration is described qualitatively and the numerically obtained base flow distributions are presented in section 3.2. The governing equations under the low Mach number limit are also given in section 3.2. Section 3.3 formulates the linear stability problem under both global and local frameworks, for arbitrary azimuthal wavenumbers. The results of the global and local stability analyses are presented and discussed in section 3.4 for both axisymmetric and helical modes. A sensitivity analysis of the global eigenvalues is presented in section 3.5. In particular, the role of various destabilizing mechanisms is discussed and also the most sensitive regions with regard to the dynamics of the flow are identified. In section 3.6, the global dynamics considered in the previous sections are related to the local absolute/convective instability of the base flow. Further, a connection

with the previously investigated Boussinesq limit is made. Finally in section 3.7, the main results are summarized and juxtaposed against previous works.

3.2 Problem formulation

3.2.1 Governing equations

A heated calorically perfect fluid is injected into an unstratified quiescent ambient of the same fluid at lower temperature, from a circular orifice in an infinitely large, rigid, adiabatic wall. In order to model a flow which has a strong density variation but low flow velocity, a low Mach number approximation of the fully compressible Navier-Stokes equation is used. One of the first investigations to use this approximation was by McMurtry et al. [54] in the case of non-buoyant jets. It was extended to include buoyancy by Nichols et al. [64], Chandler [11] and the same equations are used in this investigation. In dimensional form, the governing equations are

$$\frac{\partial \tilde{\rho}}{\partial t} + \nabla \cdot (\tilde{\rho}\tilde{\mathbf{u}}) = 0, \tag{3.1a}$$

$$\tilde{\rho}\frac{D\tilde{\mathbf{u}}}{Dt} = -\nabla\tilde{p} + \mu\left[\nabla^2\tilde{\mathbf{u}} + \frac{1}{3}\nabla(\nabla\cdot\tilde{\mathbf{u}})\right] - \mathbf{g}(\tilde{\rho}_\infty - \tilde{\rho}), \tag{3.1b}$$

$$\tilde{\rho}\frac{D\tilde{T}}{Dt} = \alpha\nabla^2\tilde{T}, \tag{3.1c}$$

$$\tilde{\rho}R\tilde{T} = p_0 \tag{3.1d}$$

where $\tilde{\rho}$, $\tilde{\mathbf{u}}$, $\tilde{p}$, $\tilde{T}$ denote the dimensional density, velocity, pressure and temperature respectively, $\tilde{\rho}_\infty$ is the ambient density, $\mathbf{g}$ is the acceleration due to gravity, α is the thermal diffusivity, μ is the dynamic viscosity, and R is the specific gas constant. Note that in (3.1d), p_0 denotes the thermodynamic component of pressure and it is a constant, unlike the hydrodynamic part $\tilde{p}$ in (3.1b). It can be seen that under the low Mach number limit, the continuity equation (3.1a) and momentum equation (3.1b) are the same as the fully compressible conservation equations. However, the energy equation (3.1c) simplifies to a simple advection - diffusion equation for temperature. In order to close this system of conservation equations, the equation of state for a perfect gas (3.1d) is used.

Non-dimensionalizing equations (3.1a) - (3.1d) by adopting the centreline velocity at the inlet $\tilde{u}_j$ as the velocity scale, the difference $\tilde{T}_j - \tilde{T}_\infty$ between the inlet centreline temperature and the ambient temperature as the temperature

scale, radius of the inlet R as the length scale and ambient density $\tilde{\rho}_\infty$ as the density scale, the following equations are obtained:

$$\frac{\partial \rho}{\partial t} + \nabla \cdot (\rho \mathbf{u}) = 0, \tag{3.2a}$$

$$\rho \frac{D\mathbf{u}}{Dt} = -\nabla p + \frac{1}{ReS}\left[\nabla^2 \mathbf{u} + \frac{1}{3}\nabla(\nabla \cdot \mathbf{u})\right] + \frac{Ri}{S-1}(1-\rho)\mathbf{e_z}, \tag{3.2b}$$

$$\rho \frac{DT}{Dt} = \frac{1}{PrReS}\nabla^2 T, \tag{3.2c}$$

$$\rho(1 + T(S-1)) = 1, \tag{3.2d}$$

where, $T = (\tilde{T} - \tilde{T}_\infty)/(\tilde{T}_j - \tilde{T}_\infty)$ is the reduced temperature, Pr is the Prandtl number, $S = \tilde{\rho}_\infty/\tilde{\rho}_j$ denotes the density ratio of the ambient fluid to the fluid injected at the inlet, $Re = \tilde{\rho}_j \tilde{u}_j R/\mu$ is the Reynolds number and $Ri = gR(\tilde{\rho}_\infty - \tilde{\rho}_j)/\tilde{\rho}_j \tilde{u}_j^2$ is the Richardson number. Further, the thermodynamic pressure p_0 is scaled appropriately so as to have the right-hand side of (3.2d) as unity. It can be seen that in the limit $S \to 1$, state equation (3.2d) becomes $\rho \to 1$. Substituting it in equations (3.2a) - (3.2c), the governing equations for the Boussinesq limit given in Chakravarthy et al. [10] are recovered. Although the current investigation is limited to hot fluid injected at the inlet, the analysis can be easily extended to the case of a lighter density fluid injected into heavier density ambient at the same temperature as the governing equations are similar: the Schmidt number takes a role of the Prandtl number and temperature would be replaced by mass fraction of the injected species [14].

3.2.2 Base flow

In a cylindrical coordinate system, where z denotes the axial direction and r denotes the radial direction, the variables can be split into a steady and unsteady component as

$$q = \overline{q}(r, \theta, z) + q'(r, \theta, z, t) \tag{3.3}$$

where $q = (\rho, \mathbf{u}, p, T)^{tr}$, $\overline{q} = (\overline{\rho}, \overline{\mathbf{u}}, \overline{p}, \overline{T})^{tr}$ and $q' = (\rho', \mathbf{u}', p', T')^{tr}$. A steady axisymmetric solution to the set of equations (3.2) is obtained by iteratively solving these equations, using the Newton - Raphson method with finite element method in FreeFEM++ [25] on a domain which is 80 radii along the streamwise direction and 30 radii along the transverse direction. This is equivalent to solving the system (3.2) for a solution of the form $q' = 0$ and

$\overline{q}(r,\theta,z) = \overline{q}(r,z)$. At the inlet $z = 0$, the boundary conditions

$$\overline{u} = 0.5 + 0.5\tanh\left[\frac{R}{4\theta}\left(\frac{1}{r} - r\right)\right] \tag{3.4a}$$

$$\overline{\rho} = 1 - \left(1 - \frac{1}{S}\right)\left(0.5 + 0.5\tanh\left[\frac{R}{4\theta}\left(\frac{1}{r} - r\right)\right]\right) \tag{3.4b}$$

are assumed, where a moderately thin value $R/\theta = 10$ has been chosen throughout the analysis and the radial velocity is set to zero at the station $z = 0$. Such *tanh* profiles to model the flow near an inlet were introduced by Michalke [57] and since then, it has been used to study buoyant jets as well [64]. For the ease of computation, the variable $\overline{T}$ is eliminated from the system of equations (3.2) by using the equation of state (3.2d). Therefore, the boundary conditions on $\overline{T}$ will not be discussed explicitly. Apart from the inhomogeneous Dirichlet type boundary condition for $\overline{\mathbf{u}}$ and $\overline{\rho}$ at the inlet, stress-free boundary conditions are imposed on velocity and pressure on the far field radial and streamwise boundaries. The variable $\overline{\rho}$ is set to unity in far field radial direction while in the streamwise far field, a homogeneous Neumann boundary condition is imposed. On the axis, $r = 0$, a homogeneous Neumann condition is imposed on $\overline{u}_z$, $\overline{p}$ and $\overline{\rho}$ while a homogeneous Dirichlet boundary condition is imposed on $\overline{u}_r$ [41].

The main objective of this study is to understand the effect of buoyancy and therefore the Richardson number Ri is varied from 10^{-4} to 10^3, while the density ratio S is varied between 1.05 and 7. It will be shown later that the effect of Reynolds number Re on the dynamics is very weak. Hence, the investigation is mostly limited to $Re = 200$ and in some cases $Re = 500$. Throughout this analysis, Prandtl number is set to 0.7. Following the procedure described above, a steady axisymmetric base flow is obtained for given Re, Ri and S. Figure 3.1 shows the distribution of axial velocity and density in the $r - z$ plane for extreme values of Ri, $Ri = 10^{-4}$ and 10^3, at $S = 7$ and $Re = 200$. Further in this article, the base flow corresponding to $Ri = 10^{-4}$ will be referred to as the *buoyant jet* while $Ri = 1000$ will be referred to as the *plume*. Figures 3.1(a) and 3.1(b) show the variation of axial velocity and density respectively for the buoyant jet. This base flow is similar to a non-buoyant heated jet [64, 46], where the momentum injected at the inlet dissipates radially as the fluid is convected downstream and consequently the axial velocity along the centreline decreases as z^{-1} for $z \gg 1$. However, for the case of the plume, i.e. $Ri = 1000$, shown in figures 3.1(c) and 3.1(d), the fluid injected at the inlet is continually accelerated due to buoyancy as it is convected downstream and the centreline velocity asymptotes to a non-zero constant as the flow approaches the self-similar

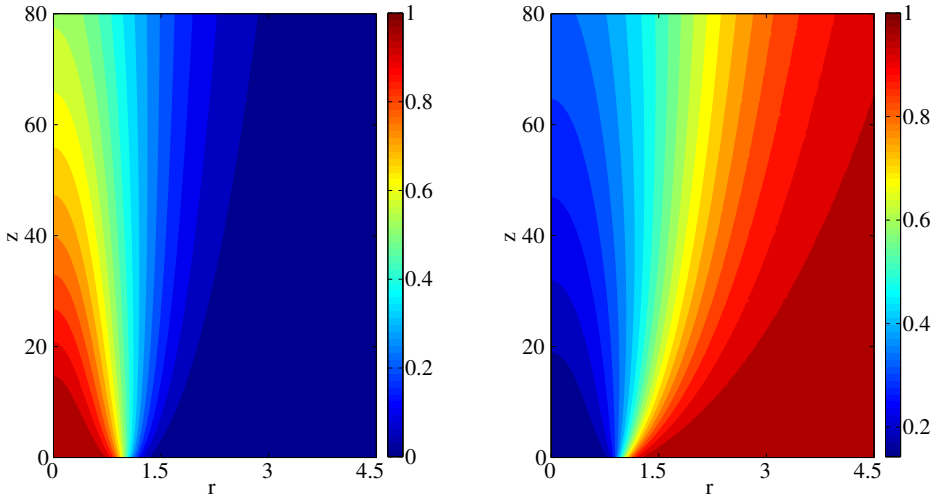

(a) Axial velocity, $\overline{u}_z$

(b) Density, $\overline{\rho}$

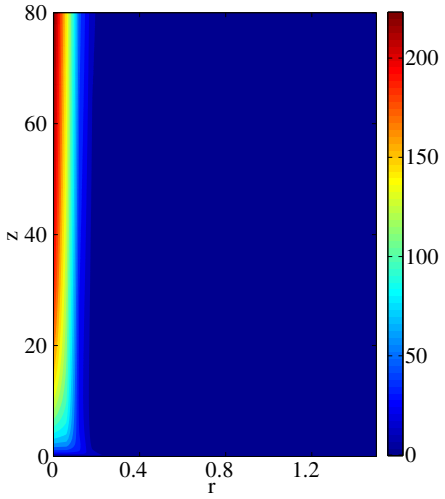

(c) Axial velocity, $\overline{u}_z$

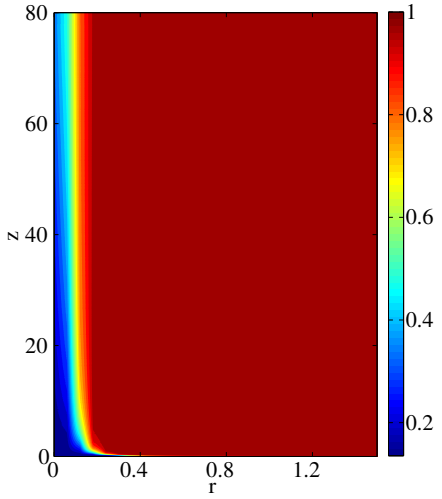

(d) Density, $\overline{\rho}$

Figure 3.1: Distribution of the axial velocity (left) and density (right) in the $r-z$ plane for Richardson numbers $Ri = 0.0001$ (a and b) and $Ri = 1000$ (c and d) at $S = 7$, $Re = 200$.

limit. Although this is not a new result and it was demonstrated analytically in the Boussinesq limit by Yih [98], it is worthwhile to re-iterate the inherent difference between the base flow of a plume and a jet, and demonstrate it through the axial velocity and density distributions for the non-Boussinesq case as well. Another feature of the base flow for the plume is the high entrainment of ambient fluid. In figure 3.1(d), the density contour at $r = 1$ and $z = 0$ is seen to be squeezed towards the axis and within two radii distance from the inlet, the local radius reduces by nearly 80%. While for buoyant jets the variation is gradual, indicating a relatively small entrainment velocity. Although the results are presented only for $S = 7$ and $Re = 200$, qualitatively similar results are observed at other values of Re and S as well.

At low Ri, the flow field is very similar to non-buoyant heated jets indicating a negligible dependence on buoyancy. This is consistent with the definition of Richardson number, which is the ratio of buoyancy to inertia of the fluid injected at the inlet. Large values of Ri indicate the dominance of buoyancy over inertia in the streamwise evolution of the flow and therefore the flow field is very different from a non-buoyant jet. Thus, the flow scenarios *pure jet* and *pure plume* can be interpreted as the asymptotic limits for the value of Ri with *pure jet* corresponding to the limit $Ri \to 0$ and *pure plume* corresponding to the other asymptotic limit $Ri \to \infty$.

3.3 Formulation of the stability problem

3.3.1 Global Stability

As the base flow is highly nonparallel, especially at large Ri near the inlet, the instability dynamics are analyzed in a global framework. In order to accomplish this, a perturbation of the form

$$(\rho', \mathbf{u}', p', T') = \left[\hat{\rho}(r,z), \hat{\mathbf{u}}(r,z), \hat{p}(r,z), \hat{T}(r,z)\right] e^{i(m\theta - \omega t)} + c.c. \qquad (3.5)$$

is superposed on the base flow. Here, the integer m denotes the azimuthal wavenumber and $\omega = \omega_r + i\omega_i$ is the complex frequency. Variables of the form $\hat{q}(r,z)$ are complex-valued functions. Upon linearizing the governing

equations (3.2) with the ansatz (3.5), the following equations are obtained:

$$-i\omega\hat{\rho} + \nabla \cdot (\hat{\rho}\overline{\mathbf{u}} + \overline{\rho}\hat{\mathbf{u}}) = 0, \tag{3.6a}$$

$$-i\omega\overline{\rho}\hat{\mathbf{u}} + \overline{\rho}(\hat{\mathbf{u}}.\nabla\overline{\mathbf{u}} + \overline{\mathbf{u}}.\nabla\hat{\mathbf{u}}) + \hat{\rho}\overline{\mathbf{u}}.\nabla\overline{\mathbf{u}} = -\nabla\hat{p} + \frac{1}{ReS}\left[\nabla^2\hat{\mathbf{u}} + \frac{\nabla(\nabla\cdot\hat{\mathbf{u}})}{3}\right] - \frac{Ri\hat{\rho}}{S-1}\mathbf{e_z}, \tag{3.6b}$$

$$-i\omega\overline{\rho}\hat{T} + \overline{\rho}(\hat{\mathbf{u}}.\nabla\overline{T} + \overline{\mathbf{u}}.\nabla\hat{T}) + \hat{\rho}\overline{\mathbf{u}}.\nabla\overline{u} = \frac{1}{PrReS}\nabla^2\hat{T}, \tag{3.6c}$$

$$\hat{\rho} + \overline{\rho}^2\hat{T}(S-1) = 0, \tag{3.6d}$$

where variables with an overbar ($\overline{q}$) denote the base flow solution. While the base flow is taken to be swirl free, $\overline{u}_\theta = 0$, the azimuthal perturbation velocity u'_θ is not a priori zero. A homogeneous Dirichlet condition is imposed on $\hat{\mathbf{u}}, \hat{\rho}, \hat{T}$ as boundary condition at the inlet $z = 0$, while a homogeneous Neumann condition is imposed on $\hat{p}$. On the axis, depending on the azimuthal mode considered, appropriate boundary conditions as detailed in Khorrami et al. [41] and Chakravarthy et al. [10] are enforced. For the radial and streamwise far field boundaries, a no-stress condition is implemented.

The system (3.6) is cast into the form of an eigenvalue problem

$$\omega B\hat{q} = L\hat{q}, \tag{3.7}$$

where

$$\hat{q} = [\hat{\rho}, \hat{\mathbf{u}}, \hat{p}, \hat{T}]^{tr}.$$

Solving this eigenvalue problem, $\hat{q}(r, z)$ is obtained as the eigenvector with ω as the corresponding eigenvalue. According to the ansatz (3.5), the real part of the eigenvalue, ω_r, denotes the oscillation frequency while the imaginary part, ω_i, denotes the growth rate of the perturbation. As in the base flow computation, the variable $\hat{T}$ is eliminated by using the the linearized equation of state (3.6d). The matrices L and B are constructed through discretization of the operators by using a finite element method in FreeFEM++. The matrices are then exported into MATLAB, where the eigenvalues are obtained by a shift-invert method. This is the same strategy as in several previous investigations [25, 13].

3.3.2 Local Stability

If the base flow is slowly evolving, i.e. weakly nonparallel, the unsteady dynamics can be predicted from local stability analysis. In the local framework,

the perturbation is assumed to be of the form

$$(\rho', \mathbf{u}', p', T') = \left[\hat{\rho}(r), \hat{\mathbf{u}}(r), \hat{p}(r), \hat{T}(r)\right] e^{i(kz+m\theta-\omega t)} + c.c. \tag{3.8}$$

where k is the complex axial wavenumber. Linearizing (3.2) over a parallel base flow with the above ansatz (3.8) for perturbation, equations

$$-i\omega\hat{\rho} + \overline{\rho}\frac{\partial \hat{u}_r}{\partial r} + \overline{\rho}\frac{\hat{u}_r}{r} + \hat{u}_r\frac{\partial \overline{\rho}}{\partial r} + \frac{im\overline{\rho}\hat{u}_\theta}{r} + ik\overline{\rho}\hat{u}_z + ik\overline{u}_z\hat{\rho} = 0, \tag{3.9a}$$

$$-i\omega\overline{\rho}\hat{u}_r + ik\overline{u}_z\overline{\rho}\hat{u}_r = -\frac{\partial \hat{p}}{\partial r} + \frac{1}{ReS}\left[\Delta\hat{u}_r - \frac{\hat{u}_r}{r^2} - \frac{2im\hat{u}_\theta}{r^2} + \frac{1}{3}\frac{\partial(\nabla.\hat{\mathbf{u}})}{\partial r}\right], \tag{3.9b}$$

$$-i\omega\overline{\rho}\hat{u}_\theta + ik\overline{u}_z\overline{\rho}\hat{u}_\theta = -\frac{im\hat{p}}{r} + \frac{1}{ReS}\left[\Delta\hat{u}_\theta - \frac{\hat{u}_\theta}{r^2} + \frac{2im\hat{u}_r}{r^2} + \frac{im}{3r}(\nabla.\hat{\mathbf{u}})\right], \tag{3.9c}$$

$$-i\omega\overline{\rho}\hat{u}_z + \overline{\rho}\frac{\partial \overline{u}_z}{\partial r}\hat{u}_r + ik\overline{u}_z\overline{\rho}\hat{u}_z = -ik\hat{p} + \frac{1}{ReS}\left[\Delta\hat{u}_z + \frac{ik}{3}(\nabla.\hat{\mathbf{u}})\right] - \frac{Ri\hat{\rho}}{S-1}, \tag{3.9d}$$

$$-i\omega\overline{\rho}\hat{T} + \overline{\rho}\frac{\partial \overline{T}}{\partial r}\hat{u}_r + ik\overline{u}_z\overline{\rho}\hat{T} = \frac{1}{PrReS}\Delta\hat{T}, \tag{3.9e}$$

$$\hat{\rho} + \overline{\rho}^2\hat{T}(S-1) = 0, \tag{3.9f}$$

are obtained, where

$$\Delta = \frac{\partial^2}{\partial r^2} + \frac{1}{r}\frac{\partial}{\partial r} - k^2 - \frac{m^2}{r^2},$$
$$\nabla.\hat{\mathbf{u}} = \frac{\partial \hat{u}_r}{\partial r} + \frac{\hat{u}_r}{r} + \frac{im\hat{u}_\theta}{r} + ik\hat{u}_z.$$

The system of equations (3.9) is cast in the form $\omega B\hat{q} = L\hat{q}$, where a complex ω is obtained as an eigenvalue for a prescribed complex k to determine the spatio-temporal characteristics as described in Chakravarthy et al. [10].

3.4 Global spectra and eigenfunctions

The formulations of the local and global stability problem are valid for any azimuthal wavenumber m. As experimental investigations by Subbarao & Cantwell [85] and Cetegen & Kasper [9] have shown the self-sustained oscillations to be axisymmetric in nature, the stability to axisymmetric perturbations is presented first in section 3.4.1 and this is followed by a brief discussion of the helical perturbations of $m = 1$ in section 3.4.2.

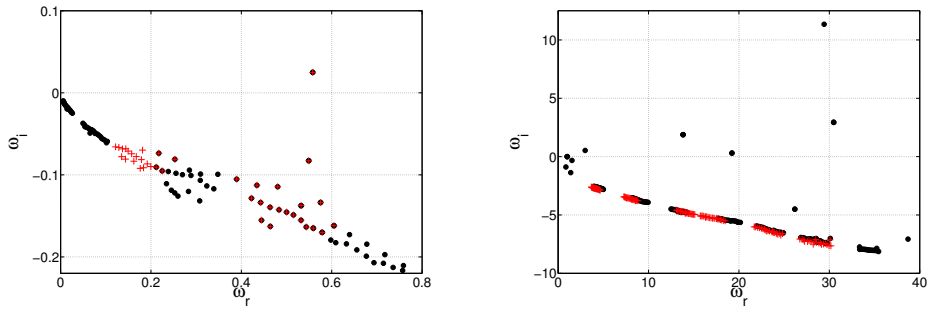

(a) $Ri = 10^{-4}$ (b) $Ri = 10^{3}$

Figure 3.2: Global stability spectrum for the axisymmetric mode $m = 0$, at $Re = 200$, $S = 7$ for the Richardson number indicated in the captions. The solid circles denote the spectrum of equations (3.6) while the spectrum indicated by plus-shaped markers (+) is obtained by setting $Ri = 0$ in equation (3.6b).

3.4.1 Axisymmetric perturbations

As in the discussion of the base flow in section 3.2.2, results will be presented for the two extreme values of Ri for $S = 7$ and $Re = 200$, in order to motivate the discussion on the effect of Ri. Figure 3.2 shows eigenvalue spectra at $Ri = 10^{-4}$ (buoyant jet) and $Ri = 10^{3}$ (plume) for $S = 7$ and $Re = 200$. The solid circles denote the spectrum obtained by solving (3.6) and the plus-shaped makers denote the spectrum of the same set of equations, but with $Ri = 0$. In other words, although the base flow corresponds to a non-zero value of Ri, the Richardson number is set to zero in equation (3.6b). First, consider the spectrum denoted by the circular markers. For the case of a buoyant jet, it can be seen that the spectrum has only one unstable discrete mode and overall, the spectrum resembles that of a non-buoyant jet [13]. As the Richardson number is varied from $Ri = 10^{-4}$ to $Ri = 1000$, the plume limit is approached and the growth rate ω_i as well as the frequency ω_r become much higher than for the buoyant jet. Also, there are multiple discrete modes which are unstable. For the case of buoyant jet, as expected, setting $Ri = 0$ hardly alters the dynamics of the flow, thereby indicating that the dynamics are dominated by inertia forces as in the case of jet. In the plume, however, switching off the buoyancy in the stability equations completely alters the dynamics: all the unstable discrete modes are stabilized. Although the buoyancy is seen to be the cause of unstable eigenmodes in the plume, the same buoyancy simultaneously alters the base state from one that

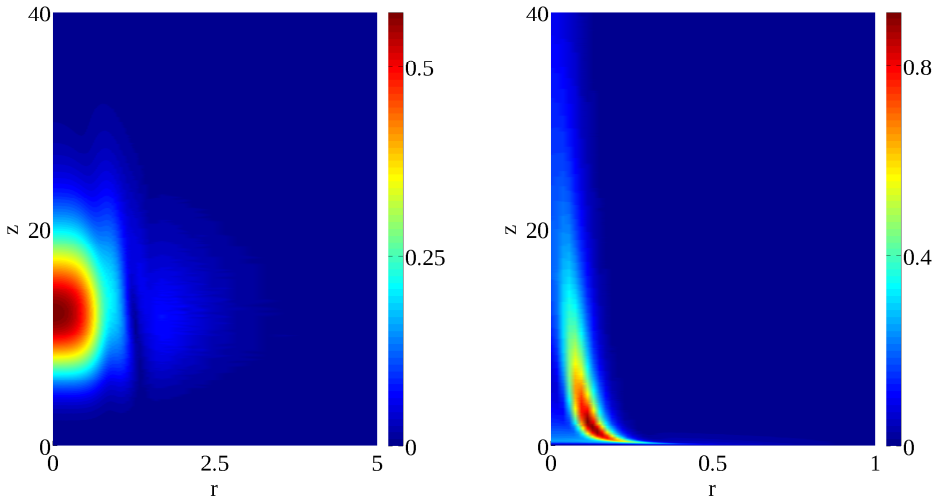

(a) $Ri = 10^{-4}$ (b) $Ri = 10^{3}$

Figure 3.3: Spatial distribution of the absolute value of the axial velocity eigenfunction $\hat{u}_z$ corresponding to the most unstable discrete mode shown in figure 3.2 for the $S = 7$ and $Re = 200$ at the Richardson number Ri indicated below the figure.

is unstable to inertia-driven instability mechanism at $Ri = 10^{-4}$ to a profile stable to such a mechanism at $Ri = 1000$. This will become clearer in section 3.5 where the role of various destabilizing mechanisms are discussed.

The distinct nature of the spectra for buoyant jets and plumes is also reflected in the characteristics of their eigenfunctions. Figure 3.3 shows the spatial distribution of the absolute value of the axial velocity perturbation of the most unstable discrete mode for $Ri = 10^{-4}$ (left) and $Ri = 1000$ (right). At low Ri, the axial velocity eigenfunction has a significant magnitude only beyond 3 radii downstream of the inlet and it has a maximum on the axis around $z = 10$. The radial extent of the eigenfunction is on the order of the plume radius similar to the *jet column mode* of a non-buoyant jet in Lesshafft et al. [45]. In a plume however, see figure 3.3(b), the eigenfunction is significant right from the inlet and has a maximum along the region of maximum density gradient. Also, the radial extent is confined to a thin region of large temperature gradient of the base flow. These very different eigenvalue spectra and the eigenfunction distributions at two extreme Richardson numbers further imply fundamentally distinct instability mechanisms. The reason why the instability in plumes is likely to live in the temperature mixing layer

rather than the shear layer will become clearer when the spectra of parabolic inlet velocity profiles are presented next.

Figure 3.4(a) displays the variations with Ri of the Strouhal number, $St = \omega_r/2\pi$, corresponding to the most unstable discrete eigenvalue for different parameter settings. The thick solid line corresponds to $S = 7$ and $Re = 200$, the solid circular markers to $S = 7$ and $Re = 500$ and the dashed line to $S = 4.5$ and $Re = 200$ with the same inlet conditions as given in equation (3.4). The triangular markers denote a parabolic axial velocity profile at the inlet but a tanh variation in density, as in (3.4), at $S = 7$ and $Re = 200$. In the three cases presented with a tanh inlet velocity profile, two distinct regions in the $St - Ri$ plane are present. At low Ri, there is hardly any variation of St with Ri, i.e. $Ri \propto Ri^0$, and at large Ri, there is strong dependence of St on Ri. For $1 \leq Ri \leq 1000$, the Strouhal number for $S = 4.5$, $Re = 200$ follows the power law $St = 0.29Ri^{0.42}$ and for $S = 7$ and $Re = 200$ it goes as $St = 0.24Ri^{0.43}$. The transition between these two regimes, however, is smooth. These observations corroborate quantitatively with the experimental findings [85, 9]. Cetegen & Kasper [9] performed experiments on pure helium and helium-air injected into quiescent air and drew similar conclusions (figure 5 in Cetegen & Kasper [9]). Their study obtained a single power law $St = 0.26Ri^{0.38}$ for both pure helium and helium - air mixtures for $1 < Ri < 250$. Note that the coefficient for the power law given in Cetegen & Kasper [9] has been rescaled to the current definition of frequency and reference scales. Also, their experiments indicate the presence of two power laws: $St = 0.26Ri^{0.38}$ for $1 \leq Ri \leq 250$ and $St \propto Ri^{0.28}$ for $250 \leq Ri \leq 5000$. However, figure 3.4(a) indicates only a single power law for the entire range $1 \leq Ri \leq 1000$. It can be seen from figure 3.2(b) that at large Ri there are multiple global modes which are unstable. Hence, in an experiment, it is possible that these global modes interact nonlinearly and result in different power laws which cannot be captured by the current linear analysis. The power law holds only for the variation of the most unstable discrete mode. For any other discrete mode, both the exponent and the coefficient of the power law, if it exists, could be different.

In the experimental investigations mentioned before, helium/helium-air mixtures were injected into air through a round pipe and hence, the velocity profile at the exit of the pipe has a parabolic variation. Therefore, a better measure of the success of this model would be to compare the prediction for a parabolic inlet profile with a sharp density gradient and this is given by the triangular markers in figure 3.4. It is seen that at large Ri, the dynamics are independent of the inlet velocity profile and show a behaviour similar to tanh profiles. This hints that at large Ri, the destabilizing mechanism is either

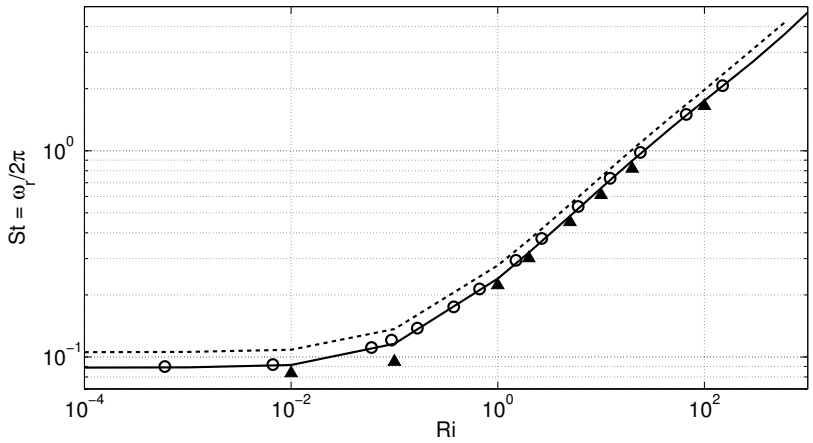

(a)

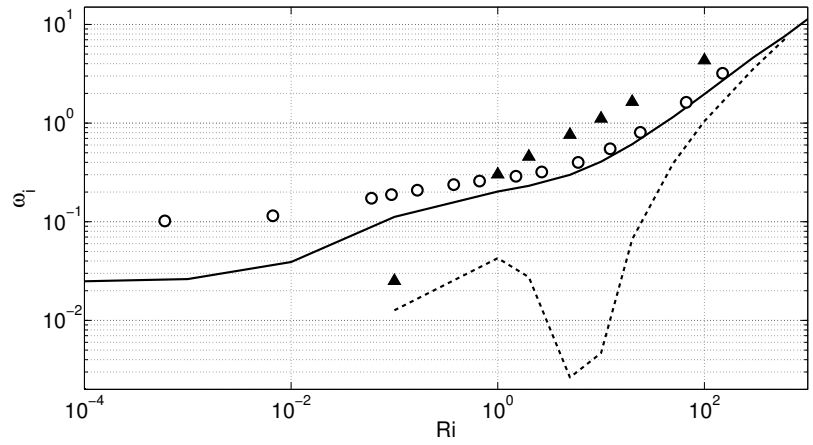

(b)

Figure 3.4: Variation of the complex global frequency ω with Richardson number Ri for the axisymmetric mode: solid line - $Re = 200$, $S = 7$; solid circles - $Re = 500$, $S = 7$, dashed line - $S = 4.5$, $Re = 200$ and triangles - parabolic inlet velocity profile at $Re = 200$, $S = 7$. Figure 3.4(a) gives the variation of Strouhal number, $St = \omega_r/2\pi$, and figure 3.4(b) shows the growth rate ω_i variation.

independent of the shear in the velocity profile or the strong acceleration imparted by buoyancy creates a gradient in velocity profile which is much stronger than that imposed at the inlet. This line of thought will be espoused further in §3.5.2. At low Ri, however, there is a significant difference in the global growth rates of parabolic and the tanh velocity profiles. The parabolic velocity profile is globally unstable only for $Ri \geq 0.1$ while tanh velocity profile results in a global instability for $Ri \geq 0$ (refer to figure 3.4(b)). This is consistent with previous investigations. Lesshafft et al. [46] investigated a tanh variation in velocity and reported self-excited behaviour while DNS by Satti & Agrawal [80] and experiments [9] chose a parabolic variation in velocity and do not observe self-excited behaviour at small Richardson numbers, $Ri \ll 1$. For the parabolic inlet velocity profile, a power law of the form $St = 0.23Ri^{0.43}$ is obtained indicating a good qualitative agreement with the experimental observation $St = 0.26Ri^{0.38}$. The quantitative difference in the numerical values of the exponent and coefficient of the power law is to be expected because, in the current investigation, the density variation is due to heating of the fluid rather than a change in the chemical composition. Thus, the difference in the formulation of Fick's law of species diffusion and Fourier's law of heat conduction is likely to result in quantitative differences [14]. The species and heat diffusion terms have the same form only in the limit of small density variations such as the Boussinesq approximation or the incompressible limit.

Apart from the variation of St with Ri, the effect of S and Re can also be seen from figure 3.4(a). The change in Re from 200 to 500 at $S = 7$ has a negligible effect on the Strouhal number. Although the real part of ω is independent of Re, the imaginary part is seen to increase as Re increases. Figure 3.4(b) shows the variation of ω_i with Ri for the same parameter settings. Similar behaviour can be seen to hold for the variation of S as well. As the density ratio increases, the growth rate increases and the effect of increasing S reduces with increasing Ri. Note that for $S = 4.5$, $Re = 200$ and $Ri < 0.1$, there is no unstable global mode, and this explains why the dashed line starts only from $Ri \geq 0.1$ in figure 3.4(b). Therefore, for these Richardson numbers, the Strouhal number plotted in figure 3.4(a) only denotes the frequency of the least stable discrete mode and not the usual unstable global mode. The same is true for the triangular makers denoting the parabolic profile as well.

The effect of S on the growth rate ω_i can also be seen in figure 3.5 where the neutral curve, i.e. the contour $\omega_i = 0$, at $Re = 200$ is plotted in the $S - Ri$ plane. The thick line represents the neutral boundary for global instability while the thin line denotes the local convective-absolute instability

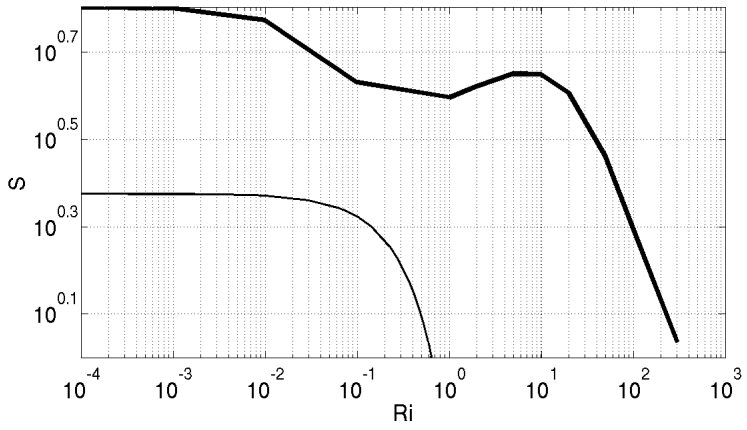

Figure 3.5: Neutral curve in the $S - Ri$ plane for the axisymmetric mode at $Re = 200$. The thick line corresponds to the global stability boundary and the thin line to the local absolute/convective instability boundary based on the inlet profile.

boundary for the inlet profile. The local modes are further discussed in section 3.6. The region enclosed by the curve and the coordinate axes is globally stable while the region outside the neutral curve is globally unstable. It is interesting to note the non-monotonic behaviour of the neutral curve. This is likely to be due to the transition of the eigendynamics from a shear-dominated regime to a buoyancy-dominated regime. As Ri is increased, the effect of the shear decreases and the buoyancy force increases. During this change of destabilization mechanisms, for a small range of Ri, the total destabilizing force decreases and this results in an increase in the minimum value of S required for the global mode to become unstable. This will be further elaborated in section 3.5. The analysis is limited to $S > 1$ only, and therefore the neutral curves plotted in figure 3.5 cannot be extrapolated to $S \leq 1$.

3.4.2 Helical perturbations

So far, the dynamics of the flow to axisymmetric perturbations were discussed. The global instability characteristics are in good agreement with the nonlinear behaviour observed in experiments. However, all the experiments were in a regime where the density ratio S is far from unity. It was shown in Chakravarthy et al. [10] that in the Boussinesq limit $S \to 1$, the helical $m = 1$ mode is absolutely unstable while the axisymmetric $m = 0$ mode is at

most convectively unstable. Hence, it is necessary to investigate the global dynamics of $m = 1$ and verify if the absolute instability translates to a global instability and if so, what the characteristics of this instability are.

As in the discussion of $m = 0$ modes in section 3.4.1, the global mode spectra are determined for $Ri = 0.01$ and $Ri = 10$ at $S = 7$ and $Re = 200$ as shown figure 3.6. For the case of $Ri = 0.01$, the base flow is very similar to a non-buoyant jet, and the global eigenspectrum is also similar: no unstable global mode is observed at $m = 1$. In figure 3.6(a) two branches of continuous modes are present. On one branch, as ω_r increases, ω_i monotonically decreases; this is referred to here as the *continuous branch*. The second branch, resembling a parabola, has a non-monotonic variation of ω_i with ω_r and this will be referred to as the *arc branch* for further discussion. On increasing the Richardson number from $Ri = 0.01$ to $Ri = 10$, the continuous branch remains stable while the arc branch becomes unstable as shown in figure 3.6(b).

Such an arc branch of eigenmodes, referred to as *box modes* in Coenen et al. [13], has been observed for the case of jets, wakes [52] and boundary layers [1, 24]. These modes were seen to be stable for the case of jets [25, 13] while for the case of boundary layers, depending on the downstream boundary condition, they could be either stable or unstable [1, 24]. An important feature of these box modes is that, as one starts from the low frequency end of the arc branch and goes further along the branch, the number of zero crossings of the real part of the eigenfunction increases monotonically. This has been demonstrated in the case of jets for $m = 0$ by Coenen et al. [13]. Similar behaviour has also been observed for the eigenfunctions of both buoyant jets and plumes for $m = 1$. In figure 3.7, the contours of $log_{10}|\hat{u}_{z,real}|$ for two consecutive points on the arc branch are shown for $Ri = 0.01$ and $Ri = 10$. Here, rather arbitrarily, the second and third points along the arc branch are chosen for demonstration. The plots on the left correspond to the second point and the ones on the right to the third point while the top row is for $Ri = 0.01$ and the bottom row is for $Ri = 10$. It is seen that an additional cycle or *wavelength* is added to the eigenfunction of the third mode in comparison to the second mode for both $Ri = 0.01$ and $Ri = 10$. This suggests that the arc branch is a numerical artifact due to the numerical condition imposed at the downstream boundary.

The dependence of the arc branch on the length of the numerical box is documented in figure 3.8 for yet another parameter setting. Over the considered range, increasing the box length results in a slight destabilization of the arc branch modes in the higher frequency range. The sensitivity of the

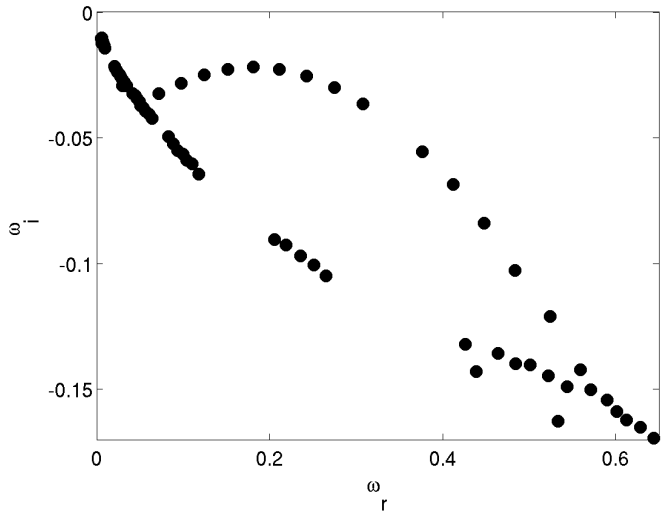

(a) $Ri = 0.01$

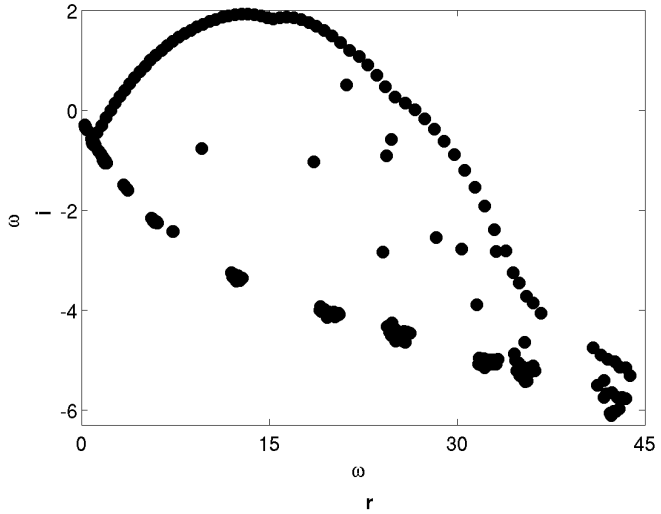

(b) $Ri = 10$

Figure 3.6: Global stability spectrum for the helical mode $m = 1$, at $Re = 200$, $S = 7$ for $Ri = 0.01$ (top) and $Ri = 10$ (bottom).

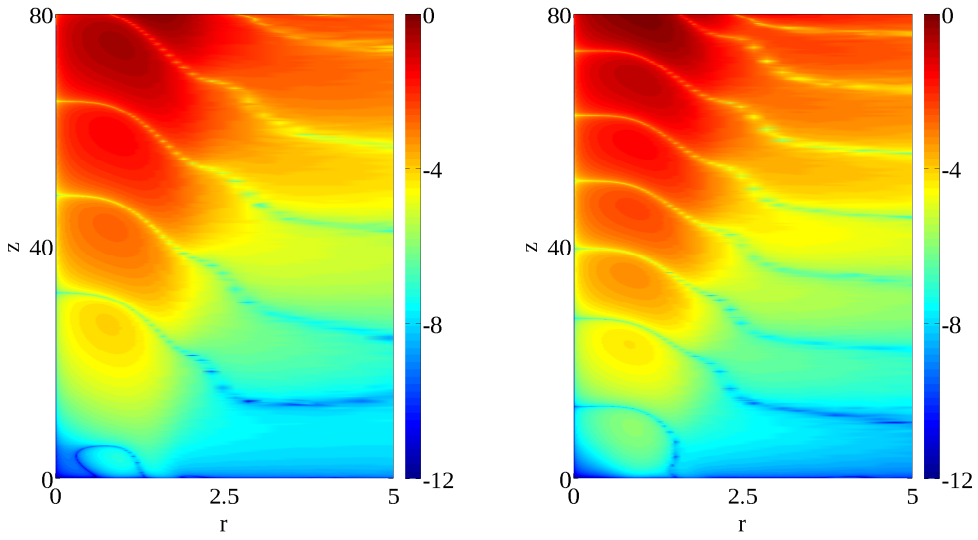

(a) $Ri = 0.01$ (b) $Ri = 0.01$

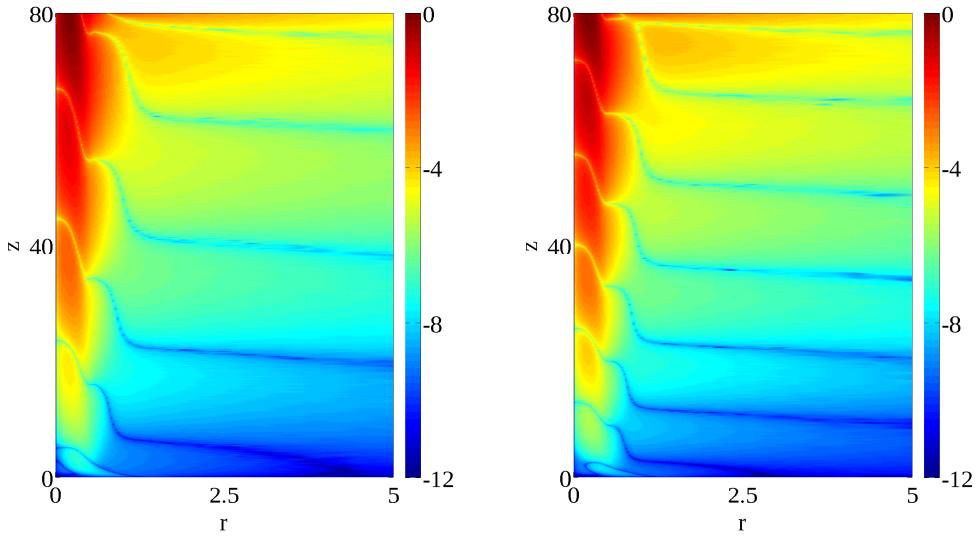

(c) $Ri = 10$ (d) $Ri = 10$

Figure 3.7: Distribution of the magnitude of the real part of the axial velocity eigenfunction int $r - z$ plane for 2 consecutive modes on the continuous parabolic-shaped branch for the helical mode $m = 1$ at $S = 7$ and $Re = 200$ at $Ri = 0.01$ and 10. The data are shown on a log scale, i.e. as contours of $log_{10}|\hat{u}_{z,real}|$.

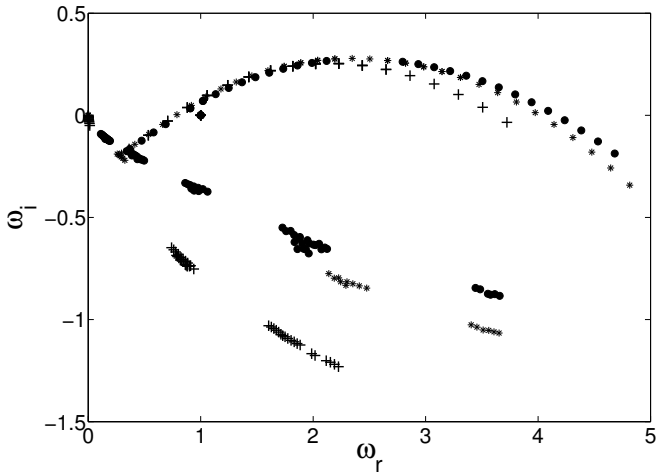

Figure 3.8: Global spectrum for the $m = 1$ mode at $Ri = 1$, $S = 7$ and $Re = 200$ for various domains sizes, i.e. locations of the streamwise far field boundary L_z: 50 (+), 80 (*) and 100 (solid circles) radii. For all cases, the radial far field boundary L_r is set to 30 radii from the axis.

branch to box length seems to be rather weak in this setting. An important observation in this context is that laminar self-similar plumes are convectively unstable even infinitely far away from the inlet. Therefore, adding further downstream extent to the box is unlikely to decrease the perturbation amplitude at the outflow which might decrease the gain of the spurious feedback. This is to be contrasted against the axisymmetric mode in jets [13], where the arc branch stabilizes with increasing downstream extent of the box possibly because the flow is locally stable far downstream and thereby decreasing the gain of spurious feedback.

The physically relevant conclusion that can be drawn from this analysis of the $m = 1$ mode is that no unstable discrete mode is obtained for the range of S and Ri investigated in this study. Thus, the absolutely unstable $m = 1$ local mode reported in Chakravarthy et al. [10] does not seem to trigger global instability. Also, the arc branch is inherent to any base flow that is convectively unstable close to downstream boundary. A better numerical treatment might make it stable, but it would still exist.

3.5 Interplay of shear and buoyancy

In section 3.4.1 it has been demonstrated that there is a clear difference between the dynamics in the buoyant jet limit and in the plume limit. In this section, a discussion on the cause of this difference is presented with specific emphasis on identifying the underlying mechanisms in the various regimes. As mentioned in section 3.4.2, the $m = 1$ perturbations have no discrete unstable global mode and the arc branch is most likely a numerical phenomenon resulting from the presence of a numerical boundary and therefore, would not warrant any discussion from the physical point of view. Hence, this section will focus only on the axisymmetric modes.

3.5.1 Endogeneity Formulation

A new sensitivity measure for understanding the intrinsic dynamics of the flow called *endogeneity* was proposed recently by Marquet & Lesshafft [51]. A brief note on this sensitivity measure is presented for the benefit of the unfamiliar reader. The classical structural sensitivity analysis formulated by Giannetti & Luchini [27] maps the sensitivity of the eigenvalues in various regions of the flow, i.e. the maximum change in the magnitude of an eigenvalue that can be triggered by the modification of the operator L at a given point in the flow field. Here, the matrix L is the same as the one described in section 3.3.1 corresponding to the global stability equations (3.6). The main disadvantage of the structural sensitivity is that one cannot distinguish if the change in the magnitude of eigenvalue is due to the frequency ω_r or the growth rate ω_i. By contrast, the endogeneity distinguishes the effect of various terms in the operator L, on the real and imaginary parts of the complex frequency ω. The spatial locations which are most relevant to the dynamics may thus be identified, as well as the way that individual terms in the equations contribute to the global eigendynamics.

The expression for the endogeneity $E(r, z)$ is

$$E(r, z) = \hat{q}^\dagger(r, z) \cdot [L\hat{q}(r, z)], \tag{3.11}$$

with $\hat{q}^\dagger$ denoting the adjoint eigenfunction obtained by solving the adjoint eigenvalue problem of the form

$$L^H \hat{q}^\dagger = \omega^* B^H \hat{q}^\dagger. \tag{3.12}$$

Here, the superscripts *, ^{H} denote the complex conjugate and Hermitian transpose respectively, and the dot in equation (3.11) only denotes the dot

product of the vector $\hat{q}^\dagger$ with $L\hat{q}$ at a given (r, z) and not a spatial integration which would result in $E(r, z)$ being constant throughout the flow field.

Performing an integration of $E(r, z)$ over the entire domain gives

$$\int_\Omega E(r,z)d\Omega = \langle \hat{q}^\dagger, L\hat{q} \rangle = \omega. \tag{3.13}$$

Note that in deriving the expressions (3.11), and (3.13), the eigenvector $q^\dagger$ is assumed to be normalized such that $\langle \hat{q}^\dagger, B\hat{q} \rangle = 1$. By splitting L into various terms such as

$$L = L_{shear} + L_{buoyancy} + L_{viscous} + L_{rest}, \tag{3.14}$$

the contribution of the individual terms to the eigenvalue can be obtained. Also, as these integrals are complex valued, the contribution of various terms to the real and imaginary parts of the eigenvalue can be quantified separately. A detailed derivation of the expressions (3.11) and (3.13) is given in Marquet & Lesshafft [51]. Note that the endogeneity is only a linear sensitivity measure. Therefore, the contribution to the eigenvalue obtained from equations (3.13) and (3.14) should be treated as the contributions in the infinitesimal limit. Stated differently, this contribution is not to be confused with the resulting change in the eigenvalue if that particular term in the operator L was switched off numerically and the eigenvalue is re-computed.

This sensitivity analysis based on endogeneity is now extended to buoyant jets and plumes to understand the role of various terms in the dynamics. In order to do so, the governing equation (3.6b) is recast in the following form that is easy to relate to the previously investigated Boussinesq limit and interpret the physical meaning of the terms:

$$-i\omega\hat{\mathbf{u}} + \overline{\mathbf{u}}.\nabla\hat{\mathbf{u}} = \mathcal{S} + \mathcal{P} + \mathcal{B} + \mathcal{V} \tag{3.15}$$

where

$$\mathcal{S} = -\hat{\mathbf{u}}.\nabla\overline{\mathbf{u}}, \tag{3.16a}$$

$$\mathcal{P} = -\frac{\nabla\hat{p}}{\overline{\rho}} + \frac{\hat{\rho}\nabla\overline{p}}{\overline{\rho}^2}, \tag{3.16b}$$

$$\mathcal{B} = \frac{Ri}{S-1}\frac{-\hat{\rho}}{\overline{\rho}^2}\mathbf{e_z}, \tag{3.16c}$$

$$\mathcal{V} = \frac{1}{ReS}\left[\frac{1}{\overline{\rho}}\left(\nabla^2\hat{\mathbf{u}} + \frac{\nabla(\nabla\cdot\hat{\mathbf{u}})}{3}\right) - \frac{\hat{\rho}}{\overline{\rho}^2}\left(\nabla^2\overline{\mathbf{u}} + \frac{\nabla(\nabla\cdot\overline{\mathbf{u}})}{3}\right)\right]. \tag{3.16d}$$

This form of velocity perturbation equation is obtained by dividing equation (3.6) by $\overline{\rho}$ and substituting the following expression for $\overline{\mathbf{u}}.\nabla\overline{\mathbf{u}}$ which is obtained from the base flow momentum equation

$$\overline{\rho}\ \overline{\mathbf{u}}.\nabla\overline{\mathbf{u}} = -\nabla\overline{p} + \frac{1}{ReS}\left[\nabla^2\overline{\mathbf{u}} + \frac{\nabla(\nabla\cdot\overline{\mathbf{u}})}{3}\right] + \frac{Ri}{S-1}(1-\overline{\rho})\mathbf{e_z}. \tag{3.17}$$

In equation (3.15), the effect of shear is given by $\mathcal{S}$, buoyancy by $\mathcal{B}$ and viscosity by $\mathcal{V}$. Regarding the interpretation of the pressure term $\mathcal{P}$, the first term $-\nabla\hat{p}/\overline{\rho}$ is related to the baroclinic torque through the curl operator while the second term $\hat{\rho}\nabla\overline{p}/\overline{\rho}^2$ denotes the strongly nonparallel nature of the base flow. Under the boundary layer approximation, in the absence of any external pressure gradient, this term vanishes as $\nabla\overline{p}$ is identically zero.

Given this interpretation of the various terms in the perturbation velocity equation (3.15), the operator L can now be split into a form analogous to equation (3.14) where

$$L_{buoyancy} = \mathcal{B}, \tag{3.18a}$$
$$L_{viscous} = \mathcal{V}, \tag{3.18b}$$
$$L_{pressure} = \mathcal{P}, \tag{3.18c}$$
$$L_{shear} = \mathcal{S}, \tag{3.18d}$$
$$L_{rest} = L - L_{shear} - L_{pressure} - L_{buoyancy} - L_{viscous}. \tag{3.18e}$$

Note that the matrix L here corresponds to the same set of equations (3.6) except for the momentum perturbation equation (3.6b) which is replaced by the velocity perturbation equation (3.15). Therefore, L_{rest} contains the contributions of continuity, temperature and state equations alongside the convection term $\overline{\mathbf{u}}.\nabla\hat{\mathbf{u}}$ of (3.15). Substituting equations (3.18) and (3.14) in equation (3.13), the eigenvalue can be split as

$$\omega = \langle q^\dagger, L_{shear}q\rangle + \langle q^\dagger, L_{pressure}q\rangle + \langle q^\dagger, L_{buoyancy}q\rangle + \langle q^\dagger, L_{viscous}q\rangle + \langle q^\dagger, L_{rest}q\rangle, \tag{3.19}$$
$$\omega = \omega_{shear} + \omega_{pressure} + \omega_{buoyancy} + \omega_{viscous} + \omega_{rest} \tag{3.20}$$

and the contributions of various terms in the governing equations may be analyzed.

3.5.2 Results and discussion

Based on the above formalism, the role of various terms in the dynamics of buoyant jets and plumes are analyzed. Figures 3.9(a) and 3.9(b) show

the contributions to the growth rate while 3.9(c) and 3.9(d) represent the contributions to the frequency at various Ri for $S = 7$ and $Re = 200$. For the ease of interpretation, the variations of growth rate and frequency are split into two plots each: low Ri, $10^{-4} \leq Ri \leq 10$, corresponding to buoyant jets are presented on the left and large Ri, $10 \leq Ri \leq 10^3$, corresponding to plumes are shown on the right. First, consider the variation of growth rates with Ri. At low Ri, figure 3.9(a), the growth rate of ω_{shear} is much larger than any other term on the right-hand side of equation (3.20) and therefore, shear is likely to be the dominant destabilizing term. On the other hand, at large Ri, figure 3.9(b), the contribution of buoyancy is larger than the contribution of shear towards ω_i, indicating that the role of buoyancy is dominant in determining the dynamics of plumes. This hypothesis is consistent with the eigenspectra shown in figure 3.2 where at low Ri, absence of buoyancy does not alter the spectrum while at large Ri, the absence of buoyancy stabilizes the flow globally.

The above observation regarding the relative importance of shear and buoyancy coupled with the spatial distributions of eigenfunctions shown in figure 3.3, give an insight into the different nature of destabilization at work in each of these regimes. For buoyant jets, the dynamics are similar to non-buoyant hot jets where the instability was shown by Lesshafft & Huerre [44] in a local framework to be a jet column type mode, i.e. the dynamics scale with the radius of the jet and are caused by the base flow shear. This is supported by the spatial distribution of the global eigenfunction given in figure 3.3(a) which has a radial extent of the order of inlet radius and confined within the shear region of the base flow. In plumes, the eigenfunction lives in a thin region close to the temperature mixing layer of the base flow. This can be reasoned from the dominance of $\mathcal{B}$ in the dynamics of the flow. The expression for $\mathcal{B}$, given by equation (3.16c), can be re-written as $\mathcal{B} = Ri\hat{T}$ by using the linearized state equation (3.6d). Thus, it can be seen that the only flow variable in $\mathcal{B}$ is the temperature perturbation $\hat{T}$ and even a small change in the base flow would result in a large variation in temperature if the perturbation is concentrated around the region of maximum gradient in the base flow temperature. Restating it differently, the instability in buoyant jets may be interpreted as the result of the base flow shear region which is of the same scale as the radius R, while in plumes the instability can be seen as result of the gradient in temperature which is confined to much smaller length which is of the order θ.

During this transition of the dominant destabilizing mechanism, over a small range of Ri, neither the shear nor the buoyancy force are strong enough to destabilize that flow globally. As a result, the minimum value of the

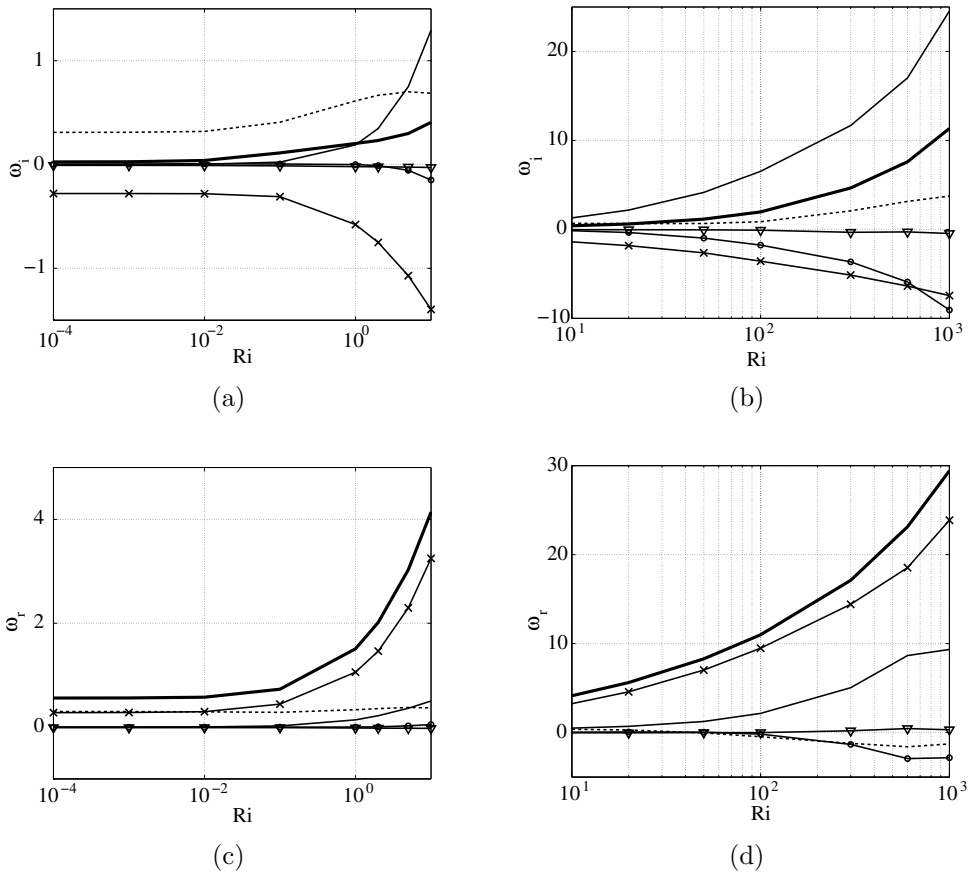

Figure 3.9: Contribution of various terms in the operator L to the eigenvalue ω as a function of Ri at $S = 7$ and $Re = 200$: thick solid line - ω; dashed line - ω_{shear}; thin solid line - $\omega_{buoyancy}$; triangles - $\omega_{viscosity}$; circles - $\omega_{pressure}$ and ($\times$) - ω_{rest}. Figures (a, b) show the contributions to ω_i and (c, d) to ω_r.

density ratio S required to destabilize the flow increases. This explains the non-monotonic behaviour of the neutral curve shown by the thick line in figure 3.5. Although the contribution of $\mathcal{B}$ towards ω is negligible for buoyant jets, the contribution of $\mathcal{S}$ is not negligible for plumes. However, this does not mean that the inlet velocity profile needs to have a strong gradient to trigger an instability. It is shown in figure 3.4 that even for a parabolic inlet profile, at large Ri the growth rate and frequency are close to that obtained with a tanh inlet velocity profile. This could be interpreted as follows: at large Ri, the gradient of the temperature profile is quickly imposed on the velocity profile as the fluid is strongly accelerated because of buoyancy. Thus, the velocity profile imparted at the inlet soon becomes irrelevant downstream and even a parabolic velocity profile which has a smooth variation at the inlet, transforms into a velocity profile with a strong gradient. Such a transition in the shear production from one that is determined by the inlet profile to one that is buoyancy induced can also be seen in the variation of $\omega_{i,shear}$ with Ri from figures 3.9(a) and 3.9(b). Until $Ri \leq 5$, $\omega_{i,shear}$ increases monotonically with Ri. However, $\omega_{i,shear}$ decreases slightly as Ri is increased for $5 \leq Ri \leq 20$ and for $Ri > 20$, it again increases monotonically. This non-monotonic behaviour could be due to the switch in the shear from being inlet determined to becoming buoyancy induced.

Even though the baroclinic torque is contained in $\mathcal{P}$, its contribution to the dynamics cannot be accounted for from the current formulation as it is based on forces and not torques. In fact, the endogeneity of $-\nabla\hat{p}/\overline{\rho}$, whose curl corresponds to baroclinic torque, can be shown to be zero. An analysis based on velocity-vorticity formulation is underway to ascertain the role of the baroclinic torque in the global dynamics of buoyant jets. Although the endogeneity of the term resulting in the baroclinic torque is zero, the total contribution of pressure, $\omega_{pressure}$, is non-zero. The component of pressure resulting from the nonparallel nature of the base flow is seen to have a strongly stabilizing influence on the global eigendynamics at large Ri. In the analysis of non-buoyant jets, this term is usually omitted because the flow is weakly nonparallel and therefore, the base flow is mostly modeled under the boundary layer approximation where $\nabla\overline{p} = 0$. This is consistent with the results from endogeneity calculations. At low Ri, where the base flow is very similar to that of a pure jet, both the real and imaginary parts of $\omega_{pressure}$ are small. However, at large Ri, where the base flow is strongly nonparallel (see figure 3.1), the contribution is substantial, and therefore should not be neglected for analyzing plumes or any flow field which is strongly nonparallel. Shifting the attention to figures 3.9(c) and 3.9(d) which detail the contributions to the global frequency ω_r, it is observed that most of the contribution

comes from L_{rest} (thin dashed line) which includes convection. The rest of the terms of the operator, $\mathcal{S}, \mathcal{B}, \mathcal{V}$ and $\mathcal{P}$, have a relatively smaller influence on the global frequency ω_r.

Until now, only the integral measure of endogeneity as defined by equations (3.13) and (3.20) is studied. For the case of the cylinder wake, Marquet & Lesshafft [51] showed the spatial distributions of $E(r, z)$ and mapped out the stabilizing and destabilizing region of the flow. A similar analysis for buoyant jets and plumes is shown in figure 3.10 where the real and imaginary parts of the endogeneity are plotted for $S = 7$, $Re = 200$ at two different Ri. The imaginary part given in figures 3.10(a) and 3.10(b) are discussed first. It can be seen from figure 3.10(a) that the most endogenous region for buoyant jets lies along the shear layer around $r = 1$, slightly downstream of the inlet and for the plume at $Ri = 100$, it lies very close to the inlet along the region of base flow temperature mixing layer. This mapping is consistent with shear being dominant instability mechanism in the case of buoyant jets while in the case of plumes, it is buoyancy. However, an oscillating pattern of the sensitivity means that the flow is stabilized by the operator at a certain location, while in the immediate neighborhood it becomes destabilizing. For a highly nonparallel base flow, such as the plume at $Ri = 100$, it might not be too counter-intuitive. However, for a buoyant jet at $Ri = 10^{-4}$, where the base flow is only weakly nonparallel, such patterns are indeed surprising. Similar oscillating patterns were reported by Tammisola [87] for the sensitivity of a wake instability with respect to base flow variations. The real part of endogeneity shown in figures 3.10(c) and 3.10(d) looks qualitatively similar to the imaginary part except that they differ in phase from the imaginary part, roughly by $\pi/2$. However, not much progress could be made with regard to interpreting the spatial distributions of the endogeneity of these global modes.

3.6 Local analysis

An approach to establish whether the global dynamics are intrinsic to the flow or due to some forcing at the boundaries (pressure feedback) is to perform a local analysis of the flow field and see if it is absolutely unstable anywhere in the domain as the existence of local absolute instability is a necessary criterion for global instability [12]. Moreover, the nonlinear global mode frequency, if it exists, can be predicted from the local spatio-temporal behaviour [72, 18]. In this study, a local analysis is undertaken primarily to show the intrinsic nature of the observed linear global modes. Also, as the

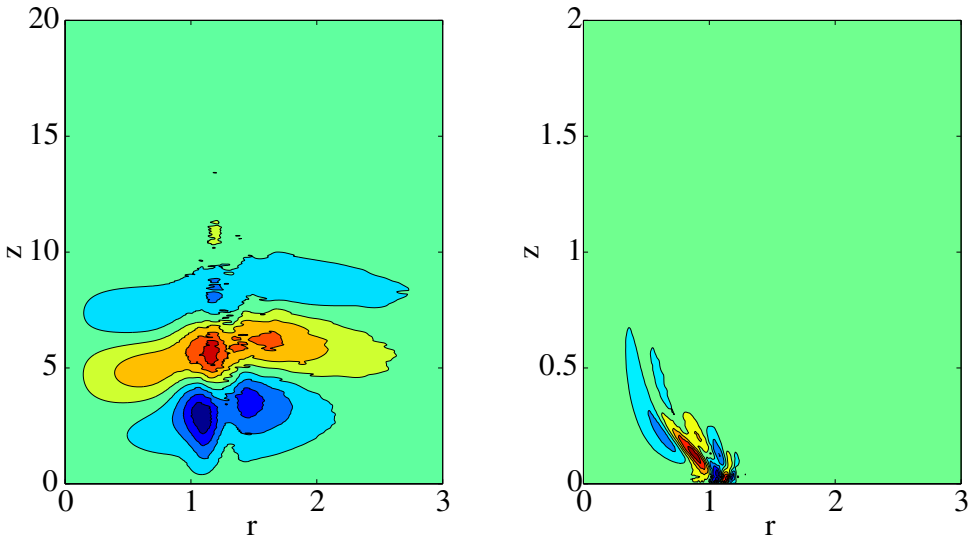

(a) $Ri = 0.0001$ (b) $Ri = 100$

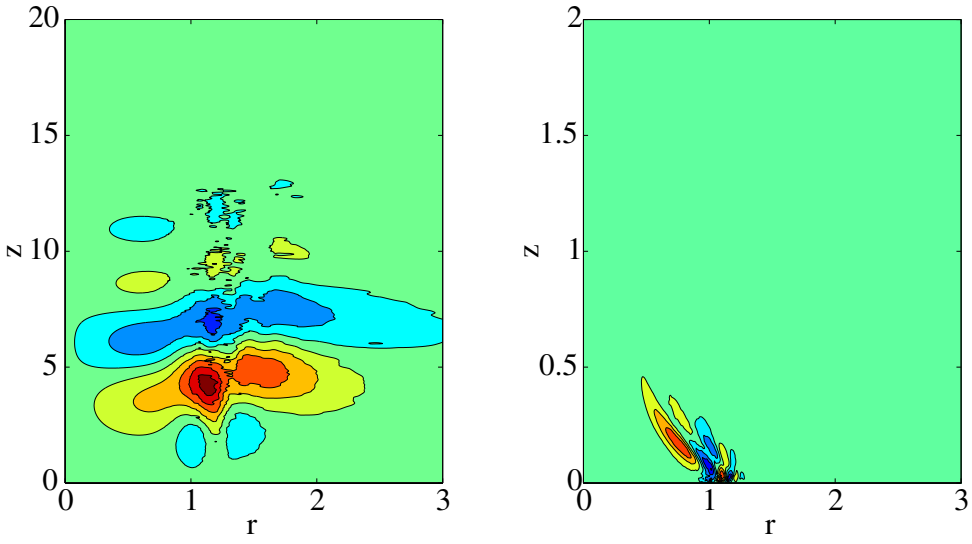

(c) $Ri = 0.0001$ (d) $Ri = 100$

Figure 3.10: Spatial distribution of the real (bottom row) and imaginary (top row) parts of the endogeneity $E(r, z)$ corresponding to the most unstable discrete mode for $S = 7$ and $Re = 200$ at $Ri = 0.0001$ (left) and 100 (right).

experimental investigations confirm the existence of axisymmetric puffing in the case of helium jets, it may be interesting to see if the nonlinear selection criterion for a semi-infinite domain holds good for the current situation.

The existence of absolute instability for buoyant jets and plumes is accomplished by tracking the saddle point of the dispersion relation (3.9) in the complex k-plane. To perform this search in the complex k-plane, for any given complex k, a complex ω is obtained as the eigenvalue for the system of equations (3.9a) – (3.9f). The associated group velocity v_g is obtained as [47]

$$v_g = \hat{q}^\dagger \frac{\partial L}{\partial k} \hat{q}. \tag{3.21}$$

A saddle point of the dispersion relation is defined by $v_g = 0$. The wavenumber $k_0 = k_{0,r} + ik_{0,i}$ corresponding to this saddle point is solved for iteratively by using the secant method until the convergence criterion $|v_g| < 10^{-6}$ is satisfied. The complex frequency $\omega_0 = \omega_{0,r} + i\omega_{0,i}$ corresponding to $k_0 = k_{0,r} + ik_{0,i}$ is obtained as the eigenvalue of the dispersion relation. Note that, in this section, the matrix L refers to the local dispersion relation given by equations (3.9a) - (3.9f). The local spatio-temporal results for the axisymmetric mode $m = 0$ and the helical mode $m = 1$ are discussed in section 3.6.1 and section 3.6.2 respectively.

3.6.1 Axisymmetric perturbations

In this section, the spatio-temporal stability of axisymmetric modes is analyzed under the local stability formulation presented in section 3.3.2. Figure 3.11 shows the variations of ω_0 and k_0 with streamwise location for $Ri = 10^{-4}$ and $Ri = 100$ at $S = 7$ and $Re = 200$. It is seen that for both these values of Ri, the flow is absolutely unstable, starting from the inlet until 7 radii downstream. For the buoyant jet case at $Ri = 10^{-4}$, the base flow is weakly nonparallel and the selection criterion for a semi-infinite domain determines that the global nonlinear frequency would correspond to the absolute frequency at the inlet. From figure 3.11, the real part of ω_0 at $z = 0$ for $Ri = 10^{-4}$ is $\omega_{0,r} = 0.54$ and this matches closely with the global stability prediction of $\omega_r = 0.56$ given in figure 3.4(a). The same comparison fails at $Ri = 100$: $\omega_{0,r}(z = 0) = 1.33$ while $\omega_r = 10.99$. This huge departure from the local absolutely unstable mode is expected because the base flow is highly nonparallel and the selection criterion does not hold. The nonparallel nature of the base state can also be seen from the variation of $\omega_{0,r}$ with z: it varies nearly by two decades within a distance of 10 radii from the inlet.

Another interesting observation to be made is that the streamwise extent of the sensitive region of the flow as per the spatial distribution of endogeneity (see figure 3.10) is also within this domain of absolute instability.

In order to establish the existence of absolute instability over the entire globally unstable regime, the neutral curve for absolute stability is plotted in the $S - Ri$ in figure 3.5 (thin line). It is observed that the convective to absolute instability boundary is much below the global instability boundary for $m = 0$. To compute this convective to absolute instability boundary, only the velocity and density profiles at the inlet are considered. Therefore, for some combination of S and Ri, it is possible to obtain $\omega_{0,i}(z) > 0$ for some $z > 0$ while $\omega_{0,i}(z = 0) \leq 0$. Although the contour $\omega_{0,i} = 0$ would be different in such a scenario, it can not be outside the boundary obtained at $z = 0$. However, the current analysis already shows that the region of global instability is within the absolutely unstable region.

3.6.2 Helical perturbations

In this subsection, the local dynamics with respect to the $m = 1$ helical perturbations are presented. It was shown in figure 18 of Chakravarthy et al. [10] that, in the Boussinesq limit, there are two saddle points in the complex k-plane and one of them is absolutely unstable while the other is convectively unstable. In the present discussion, this absolutely unstable saddle point will be referred as *mode 1* and the saddle point which is convectively unstable in the Boussinesq limit as *mode 2*.

Figure 3.12 displays the variations of $\omega_{0,i}$ with density ratio S, for mode 1 and mode 2 at $Re = 100$, $Ri = 1$. The solid lines representing the variation with S for the inlet velocity and density profiles given in equation 3.4 are discussed first. As S is increased, there is not much change in the growth rate of mode 1 (no markers) but the growth rate of mode 2 (solid circles) increases with S. However, it never becomes absolutely unstable. For the specific setting of $S = 7$, $Ri = 1$ and $Re = 200$, the streamwise evolutions of mode 1 and mode 2 are tracked, and the results are presented in figure 3.13. It is seen that the mode 2, which is convectively unstable at the inlet, remains convectively unstable throughout the domain and the growth rate of mode 1 asymptotes towards zero. This asymptotic behaviour is similar to the variation of ω_0 and k_0 in the Boussinesq limit [10]. For mode 1, as $\omega_0, k_0 \to 0$ with increasing z, the variation could be tracked only till $z \approx 5$. Despite the presence of absolute instability, the global analysis of the $m = 1$ mode reveals that no discrete unstable global mode exists for the range of

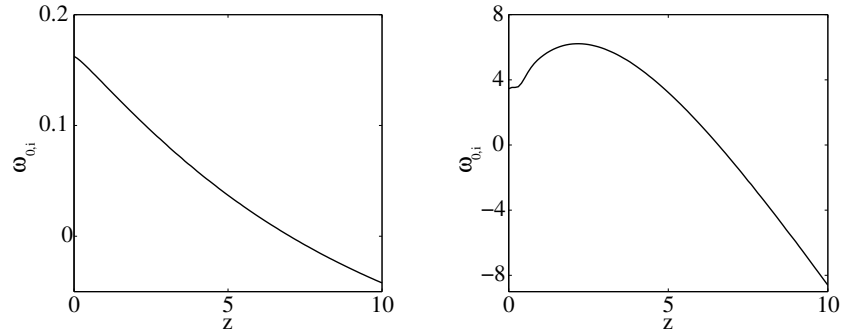

(a) $Ri = 0.0001$

(b) $Ri = 100$

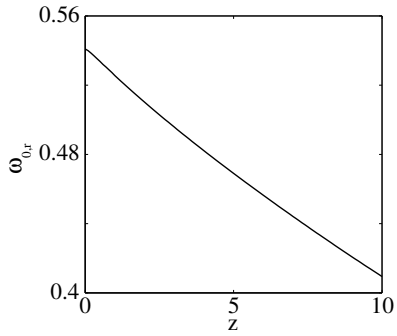

(c) $Ri = 0.0001$

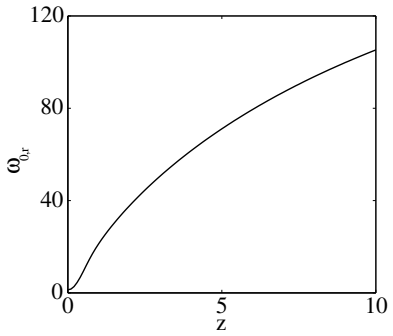

(d) $Ri = 100$

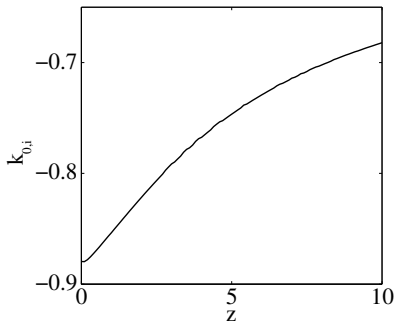

(e) $Ri = 0.0001$

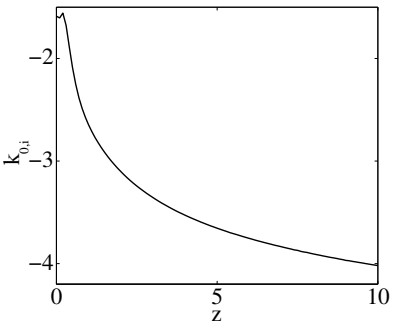

(f) $Ri = 100$

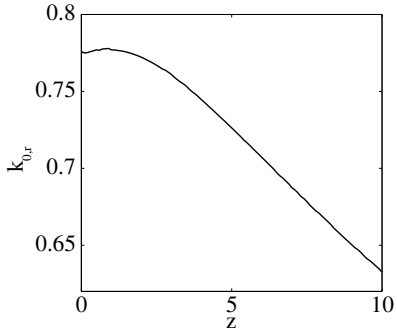

(g) $Ri = 0.0001$

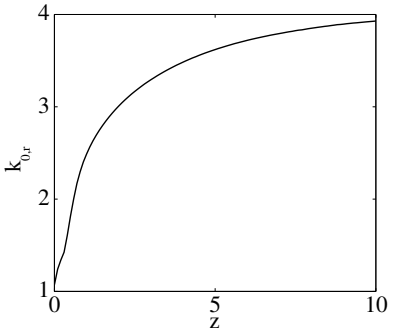

(h) $Ri = 100$

Figure 3.11: Variation of the absolute wavenumber k_0 and absolute frequency ω_0 of the axisymmetric mode $m = 0$ with streamwise location z for Richardson numbers 10^{-4} (left) and 100 (right) at $S = 7$, $Re = 200$.

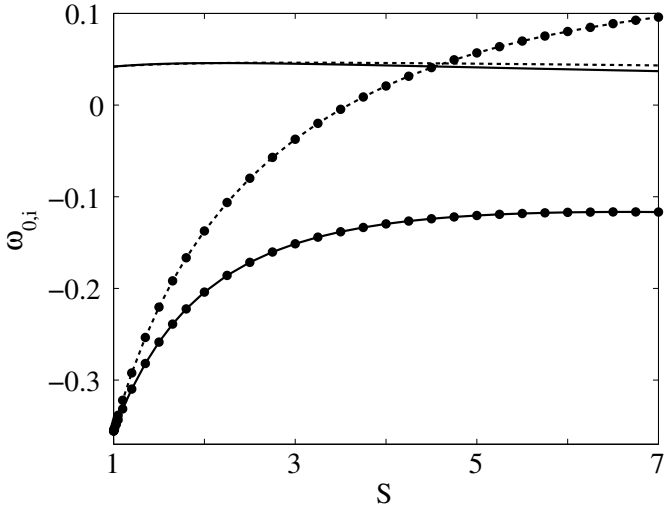

Figure 3.12: Absolute growth rate $\omega_{0,i}$ as a function of density ratio S at $Re = 100$ and $Ri = 1$ for $m = 1$ at the inlet: circles - mode 2 and no marker - mode 1. The solid lines correspond to a *tanh* variation in $\overline{\rho}$ and dashed lines denote *tanh* variation for $\overline{T}$ at the inlet.

parameters investigated. A plausible explanation for this result could be that the local absolute growth rate of mode 1 is too small to trigger a global instability, while mode 2 is always convectively unstable. Moreover, the growth rate of the weakly unstable mode 1 drops by a decade within 2 radii from the inlet, thus reducing the effective region of absolute instability of the mode. It was demonstrated in the case of the Ginzburg-Landau equation by Chomaz et al. [12] that for a flow to exhibit a global instability, the absolute growth rate must be sufficiently strong and the streamwise extent of this absolute instability should be large enough.

Note that absolute instability of mode 1 is unlikely to be related to the unstable arc branch because the ω_r value of the arc branch is orders of magnitude different from the $\omega_{0,r}$ value of mode 1. With regard to mode 2, though it was shown to be convectively stable for $Ri = 1$, for larger Ri it becomes absolutely unstable at the inlet. Figure 3.14 gives the variation of the absolute growth rate of mode 2 with Ri at $S = 7$ and $Re = 200$. The absolute growth rate is observed to monotonically increase with Ri and become absolutely unstable for $Ri \geq 3$. However, as in the streamwise evolution of mode 2 at $Ri = 1$, the absolute growth rate quickly drops and the flow becomes convectively unstable within 0.5 radius from the inlet, as shown in figure 3.15 for $S = 7$, $Re = 200$ and $Ri = 100$. This is to be contrasted with the

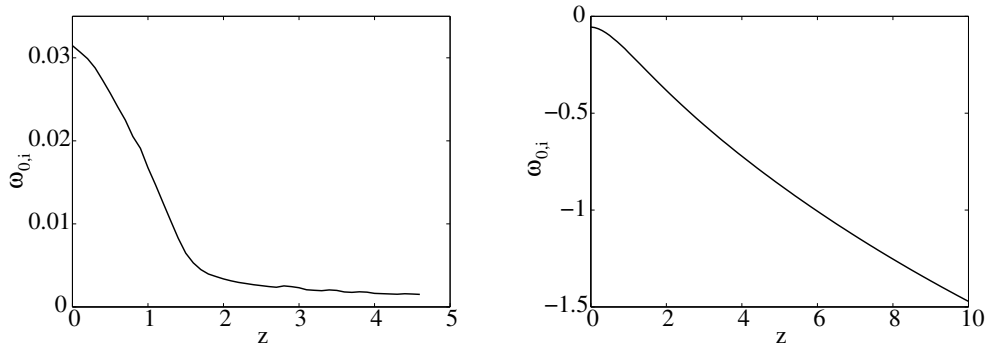

(a) mode 1 (b) mode 2

Figure 3.13: Streamwise variation of absolute growth rate $\omega_{0,i}$ of helical mode $m = 1$ at $S = 7$, $Re = 200$ and $Ri = 1$ for mode 1 (left) and mode 2 (right).

absolutely unstable mode for $m = 0$ (see figure 3.11(b)), where the region of absolute instability extends until 7 radii downstream of the inlet for the same inlet conditions. Therefore, though mode 2 is absolutely unstable for some parameters, the region of absolute instability is too small to trigger a global instability. This possibly explains the lack of any discrete global mode for $m = 1$ over the entire range of parameters investigated.

As the absolute instability starts right at the inlet for $m = 0$ as well as for $m = 1$, the inlet conditions are likely to greatly influence the dynamics. This can be demonstrated by changing the density profile at the inlet in equation (3.4) to

$$\overline{\rho} = \frac{1}{1 + (S-1)\left(0.5 + 0.5\tanh\left[\frac{R}{4\theta}\left(\frac{1}{r} - r\right)\right]\right)}. \tag{3.22}$$

This amounts to choosing a tanh variation for the temperature $\overline{T}$ instead of density $\overline{\rho}$. This results in a 1/tanh dependence for the density. As for the density profile 3.4, two saddle points are observed and their absolute growth rate variation with S is shown as dashed lines in figure 3.12. Mode 2 is seen to become unstable at $S = 3.5$. This is an example to illustrate the strong dependence of the dynamics on base flow. Thus, the results presented in this study are very sensitive to the choice of velocity and density profiles at the inlet.

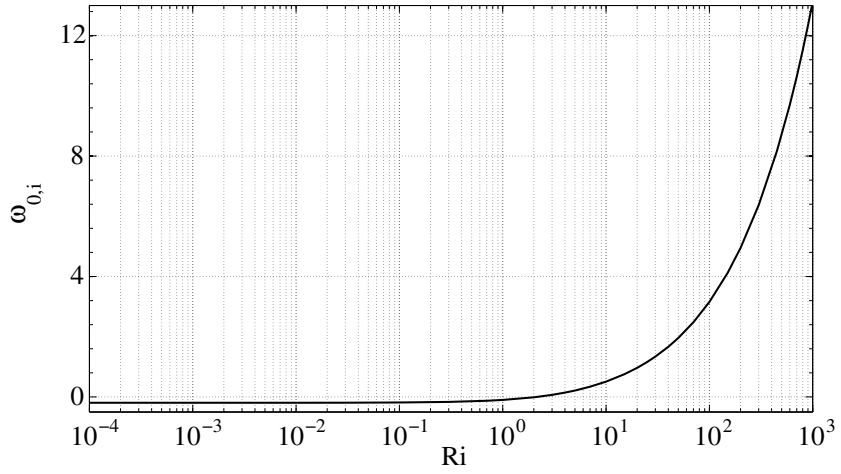

Figure 3.14: Absolute growth rate $\omega_{0,i}$ as a function of Richardson number Ri at $Re = 100$ and $S = 7$ for mode 2.

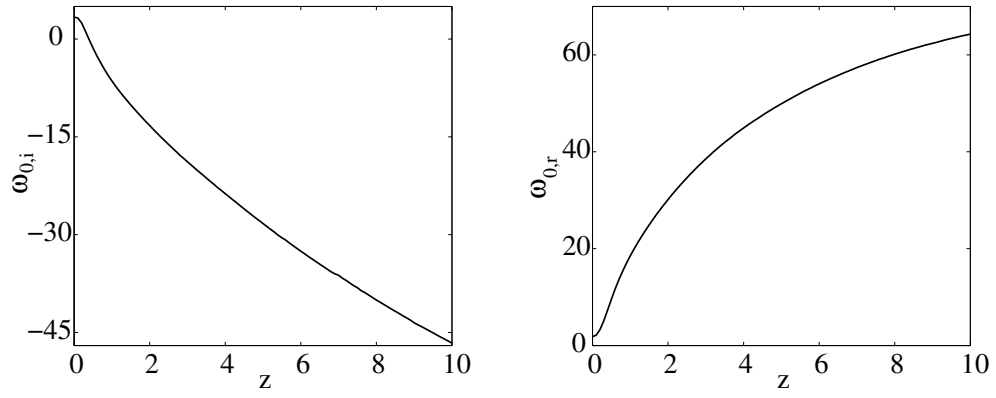

(a) $\omega_{0,i}$ (b) $\omega_{0,r}$

Figure 3.15: Variation of absolute frequency ω_0 for mode 2 with streamwise location z at $S = 7$, $Re = 200$ and $Ri = 100$.

3.7 Conclusions

The global and local stability of buoyant jets and plumes injected into quiescent ambient with imposed initial velocity and temperature variation at the inlet has been investigated. The global dynamics have been documented for a wide range of Richardson numbers and density ratios under the low Mach number approximation in a fully nonparallel formulation. For the investigated range of parameters, it was observed that only the axisymmetric perturbations could exhibit an unstable discrete global mode. This is consistent with the experimental findings of Subbarao & Cantwell [85] and Cetegen & Kasper [9] who report axisymmetric puffing in plumes. Moreover, the puffing frequency predicted by the current global analysis closely matches their experimental results. The dynamics of helical perturbations were also analyzed and no unstable discrete global mode could be found. Instead a continuous branch of unstable modes was obtained. However, this continuous arc branch is very likely to be present due to the numerical downstream boundary and it therefore does not have any physical relevance. This is supported by the lack of any local absolute instability with comparable frequency.

With regard to the global axisymmetric mode, its physical nature was discussed based on its endogeneity. Through an integral measure of endogeneity, the contributions of various terms in the perturbation velocity equation to the global eigenvalue were computed and thus, most dominant terms which destabilize the flow were determined. It was demonstrated that two destabilizing forces exist: shear and the buoyancy. At low Richardson numbers, the contribution of shear is the dominant, while at large Richardson numbers, buoyancy dominates. This is supported by the global eigenspectra computed with and without buoyancy. Further, the contribution of various terms to the global instability coupled with the spatial distributions of the endogenity and eigenfunctions, led to identify the plausible mechanisms through which buoyant jets and plumes are destabilized. In the case of buoyant jets, the destabilization is due to the shear region and is likely to scale with R; while in plumes, it is driven by the large gradient in the base flow temperature and it is likely to scale with the steepness of temperature profile θ. Investigations are underway in order to verify this hypothesis, and also to understand the role of baroclinic torque by solving the stability equations in vorticity-velocity formulation. Besides, it would be interesting to see the effect of the nonparallel component of pressure in the vorticity formulation. Overall, although a good grasp of the integral measure of endogeneity was obtained, much remains to be understood with respect to the spatial distribution of this new sensitivity measure.

To confirm that the observed global dynamics are indeed intrinsic to the flow and not an artifact of the boundary conditions, a local stability analysis of the flow was performed. The presence of global instability for $m = 0$ is supported by the presence of local absolute instability within the base flow. It was shown that the region of global instability was contained within the region of local absolute instability in the $S - Ri$ plane. Moreover, the global nonlinear frequency predicted by the local analysis matches well with the global linear frequency at low Richardson number, where the flow is weakly nonparallel. For $m = 1$, two saddle points were identified in the complex k-plane, as in the previous Boussinesq analysis [10], where one saddle point (mode 1) was absolutely unstable while the other (mode 2) is convectively unstable. At small Richardson numbers, mode 2 is convectively unstable everywhere in the physical domain while mode 1 is absolutely unstable throughout the physical domain. However, the absolute growth rate of mode 1 is very small. For large Richardson numbers, the flow is absolutely unstable with respect to helical perturbations via mode 2 as well and the absolute growth rate is comparable to the axisymmetric mode. Even so, the absolute growth was shown to quickly become negative within half a radius from the inlet. Therefore, both $m = 1$ saddle points are incapable of triggering a global instability: the absolute growth rate is either too small or too limited in streamwise extent. This interpretation is consistent with the absence of any discrete unstable global mode for $m = 1$.

This analysis as well as the previous investigation in the Boussinesq limit [10] were done in a linear framework. Hence, the nonlinear dynamics cannot be captured. This is possibly the reason why the predictions differ with the experiments on helium jets at high Richardson numbers. The linear analysis predicts the existence of multiple unstable global modes but does not say much about the possible interaction between them. Moreover, in the range of parameters where the flow is absolutely unstable and globally stable (linearly), it is possible to have a nonlinear global mode [16]. Another possibility is a bifurcation to a new steady, possibly asymmetric, base flow as a result of the linear instabilities. This was demonstrated by Lopez & Marques [50] through a DNS in the case of confined plumes under the Boussinesq approximation. Also, it was illustrated in the present work that a small change in the inlet density profile from tanh to 1/tanh greatly alters the absolute stability characteristics. Thus, caution must be exercised when extending the results to a flow with different inlet profiles. Subbarao & Cantwell [85] point out that helium jets and diffusion flames are two extreme examples of plume profiles, based on the way buoyancy is released: in a diffusion flame, it is concentrated in a thin annular region at the inlet while in helium jets, it

is uniformly distributed across the inlet. The present study only investigated the helium jet limit. Furthermore, the current investigation was limited to a Prandtl number of 0.7 where the kinematic viscosity and thermal diffusivity are of the same order. For Prandtl numbers much different from unity, the dynamics could be different qualitatively as demonstrated by Lakkaraju & Alam [42] for planar plumes.

Acknowledgements

We would like to thank Wilfried Coenen for assisting us with the FreeFEM++ code to compute the adjoint eigenvalue problem.

Chapter 4

Concluding remarks

4.1 Summary

The primary objective of this dissertation was to contrast the dynamics of buoyant jets and plumes. This was accomplished by varying the Richardson number in the case of flows driven from a finite-size inlet, and the Grashof number in the case of point-source driven flows over a wide range of values. The predictions of the linear global stability analyses compared well, both qualitatively and quantitatively, with the experiments and direct numerical simulations. The intrinsic nature of these linear global modes was supported by the presence of local absolute instability. Additionally, through computation of the perturbation kinetic energy in a local temporal analysis and the endogeneity in the global stability analysis, the role of shear and buoyancy towards destabilizing these flows was quantified: shear was shown to be the dominant destabilizing mechanism for buoyant jets while buoyancy drives the instability in plumes.

Based on the assumptions on density variation, the above stability analyses can be divided into two categories: 1. Boussinesq approximation - the density variation is neglected everywhere expect in the buoyancy term in the momentum equation and a linearized equation of state is invoked; and 2. low Mach number approximation - a more general framework than Boussinesq approximation where density variation due to the temperature is considered via perfect gas law, but the variation due to the hydrodynamics, i.e. velocity and pressure variations, is neglected. Both these approximations are more general than the incompressible limit where any density variation is strictly forbidden.

Boussinesq approximation

The bulk of the stability analysis under this approximation was performed under a local framework on a self-similar velocity profile. For most of the domain in the streamwise wavenumber (k) - Grashof number (Gr) plane, the helical mode corresponding to an azimuthal wavenumber m of unity was seen to be the most unstable temporal mode. Through a budget of the perturbation kinetic energy, the region of buoyancy and shear dominance in the $k - Gr$ plane was mapped out: buoyancy dominates for low k and small Gr while shear dominates for large Gr. Furthermore, beyond a critical Grashof number of the order of unity, the $m = 1$ mode was found to transition to an absolute instability. This was obtained by computing the saddle point of the dispersion relation in the complex $k-$plane as well as a DNS of the linear impulse response. The absolutely unstable saddle point exists only in the presence of buoyancy and does not have a non-buoyant counterpart. The axisymmetric mode ($m = 0$) and the double-helical mode ($m = 2$) are also temporally unstable, but only in small pockets in the $k-Gr$ plane which are mostly enclosed within the region where $m = 1$ is also unstable. Moreover, the growth rates of these $m = 0$ and $m = 2$ modes are much smaller than the $m = 1$ helical mode, and they are at most convectively unstable. Therefore, these modes might be irrelevant to the long-time global dynamics of the flow.

Note that all the above predictions are based on self-similar flow profiles which are attained far downstream of the inlet. Hence, the pertinence of the predictions was examined for a specific case close to the inlet. It was observed that only the $m = 1$ mode is absolutely unstable throughout the domain while the axisymmetric mode never becomes absolutely unstable but, the temporal growth rates of $m = 1$ and $m = 0$ are of the same order. Until now, only the local stability properties were discussed under this Boussinesq approximation. Preliminary investigation of the global dynamics of the Boussinesq plume suggests that the absolute instability of $m = 1$ mode does not translate into a linear global instability possibly owing to its small growth rate [12]. This is in agreement with the global stability computations under the low Mach number approximation for density ratios close to unity, where helical perturbations are seen to remain stable. However, the absence of a linear global instability does not forbid the existence of nonlinear global instability and such an analysis remains to be performed [72].

Low Mach number approximation

Although the Boussinesq plume does not seem to have any unstable linear

global mode, experiments on low speed helium jets injected into quiescent air exhibit spontaneous axisymmetric puffing beyond certain a Richardson number Ri and Reynolds number Re. In order to analyze such a configuration with large density variations in the base flow, the governing equations were obtained under the low Mach number approximation. Within this setting, linear global stability analysis is undertaken for the most part over a wide range of Richardson numbers $10^{-4} \leq Ri \leq 10^{3}$ and density ratios $1.05 \leq S \leq 7$. The oscillation frequencies obtained via linear global stability computations match well with the previously performed experiments [85, 9]. Furthermore, the presence of absolute instability in the flow was established. This strongly suggests that the unstable linear global modes are intrinsic to the flow and therefore, are related to the self-sustained axisymmetric oscillations observed in the experiments. Also, for the weakly nonparallel buoyant jets, the real part of the absolute frequency predicts the nonlinear global frequency of the DNS study [64] in accordance with the nonlinear selection criterion obtained in the 1D Ginzburg-Landau equation [17, 18].

After establishing the intrinsic nature of the linear global modes, the cause of this instability was explored next through computing the endogeneity of various terms in the governing equations. At low Richardson numbers, the instability is shear-driven while for plumes, i.e. high Richardson numbers, it is buoyancy-driven. This relative importance of shear and buoyancy for buoyant jets and plumes respectively, together with the spatial distributions of their respective eigenfunctions, provide an insight into the plausible instability mechanism. In buoyant jets, the instability mechanism is the same as that of a jet column mode in non-buoyant hot jets and it scales with the inlet radius. On the contrary, in the case of plumes, the instability is driven by the buoyancy and the dynamics are likely to scale with the thickness of the temperature gradient.

The global eigendynamics of helical perturbations was also investigated and no discrete unstable modes were observed for the entire range of Ri and S considered in this study. However, local spatio-temporal analysis reveals that, depending on the Richardson number, either *mode 1* or both *mode 1* and *mode 2* are absolutely unstable. These modes either have small absolute growth rates or the absolute instability is limited to a very small region in the streamwise direction. This is consistent with the absence of any unstable discrete global helical mode [12].

4.2 Future work

The current analysis focused on quiescent ambient and this is seldom the case in real flows, say exhaust from a chimney. Recall the picture of smoke rising from a cigarette by van Dyke [92] shown in figure 1.2. In a quiescent ambient, under the Boussinesq approximation, linear global stability analysis indicates that the flow is likely to remain stable. However, large scale self-excited oscillations are observed in figure 1.2. In order to explain the oscillations, it might be essential to consider cross-wind because these large scale structures are inclined at an angle to gravity. This makes a study on the effect of cross-wind very interesting and pertinent to real flows.

An important limitation of the current investigation is that all the predictions are made under a linear framework. Although the helical perturbations do not display any linear global mode, it is still possible that there might be a nonlinear global mode as the flow is absolutely unstable with respect to helical perturbations. Moreover, a steady absolute mode is known to lead to a symmetry-breaking bifurcation in the wake past a sphere [69] and past a disk [55]. In the case of confined plumes, Lopez & Marques [50] have demonstrated that the flow undergoes a series of bifurcations as the Rayleigh number is increased, eventually leading to an asymmetric base flow. Even in the case of axisymmetric perturbations, at large Richardson numbers, there is a departure of the linear global predictions from the experimental results. Two plausible explanations for the departure are: 1. the global oscillations could be the result of an absolute instability over a new steady base state resulting from a bifurcation of the base state currently investigated; and 2. due to the interaction of unstable linear global modes of the base state considered in this study. Thus, a possibly rich physics of the nonlinear regime remains to be explored.

In the current flow configuration itself there are many unanswered questions. For instance, the oscillatory pattern of the endogeneity is largely unexplained in physical terms. Furthermore, it was demonstrated that the dynamics are very sensitive to inlet conditions. For the current tanh type inlet temperature profiles, the effect of steepness at the inlet on the dynamics remains to be explored. Besides, if the profile was changed from a tanh type to one that mimics the heat release in a diffusion flame, the results could be very different. The buoyancy released from a diffusion flame is very compact in radial extent. This is in contrast to a helium jet, which has buoyancy distributed uniformly across the inlet. Buoyancy release in the current analysis is close to that of a helium jet. In geophysical contexts, such as magma flows,

saline conduits or carbon dioxide saturated flows, the Prandtl numbers and Schmidt numbers are very different from unity. For large Prandtl numbers, a new unstable mode was shown to exist in the case of planar plumes [42]. Therefore, for Prandtl numbers and Schmidt numbers much different from unity, the current predictions might not hold. Also, ambient stratification and Coriolis force might also be very important in oceanic contexts.

The current analysis therefore needs to be seen as a first step towards studying the plethora of buoyancy-driven flows. In particular, it explored the effect of buoyancy in shear flows, both in the base flow and the eigendynamics by considering a fundamental case of the free plume in quiescent, unstratified ambient.

Appendix

Effect of buoyancy on the instability of light jets and plumes

R. V. K. Chakravarthy, L. Lesshafft and P. Huerre,
Laboratoire d'Hydrodynamique (LadHyX), CNRS – École Polytechnique,
91128 Palaiseau, France

presented at
The International Conference on Jets, Wakes and Seperated Flows
16 - 18 June 2015, KTH, Stockholm, Sweden.

(accepted for publication in the proceedings)

Abstract

The linear global stability of light jets and plumes is analyzed to examine the role of buoyancy on the dynamics of the flow by varying the Froude number under low Mach number approximation. In this study, buoyancy is generated due to the heating of fluid injected at the inlet (thermal plume). The results also closely describe the dynamics of an isothermal light jet at the corresponding density ratio, ρ_∞/ρ_j, where ρ_j and ρ_∞ are the jet and ambient density respectively. The analysis is limited to a thermal plume which has a density ratio $\rho_\infty/\rho_j = 7$ corresponding to the value for pure Helium injected into air. At large Froude number (or small Richardson number), the dynamics of the flow are shown to be determined by the baroclinic torque resulting in the Kelvin Helmholtz instability as in the case of hot jets. However, as the Froude number is lowered, the dominant growth rate and Strouhal number increase monotonically and the dynamics become strongly buoyancy dependent. The variation of Strouhal number with Richardson number (or Froude number) resulting from the global instability is found to match closely with the experimental and DNS investigations on Helium jets injected into air.

A.1 Introduction

Many investigations have previously addressed, from the stability point of view [11, 36, 44, 46], the local and global dynamics of light jets, and confirmed the existence of self-sustained oscillations due to baroclinic torque. However, the same cannot be said about their buoyant counterparts, plumes and light jets. This study aims to extend the global stability analysis to strongly buoyant light jets, plumes and explore the variation of the dynamics with Froude number.

Firstly, due to the addition of buoyancy, the base flow of a plume differs from that of a jet. The fundamental difference is that a jet emerges from a nozzle with a given amount of streamwise momentum which diffuses as the fluid convects downstream whereas, in the presence of buoyancy, plumes continue to generate vertical momentum at any given streamwise station.

With regard to unsteady dynamics, the presence of buoyancy generates a torque which could destabilize the flow, in addition to the baroclinic torque and vortex stretching/tilting which result in the classical K-H instability. One of the earliest experiments on strongly buoyant light jets were made by Subbarao and Cantwell [85]. It was observed that Helium jets injected into air, in a certain range of parameters, exhibit self-excited axisymmetric puffing. Similar observations were made by Cetegen and Kasper [9] for pure Helium and Helium - air mixtures over a larger range of parameters and a power law describing the variation of Strouhal number with Richardson number was obtained. More recent studies [11, 40, 64, 75, 80] performed a DNS of light jets and their results corroborate the experimental findings. These numerical experiments have demonstrated that at high Richardson numbers, self-sustained oscillations cease to exist in the absence of gravity. Similar observations were also made by Jiang and Luo [40] for the case of a thermal plume. It must be noted that, in all these studies the density variation is strong and therefore non-Boussinesq in nature. However, under the Boussinesq approximation there is no baroclinic torque and the spatiotemporal dynamics are shown to be dominated by the helical mode $m = 1$ rather than the axisymmetric mode $m = 0$ [10].

The current investigation, however, is focused towards understanding the axisymmetric puffing of strongly heated thermal plumes from a global instability point of view. Note that in order to account for the strong inhomogeneity in density, the analysis is performed under the low Mach number approximation. The paper is organised as follows: the governing equations, computation of the base flow and its linear stability are discussed in Sect.

A.2. Section A.3 documents the variation of stability characteristics of the flow with Froude number and a discussion of the role of buoyancy in the dynamics is presented. The findings are summarized and juxtaposed against previous works in Sect. A.4.

A.2 Formulation

A calorically perfect fluid with Prandtl number Pr, is injected into a quiescent ambient of the same fluid with a prescribed velocity and density profile at the station $z = 0$ through a nozzle of radius R at temperature T_j and density ρ_j on the axis. Adopting the radius of the nozzle R as length scale, ambient temperature $T_\infty (< T_j)$ as temperature scale, ambient density $\rho_\infty (> \rho_j)$ as the density scale and centreline velocity at $z = 0$, u_j, as velocity scale, the non-dimensional governing equations, under the low Mach number approximation, are obtained as:

$$\frac{\partial \rho}{\partial t} + \nabla \cdot (\rho \mathbf{u}) = 0, \tag{A.1}$$

$$\rho \frac{D\mathbf{u}}{Dt} = -\nabla p + \frac{1}{ReS}\left[\nabla^2 \mathbf{u} + \frac{1}{3}\nabla(\nabla \cdot \mathbf{u})\right] + \frac{1}{Fr^2} \quad (1-\rho)\mathbf{e_z}, \tag{A.2}$$

$$\rho \frac{DT}{Dt} = \frac{1}{PrReS}\nabla^2 T, \tag{A.3}$$

$$\rho(1 + T(S-1)) = 1, \tag{A.4}$$

where T is the reduced temperature, $Re = \rho_j u_j R/\mu$, $Fr = u_j/\sqrt{gR}$, and $S = \rho_\infty/\rho_j$. Instead of the Froude number Fr, one could also define a Richardson number $Ri = (S-1)/Fr^2 = (\rho_\infty/\rho_j - 1)gR/u_j^2$. As we wish to extend this study in the future to various values of S, the Richardson number Ri is preferred over Fr as it was demonstrated to be a better parameter to analyze the variation of Strouhal number [9]. Throughout this analysis, the Prandtl number Pr is set to 0.7.

The base flow is assumed to be axisymmetric and computed by the Newton-Raphson method using the finite element method in FreeFEM++ [25] on a domain which is 80 radii along the axial/streamwise direction and 30 radii along the radial/transverse direction. The non-dimensional axial velocity and temperature at the inlet ($z = 0$) are assumed to be of the form $u_z(r, z = 0) = T(r, z = 0) = 0.5 + 0.5 \tanh[0.25(R/\theta)(1/r - r)]$ where a moderately thin value $R/\theta = 10$ has been chosen throughout the analysis and the radial velocity is set to zero at the station $z = 0$. Apart from these Dirichlet

type boundary conditions for velocity and temperature at the inlet, stress-free boundary conditions are imposed on velocity and pressure at radial and streamwise farfield boundaries. The reduced temperature T is set to zero in farfield radial direction while in the streamwise farfield, a homogeneous Neumann boundary condition is imposed. On the axis, $r = 0$, a Neumann boundary condition is imposed on axial velocity, temperature and density while a Dirichlet boundary condition is imposed on radial velocity [41].

On this base flow, an axisymmetric perturbation of the form $q(r, z)e^{-i\omega t}$ is superposed where $q = [\rho', u_r', u_z', p']^T$ is a column vector denoting the perturbation of flow variables. The governing equations (A.1 - A.4) are linearized to obtain a generalized eigenvalue problem of the form $LNS(q) = \omega M(q)$ with $\omega = \omega_r + i\omega_i$ being the eigenvalue. The matrices LNS and M, denoting the discretized linearized Navier-Stokes operator and the mass matrix respectively, are constructed in FreeFEM++ and the eigenvalues are obtained through Arnoldi method.

A.3 Results and Discussion

A.3.1 Base Flow

In this paper, the analysis is limited to the case of $Re = 200, 500$, $S = 7$ while Ri is varied from 0.0006 to 600. The base flow solution was found to be well converged with a residue less than 10^{-9} and is also independent of the grid resolution and domain size. Figure A.1 demonstrates the variation of axial velocity in the $r - z$ plane for $Ri = 0.0006$ and 600 at $Re = 200$. Note that smaller Ri indicates small or negligible effect of buoyancy in comparison to inertia while large Ri indicates dominance of buoyancy over inertia. It can be seen that in the case of $Ri = 0.0006$, the inlet momentum is radially dissipated as it is convected downstream similar to jets, while for $Ri = 600$ it is continually accelerated under the effect of buoyancy which is a characteristic feature of plumes.

A.3.2 Global Stability

For the above two base flows, the global stability is analyzed in a linear framework. Figure A.2 shows the spectrum in the complex $\omega-$plane where the black markers indicate the spectrum for $Re = 200$, $S = 7$ in the presence of buoyancy, while the red markers indicate the spectrum in the absence

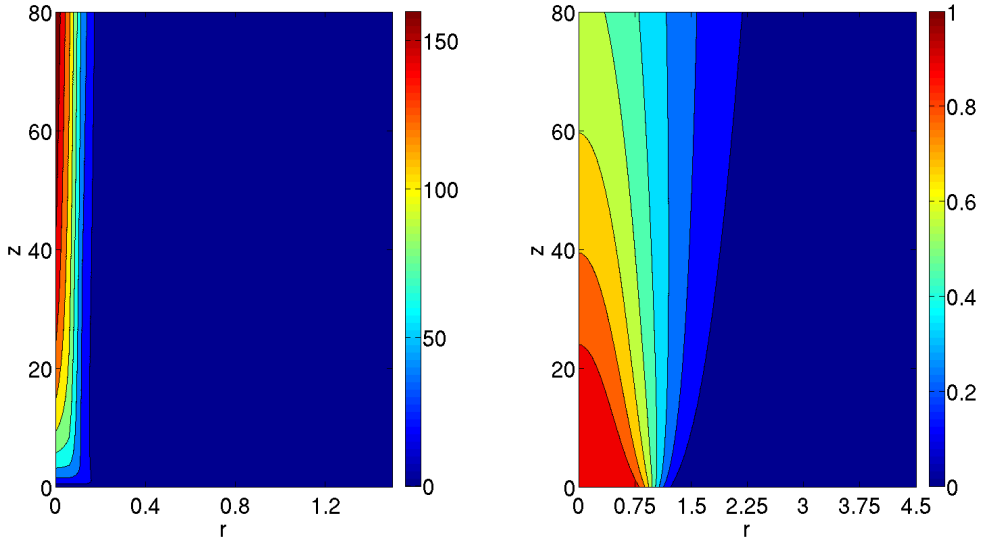

Figure A.1: Spatial distribution of base flow axial velocity in the $r-z$ plane at $Ri = 600$ (left) and $Ri = 0.0006$ (right) for $S = 7$ and $Re = 200$.

of buoyancy. It is seen that the Strouhal number St ($St = \omega_r/2\pi$) and growth rate ω_i increase as Ri increases. Here, the effect of buoyancy on the flow dynamics is captured by computing the spectrum with and without buoyancy. For the case without buoyancy, the stability matrices LNS and M are obtained by artificially setting the Ri to a very low value in the linearized equations, while the base flow corresponds to the exact solution at the higher Ri. The effect of buoyancy is negligible at low Ri (the spectra almost coincide and cannot be distinguished visually), while at high Ri the flow is stabilized in the absence of buoyancy. It is interesting to note the distinct character of buoyancy: as Ri is increased, the base flow which is unstable even in the absence of buoyancy becomes stable to shear while a new instability is triggered by buoyancy on this new base flow.

The variation of St with Ri is shown in figure A.3 for $Re = 200$ (solid line) and 500 (circular markers) on a log-log scale. It can be seen that Re only weakly influences St. At low values of Ri, St is seen to be invariant with Ri, indicating a negligible influence of Ri. However, for values of $Ri > 1$, St is strongly dependent on Ri and follows the relation $St \propto Ri^{\,0.42}$ which closely matches the experimental result $St \propto Ri^{\,0.38}$ obtained for light Helium jets by Cetegen and Kasper [9] in the range $1 \leq Ri \leq 100$ (Ri_1 in [9] is equivalent to the current definition of Ri). For $100 \leq Ri \leq 500$, a different power law was

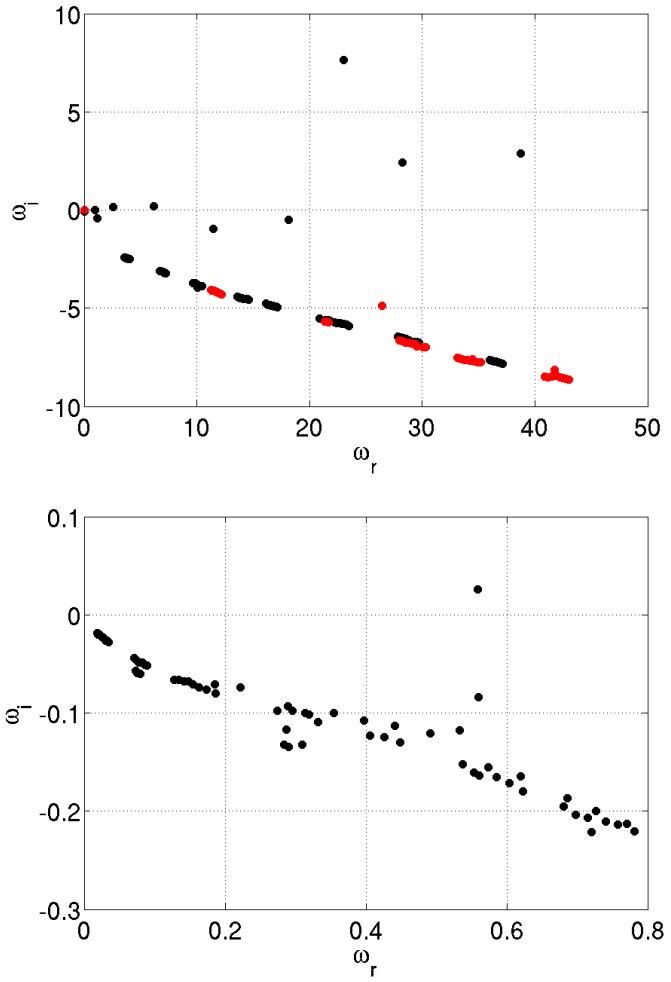

Figure A.2: Eigenvalue spectrum in the complex $\omega-$plane for $Ri = 600$ (left) and $Ri = 0.0006$ (right) at $S = 7$ and $Re = 200$.The red markers denoted the case where buoyancy is switched off in the perturbation equations while black markers are obtained by solving the exact perturbation equations.

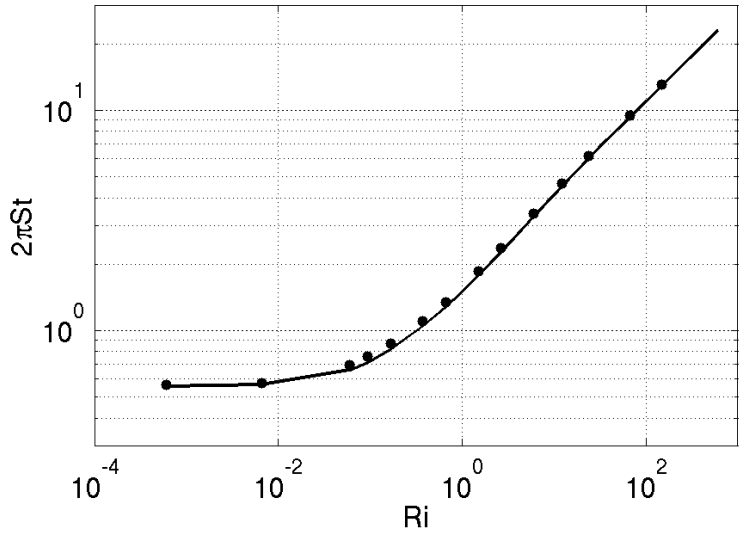

Figure A.3: Variation of Strouhal number with Richardson number in a log-log plot at $Re = 200$ (solid line) and $Re = 500$ (circular markers). At large Ri, St scales as $Ri^{\ 0.42}$.

proposed by these authors and also the spectrum was seen to exhibit multiple peaks (figure 8(c,d) in [9]). The current investigation, however indicates that the most unstable global mode follows the same power law for all $Ri > 1$. This discrepancy between the two investigations could be due to the multiple unstable modes observed at large Ri. In figure A.2, it can be seen that apart from the most unstable global mode, which follows the $St \propto Ri^{0.42}$ power law, there are multiple unstable modes with smaller $\omega_i(> 0)$ which may interact non-linearly resulting in a different St. This could be a plausible explanation for the multiple peaks observed in their experiments and a different power law for $Ri > 100$. Another interesting feature of the variation in St is the rather smooth transition from shear-dominated to buoyancy-dominated behaviour similar to the local stability characteristics of the Boussinesq plume [10].

Global stability of the $m = 1$ helical mode was also performed and for all the parameters investigated in this study, the flow was found to be stable. This is in contrast to the Boussinesq limit, where only the $m = 1$ mode is absolutely unstable and the $m = 0$ mode is at most convectively unstable [10]. A plausible explanation for this could be the absence of baroclinic torque in the Boussinesq limit.

A.4 Conclusions

The global stability of a thermal plume has been investigated in a linear framework under the low Mach number approximation. Variation of the global frequency, ω_r or St, and growth rate, ω_i, with Ri have been documented for $S = 7$ at $Re = 200, 500$. In the range of parameters investigated, only $m = 0$ modes were found become globally unstable. At low Ri, the behaviour of a jet was recovered and the dynamics were independent of buoyancy. However, at large Ri, the instability is strongly effected by buoyancy. It is important to note that the transition from baroclinic and shear dominated behaviour to buoyancy dominated behaviour is smooth which can be seen from the variation of St with Ri. The variation of St with Ri compares well with the experimental data corresponding to isothermal Helium jets injected into air [9, 85]. Also, St was observed to be only weakly dependent on Re, which is again consistent with the experimental studies on Helium jets.

An important *caveat* of the current investigation is that it is non-Boussinesq in nature and the dynamics are very different from the Boussinesq limit. The local stability analysis on a Boussinesq plume indicates that only a helical $m = 1$ mode is absolutely unstable and therefore might possible become globally unstable [10]. However, in the current study $m = 0$ is seen to be globally unstable indicating a strong dependence on the value of S. Further analysis is required to establish if there is transition from $m = 0$ to $m = 1$ in a global scenario as we vary the density ratio S.

Acknowledgements

This work is being supported by the Agence Nationale de la Recherche (ANR) under the Cool Jazz project, grant number ANR-12-BS09-0024.

Bibliography

[1] E. Akervik, U. Ehrenstein, F. Gallaire & D. S. Henningson, 2008.
Global two-dimensional stability measures of the flat plate boundary-layer flow. *Eur. J. Mech. B/Fluids* **27(5)**, 501–513.

[2] G. K. Batchelor & A. E. Gill, 1962.
Analysis of the stability of axisymmetric jets. *J. Fluid Mech.* **14**, 529–551.

[3] A. Bers, 1983.
Space-time evolution of plasma instabilities-absolute and convective. *Basic plasma phys.* **1**.

[4] P. Billant & J.-M. Chomaz, 2000.
Theoretical analysis of the zigzag instability of a vertical columnar vortex pair in a strongly stratified fluid. *J. Fluid Mech.* **419**, 29–63.

[5] R. B. Bornoff & M. R. Mokhtarzadeh-Dehghan, 2001.
A numerical study of interacting buoyant cooling-tower plumes. *Atmospheric Environment* **35(3)**, 589–598.

[6] R. S. Brand & F. J. Lahey, 1967.
The heated laminar vertical jet. *J. Fluid Mech.* **29(2)**, 305–315.

[7] R. J. Briggs, 1964.
Electron-stream interaction with plasmas. M. I. T. Press.

[8] B. M. Cetegen, Y. Dong & M. C. Soteriou, 1998.
Experiments on stability and oscillatory behaviour of planar buoyant plumes. *Phys. Fluids* **10(7)**, 1658–1665.

[9] B. M. Cetegen & K. D. Kasper, 1996.
Experiments on the oscillatory behavior of buoyant plumes of helium and heliumair mixtures. *Phys. Fluids* **8(11)**, 2974–2984.

[10] R. V. K. Chakravarthy, L. Lesshafft & P. Huerre, 2015.
Local linear stability of laminar axisymmetric plumes. *J. Fluid Mech.* **580**, 344–369.

[11] G. J. Chandler, 2010.
Sensitivity analysis of low density jets and flames. PhD thesis, University of Cambridge, Cambridge, U. K.

[12] J. M. Chomaz, P. Huerre & L. G. Redekopp, 1991.
A frequency selection criterion in spatially developing flows. *Stud. Appl. Math.* **84(2)**, 119–144.

[13] W. Coenen, L. Lesshafft, X. Garnaud & A. Sevilla, 2015.
Global mode analysis and frequency response of low-density jets. *J. Fluid Mech.* **in preparation**.

[14] W. Coenen & A. Sevilla, 2012.
The structure of the absolutely unstable regions in the near field of low-density jets. *J. Fluid Mech.* **713**, 123–149.

[15] C. Cossu & J. M. Chomaz, 1997.
Global measures of local convective instabilities. *Phys. Rev. Lett.* **78(23)**, 4387–4390.

[16] A. Couairon & J. M. Chomaz, 1997.
Absolute and convective instabilities, front velocities and global modes in nonlinear systems. *Physica D: Nonlinear Phenomena.* **108(3)**, 236–276.

[17] A. Couairon & J. M. Chomaz, 1997.
Pattern selection in the presence of a cross flow. *Phys. Rev. Lett.* **79(14)**, 2666–2669.

[18] A. Couairon & J. M. Chomaz, 1999.
Fully nonlinear global modes in slowly varying flows. *Phys. Fluids* **11(12)**, 3688–3703.

[19] D. G. Crighton & M. Gaster, 1976.
Stability of slowly diverging jet flow. *J. Fluid Mech.* **77(02)**, 397–413.

[20] I. Delbende & J.-M. Chomaz, 1998.
Nonlinear convective/absolute instabilities in parallel two-dimensional wakes. *Phys. Fluids* **10(11)**, 2724–2736.

[21] I. Delbende, J.-M. Chomaz & P. Huerre, 1998.
Absolute/convective instabilities in the batchelor vortex: a numerical study of the linear impulse response. *J. Fluid Mech.* **355**, 229–254.

[22] A. Deloncle, 2007.
Three dimensional instabilities in stratified fluids. PhD thesis, Ecole polytechnique, Palaiseau, France.

[23] P. G. Drazin & W. H. Reid, 2004.
Hydrodynamic stability. Cambridge University Press, Cambridge.

[24] U. Ehrenstein & F. Gallaire, 2005.
On two-dimensional temporal modes in spatially evolving open flows: the flat-plate boundary layer. *J. Fluid Mech.* **536**, 209–218.

[25] X. Garnaud, L. Lesshafft, P. J. Schmid & P. Huerre, 2013.
Modal and transient dynamics of jet flows. *Phys. Fluids* **25(4)**, 044103.

[26] B. Gebhart, 1973.
Instability, transition, and turbulence in buoyancy-induced flows. *Ann. Rev. Fluid Mech.* **5(1)**, 213–246.

[27] F. Giannetti & L. Luchini, 2007.
Structural sensitivity of the first instability of the cylinder wake. *J. Fluid Mech.* **581**, 167–197.

[28] A. E. Gill & A. Davey, 1969.
Instabilities of a buoyancy-driven system. *J. Fluid Mech.* **35(4)**, 775–798.

[29] M. P. Hallberg & P. J. Strykowski, 2006.
On the universality of global modes in low-density axisymmetric jets. *J. Fluid Mech.* **569**, 493–507.

[30] T. Hattori, N. Bartos, S. E. Norris, M. P. Kirkpatrick & S. W. Armfield, 2013.
Prandtl number dependence and instability mechanism of the near-field flow in planar thermal plume. *J. Fluid Mech.* **732**, 105–127.

[31] T. Hattori, N. Bartos, S. E. Norris, M. P. Kirkpatrick & S. W. Armfield, 2013.
Simulation and analysis of puffing instability in the near field of pure thermal planar plumes. *Intl J. Therm. Sci.* **69**, 1–13.

[32] T. L. Heath, 1897.
On floating bodies, book I. In *The works of Archimedes*, pages 253–262. Cambridge University Press, Cambridge.

[33] N. E. Huang & S. S. Shen, 2005.
Hilbert-huang transform and its applications (vol. 5). World Scientific.

[34] P. Huerre, 2000.
Open shear flow instabilities. In G. K. Batchelor, H. K. Moffatt & M. G. Worster, editors, *Perspectives in fluid dynamics*, pages 159–230. Cambridge University Press, Cambridge.

[35] P. Huerre & P. A. Monkewitz, 1985.
Absolute and convective instabilities in free shear layers. *J. Fluid Mech.* **159**, 151–168.

[36] P. Huerre & M. Rossi, 1998.
Hydrodynamic instabilities in open shear flows. In C. Godreche & P. Manneville, editors, *Hydrodynamics and Nonlinear Instabilities*, pages 81–294. Cambridge University Press, New York.

[37] G. R. Hunt & N. G. Kaye, 2001.
Virtual origin correction for lazy turbulent plumes. *J. Fluid Mech.* **435**, 377–396.

[38] S. Jendoubi & P. J. Strykowski, 1994.
Absolute and convective instability of axisymmetric jets with external flow. *Phys. Fluids* **6(9)**, 3000–3009.

[39] X. Jiang & K. H. Luo, 2000.
Combustion-induced buoyancy effects of an axisymmetric reactive plume. *Proc. of the Combustion Institute* **28(2)**, 1989–1995.

[40] X. Jiang & K. H. Luo, 2000.
Direct numerical simulation of the puffing phenomenon of an axisymmetric thermal plume. *Theoret. Comput. Fluid Dynamics* **14**, 55–74.

[41] M. R. Khorrami, M. R. Malik & R. L. Ash, 1989.
Application of spectral collocation techniques to the stability of swirling flows. *J. Comput. Phys.* **81**, 206–229.

[42] R. Lakkaraju & M. Alam, 2007.
Effects of Prandtl number and a new instability mode in a plane thermal plume. *J. Fluid Mech.* **592**, 221–231.

[43] L. Lesshafft, 2015.
Linear global stability of a confined plume. *Theoretical. Appl. Mech. Lett.* **5(3)**, 126–128.

[44] L. Lesshafft & P. Huerre, 2007.
Linear impulse response in hot round jets. *Phys. Fluids* **19(2)**, 024102.

[45] L. Lesshafft, P. Huerre & P. Sagaut, 2007.
Frequency selection in globally unstable round jets. *Phys. Fluids* **19(5)**, 054108.

[46] L. Lesshafft, P. Huerre, P. Sagaut & M. Terracol, 2006.
Nonlinear global modes in hot jets. *J. Fluid Mech.* **554**, 393–409.

[47] L. Lesshafft & O. Marquet, 2010.
Optimal velocity and density profiles for the onset of absolute instability in jets. *J. Fluid Mech.* **662**, 398–408.

[48] E. J. List, 1982.
Turbulent jets and plumes. *Ann. Rev. Fluid Mech.* **14(1)**, 189–212.

[49] M. Lombardi, C. P. Caulfield, C. Cossu, A. I. Pesci & R. E. Goldstein, 2011.
Growth and instability of a laminar plume in a strongly stratified environment. *J. Fluid Mech.* **671**, 184–206.

[50] J. M. Lopez & F. Marques, 2013.
Instability of plumes driven by localized heating. *J. Fluid Mech.* **736**, 616–640.

[51] O. Marquet & L. Lesshafft, 2015.
Identifying the active flow regions that drive linear and nonlinear instabilities. *J. Fluid Mech.* **under review**.

[52] O. Marquet, D. Sipp & L. Jacquin, 2008.
Sensitivity analysis and passive control of cylinder flow. *J. Fluid Mech.* **615**, 221–252.

[53] T. Maxworthy, 1999.
The flickering candle: transition to a global oscillation in a thermal plume. *J. Fluid Mech.* **390**, 297–323.

[54] P. A. McMurtry, W. H. Jou, J. J. Riley & R. W. Metcalfe, 1986.

Direct numerical simulations of a reacting mixing layer with chemical heat release. *AIAA journal* **24(6)**, 962–970.

[55] P. Meliga, J. M. Chomaz & D. Sipp, 2009.
Global mode interaction and pattern selection in the wake of a disk: a weakly nonlinear expansion. *J. Fluid Mech.* **633**, 159–189.

[56] P. Meliga, D. Sipp & J.-M. Chomaz, 2010.
Effect of compressibility on the global stability of axisymmetric wake flows. *J. Fluid Mech.* **660**, 499–526.

[57] A. Michalke, 1984.
Survey on jet instability. *Prog. Aerospace Sci.* **21**, 159–199.

[58] J. C. Mollendorf & B. Gebhart, 1973.
An experimental and numerical study of the viscous stability of a round laminar vertical jet with and without thermal buoyancy for symmetric and asymmetric perturbations. *J. Fluid Mech.* **61(2)**, 367–399.

[59] P. Monkewitz & K. Sohn, 1988.
Absolute instability in hot jets. *AIAA* **26**, 911–916.

[60] P. A. Monkewitz, D. W. Bechert, B. Barsikow & B. Lehmann, 1990.
Self-excited oscillations and mixing in a heated round jet. *Phys. Fluids* **213**, 611–639.

[61] B. R. Morton, G. Taylor & J. S. Turner, 1956.
Turbulent gravitational convection from maintained and instantaneous sources. *Proc. Royal Soc. London A: Math., Physical and Engg. Sci.* **234(1196)**, 1–23.

[62] P. R. Nachtsheim, 1963.
Stability of free-convection boundary layer flows. Technical Report 2089, NACA TN D-.

[63] F. Nadal, P. Meunier, B. Pouligny & E. Laurichesse, 2011.
Stationary plume induced by carbon dioxide dissolution. *J. Fluid Mech.* **719**, 203–229.

[64] J. W. Nichols, P. J. Schmid & J. J. Riley, 2007.
Self-sustained oscillations in variable-density round jets. *J. Fluid Mech.* **582**, 341–376.

[65] W. M. F. Orr, 1907.
The stability or instability of the steady motions of a perfect liquid and of a viscous liquid. part ii: A viscous liquid. pages 69–138. Hodges, Figgis, & Co.

[66] J.-M. Chomaz P. Brancher & P. Huerre, 1994.
Direct numerical simulations of round jets: Vortex induction and side jets. *Phys. Fluids* **6(5)**, 1768–1774.

[67] L. Pera & B. Gebhart, 1971.
The nature of vertical natural convection flows resulting from the combined buoyancy effects of thermal and mass diffusion. *Intl. J. Heat and Mass Trans.* **14(12)**, 2025–2050.

[68] L. Pera & B. Gebhart, 1971.
On the stability of laminar plumes: some numerical solutions and experiments. *Intl. J. Heat and Mass Trans.* **14(7)**, 975–984.

[69] B. Pier, 2008.
Local and global instabilities in the wake of a sphere. *J. Fluid Mech.* **603**, 39–61.

[70] B. Pier & P. Huerre, 1996.
Fully nonlinear global modes in spatially developing media. *Physica D: Nonlinear Phenomena* **97(1)**, 206–222.

[71] B. Pier, P. Huerre & J. M. Chomaz, 2001.
Bifurcation to fully nonlinear synchronized structures in slowly varying media. *Physica D: Nonlinear Phenomena* **148**, 49–96.

[72] B. Pier, P. Huerre, J. M. Chomaz & A. Couairon, 1998.
Steep nonlinear global modes in spatially developing media. *Phys. Fluids* **10(10)**, 2433–2435.

[73] F. Plourde, M. V. Pham, S. D. Kim & S. Balachandar, 2008.
Direct numerical simulations of a rapidly expanding thermal plume: structure and entrainment interaction. *J. Fluid Mech.* **604**, 99–123.

[74] M. Provansal, M. Mathis & L. Boyer, 1987.
Bénard-von Kármán instability: transient and forced regimes. *J. Fluid Mech.* **182**, 1–22.

[75] Q. A. Quadri, 2013.
Global stability and control of swirling jets and flames. PhD thesis, University of Cambridge, Cambridge, U. K.

[76] L. Rayleigh, 1880.
On the stability or instability of certain fluid motions. *Scientific Papers* **3**, 594–596.

[77] D. S. Riley & D. G. Drake, 1983.
Mixed convection in an axisymmetric buoyant plume. *Q. Jl Mech. appl. Math.* **36(1)**, 43–54.

[78] D. S. Riley & M. Tveitereid, 1984.
On the stability of an axisymmetric plume in a uniform flow. *J. Fluid Mech.* **142**, 171–186.

[79] R. P. Satti & A. K. Agrawal, 2004.
Numerical analysis of flow evolution in a helium jet injected into ambient air. *ASME* **2**, 1267–1276.

[80] R. P. Satti & A. K. Agrawal, 2006.
Computational analysis of gravitational effects in low-density gas jets. *AIAA* **44(7)**, 1505–1515.

[81] R. P. Satti & A. K. Agrawal, 2006.
Flow structure in the near-field of buoyant low-density gas jets. *Int. J. of Heat and Fluid* **27(2)**, 336–347.

[82] A. Sommerfeld, 1908.
Ein beitrag zur hydrodynamischen erklaerung der turbulenten fluessigkeitsbewegungen. pages 116–124.

[83] K. R. Sreenivasan, S. Raghu & D. Kyle, 1989.
Absolute instability in variable density round jets. *Exps. Fluids* **213**, 309–317.

[84] P. J. Strykowski & D. L. Niccum, 1991.
The stability of countercurrent mixing layers in circular jets. *J. Fluid Mech.* **227**, 309–343.

[85] E. R. Subbarao & B. J. Cantwell, 1992.
Investigation of a co-flowing buoyant jet: experiments on the effect of reynolds number and richardson number. *J. Fluid Mech.* **245**, 69–90.

[86] S. E. Norris M. P. Kirkpatrick T. Hattori, N. Bartos & S. W. Armfield, 2013.
Experimental and numerical investigation of unsteady behaviour in the near-field of pure thermal planar plumes. *Experimental Thermal and Fluid Science* **46**, 139–150.

[87] O. Tammisola, 2015.
Oscillatory sensitivity patterns for global modes in wakes. *J. Fluid Mech.* **701**, 251–277.

[88] T. G. Thomas & H. S. Takhar, 1988.
Second-order effects in an axisymmetric plume. *Q. Jl Mech. appl. Math.* **41(1)**, 1–16.

[89] S. A. Thorpe, 2005.
The turbulent ocean. Cambridge University Press, New York.

[90] D. J. Tritton, 1988.
Physical fluid dynamics. Clarendon Press, Oxford.

[91] M. Tveitereid & D. S. Riley, 1992.
Nonparallel flow stability of an axisymmetric buoyant plume in a coflowing uniform stream. *Phys. Fluids A* **4(10)**, 2151–2161.

[92] M. van Dyke, 1982.
An album of fluid motion. page figure 107. Parabolic Press.

[93] S. Wakitani, 1980.
The stability of a natural convection flow above a point heat source. *J. Phys. Soc. Japan* **49(6)**, 2392–2399.

[94] R. J. Whittaker & J. R. Lister, 2006.
Steady axisymmetric creeping plumes above a planar boundary. part 1. a point source. *J. Fluid Mech.* **567**, 361–378.

[95] R. J. Whittaker & J. R. Lister, 2006.
Steady axisymmetric creeping plumes above a planar boundary. part 2. a distributed source. *J. Fluid Mech.* **567**, 379–397.

[96] A. W. Woods, 2010.
Turbulent plumes in nature. *Ann. Rev. Fluid Mech.* **42**, 391–412.

[97] M. G. Worster, 1986.
The axisymmetric laminar plume: asymptotic solution for large Prandtl number. *Stud. Appl. Math.* **75**, 139–152.

[98] C. S. Yih, 1988.
Fluid mechanics. West River Press, Ann Arbor.